FLEXIBLE, STRETCHABLE, AND TRANSIENT ELECTRONICS FOR INTEGRATION WITH THE HUMAN BODY

BY

SANG M. WON

DISSERTATION

Submitted in partial fulfillment of the requirements
for the degree of Doctor of Philosophy in Electrical and Computer Engineering
in the Graduate College of the
University of Illinois at Urbana-Champaign, 2019

Urbana, Illinois

Doctoral Committee:

Professor John A. Rogers, Chair
Professor Rashid Bashir, Co-chair
Professor Brian T. Cunningham
Professor Joseph W. Lyding
Professor Xiuling Li

Abstract

Technologies capable of establishing intimate, long-lived interfaces to the human body have broad utility in continuous measurement of physiological status, with the potential to significantly lower tissue injury and irritation after implants. The development of such soft, biocompatible platforms and integrating them into a biotissue-interfaced system requires suitable choice of materials and engineered structures. Specific directions include overall miniaturization (e.g., Si nanomembrane) or composite material structure (e.g., carbon black doped elastomer) that provide effective mechanics to match those of biological tissues. This dissertation presents combined experimental and theoretical investigations of such functional systems that offer flexibility and stretchability, while maintaining operational performance and mechanical robustness. The dissertation begins with a fundamental study of responsive monocrystalline silicon nanomembrane as a flexible electromechanical sensor element. Subsequent chapters highlight integration with active components for wireless addressing, multiplexing, and local amplification, with multimodal operation in a thin, soft, skin-like platform. The resulting biointegrated system enables (1) sensitive health monitoring system, (2) multifunctional tactile sensor, (3) high-density neural interfaces, and (4) physically transient, implantable electronics, all with the capability of stable operation for long timeframes.

To my parents and family

Table of Contents

Chapter 1. Introduction

1.1 Research Motivation

The most widely used and high-performance electronics exploit single-crystal inorganic materials, such as silicon or gallium nitride, in wafer-based, rigid, and planar form [1-3]. Biological tissues are, by contrast, curvilinear and soft (modulus of ~kPa, compared to ~GPa for bulk wafer and metal). This mechanical mismatch between conventional rigid electronic materials/devices and the human body hinders the development of bioelectronics systems capable of conformal, intimate integration, for applications ranging from measurement of biological signals (i.e. electrophysiological, physiological, thermal, mechanical, biochemical information) to delivery of therapies and stimulus. To remedy the current situation, recent advances in design strategies and fabrication techniques have focused on overcoming intrinsic limitations associated with the material mechanics for noninvasive implantation and subsequent chronic operation, in a way to minimize tissue damage and immune response [4,5]. One specific direction is the overall miniaturization. Here, flexural rigidity of micro/nanoscale wires, ribbons, and membranes can be more than ten orders of magnitude smaller than bulk counterparts [6,7]. Alternative approaches use composite material structures that provide effective mechanics to match those of biological tissues. These recent advances open new possibilities for studying chronic diseases, improving surgical procedures and empowering patients to self-manage their own health. Applications include brain-machine interfaces to treat diverse neurological disorders [8,9], skin-based devices to monitor health markers [10,11], sophisticated prosthetics [12], and robotic interfaces [13,14].

Following these current research trends, my research group has built functional systems, based on both inorganic and organic materials, that interface with the complex geometries, soft modulus, and time-dynamic tissues of the human body. Specifically, this dissertation will explore a combination of previous theoretical and experimental studies for the development, characterization, optimization, and demonstration of (1) an ultrathin single crystalline Si based strain gauge array, (2) battery-free, wireless sensors for pressure mapping, (3) three-dimensional (3D) multimodal sensor, (4) a miniaturized, wireless optoelectronic system for closed loop neuromodulation, (5) long-term implantable bioelectronics for brain interfacing, and (6) natural wax for transient electronics. Overall, all projects relate to developments and demonstrations of unconventional electronics using either ultrathin nanomembrane or composite material structure that provide effective mechanics and geometries suitable to interface with targeted biological tissues.

1.2 Overview

All chapters are completed works that are either published or submitted during the author's PhD study. Chapter 2 presents a strain sensor array using printed single crystalline silicon on plastic substrate. The chapter investigates details of physical principles, fabrication methods, and electrical/mechanical characterization of the system. This work has since become fundamental for most piezoresistive sensors based on ultrathin Si nanomembrane.

Chapter 3 presents battery-free, wireless sensors for full body pressure mapping. The system offers the transmission of the pressure data without external measuring device and wire, which degrade durability and limit the user's activity. Use of multiple sensors (>50) in a time-sequenced manner allows the full body pressure mapping.

Chapter 4 presents unique complex 3D piezoresistive sensors that can detect various external stimuli such as normal pressure, shear force, bending, and temperature. A system shows high sensitivity (gauge factor of ~50) and immediate response in the range of milliseconds. By integrating with Bluetooth platform, the system communicates with external devices in a fully wireless manner without functional or performance degradation.

Chapter 5 presents an implantable wireless optoelectronic system to monitor and modulate bladder function, as well as viral strategies to express opsins in rat bladder afferents. The technology eliminates the need for implantation of potentially damaging bladder catheters or electrodes, and provides unique access to bladder functionality in the awake, freely moving rat.

Chapter 6 presents an actively powered electrode array that can chronically and stably function in both rat and nonhuman primate neocortex. The work demonstrates the feasibility of using a thermally grown, ultrathin layer of silicon dioxide as the dielectric medium for capacitive sensing of neural signal and as the biofluid barrier for chronic operation over more than 10 years.

Chapter 7 presents natural wax as a possible candidate for robust biodegradable encapsulants in homogeneous form as well as an electrically conductive component when processed in the form of a tungsten wax composite.

Chapter 8 summarizes all projects and provides an outlook for future work in the area of biointegrated electronics.

1.3 References

[1] B. G. Streetman et al., *Solid State Electronic Devices*. Upper Saddle River, NJ: Prentice Hall.

[2] E. M. Vogel et al., *Nat. Nanotechnol*. 2, 25 (2007).

[3] D.-H Kim et al., *Annu. Rev. Biomed. Eng*. 14, 113 (2012).

[4] W. M. Grill et al., *Annu. Rev. Biomed. Eng*. 11, 1 (2009).

[5] M. P. Ward et al., *Res. Brain Res.* 1282, 183 (2009).

[6] J. Rivnay et al., *Sci. Adv.* 3, e1601649 (2017).

[7] J. W. Jeong et al., *Neuron* 86, 175 (2015).

[8] D. Khodagholy et al., *Nat. Neurosci.* 18, 310 (2015).

[9] J. Viventi et al., *Nat. Neurosci.* 14, 1599 (2011).

[10] C. Wang et al., *Nat. Mater.* 12, 899 (2013).

[11] D. J. Lipomi et al., *Nat. Nanotechnol* 6, 788 (2011).

[12] D. R. Moore et al., *Nat. Neurosci*. 12, 686 (2009).

[13] Y. R. Jeong et al., *NPG Asia Mater.* 9, e443(2017).

[14] H. Kim, *Sci. Adv.* 3, e1701114 (2017).

Chapter 2. Single Crystalline Si-Based Strain Sensor Array on Flexible Substrate

2.1 Introduction

Conventional metal-based strain gauges offer high-flexibility and low-cost production, but they suffer low sensitivity (gauge factor, or change of resistance by the external strain, of <1) and limited scalability to large area due to the lack of strategies for multiplexed addressing. For example, a 6 x 6 array requires 72 electrodes to address each sensor. Change of band gap structure by the external strain (i.e. piezoresistive effect) in silicon strain gauges, on the other hand, offers high sensitivity (gauge factor of 20~150 [1-4]) and can be scaled to large area with spatial mapping capabilities via coupling to local multiplexer. Typically, silicon-based sensors are fabricated on wafers and then integrated into a small package with microelectronic integrated circuits for signal processing [5,6]. Although well configured in various applications, devices in this rigid form are unsuitable for certain applications such as interfacing on the human body where curvilinear deformation is required. Recent research aimed to overcome this limitation by using deposited amorphous, microcrystalline, and polycrystalline silicon on flexible substrate, but piezoresistive effects in these materials are considerably lower than in single crystalline silicon. This chapter introduces an ultrathin single crystalline silicon (thickness of ~200 nm) based strain gauge bonded to a thin plastic substrate. The resulting device exhibits lightweight construction, mechanical flexibility, and high sensitivity (device gauge factor of 43). This sensor further demonstrates large area with local spatial strain mapping by using Wheatstone bridge configuration and integrating to multiplexing diodes. Significant components of this chapter were published as S. M. Won et al., "Piezoresistive Strain Sensors and Multiplexed Arrays Using Assemblies of Single-Crystalline Silicon Nanoribbons on Plastic Substrates," *IEEE Trans. Elect. Devices* **2011**, 58, 4074.

2.2 Basic Physical Principles

The change of resistance depends on two different mechanisms: geometrical change and resistivity change (i.e. piezoresistive effect). While only the first term contributes to the change of resistance in metal strain gauge, both terms contribute to the change of resistance in a semiconductor strain gauge. This indicates that the high gauge factor of semiconductor is mainly due to the piezoresistive effect. This section will cover the physics behind the change of electrical resistance of semiconductors.

The forbidden energy gap between the conduction and valence bands is due to the interaction between moving electrons and the periodic lattice. When anisotropic tensile stress is applied, lattice spacing along the stress direction increases, whereas spacing along two other perpendicular directions decreases [7]. As a result, it changes the interaction of the electrons with the lattice, yielding the change of the forbidden energy gap. For example, with compression along the [100] direction in n-type silicon, the minimum energy level along the [100] direction becomes lower, whereas the minima along the [010] and [001] directions become higher. This change of energy minima in different directions redistributes the electrons among them. In this example, electrons move toward lower minima, which is in the [100] direction, resulting in an increase of effective mass and subsequently the reduction of mobility and conductivity in the [100] direction. For p-type silicon, on the other hand, hole concentration in the valence band (i.e. light and heavy hole bands) contributes to the piezoresistive effect. As the strain is applied, heavy and light hole bands split, and holes move toward the lower bands. The effect of this redistribution of holes is large for the [111] direction where the effective mass due to the flatness of heavy and light hole bands is greatest. The experimental results show that p-type silicon has a positive strain gauge factor, meaning positive or tensile strain along the current direction causes an increase of the resistivity. This indicates that tensile strain causes the band with lower mobility to be higher with respect to the high-mobility band.

The gauge factor depends on the doping concentration of the silicon (Figure 2.1a). Many electrons in highly doped n-type silicon occupy the energy state in the conduction band, whereas most electrons in lowly doped silicon stay in the valence band. As the stress is applied, the energy band shifts, and electrons in the higher energy level move toward the lower energy level until the equilibrium state. If conduction bands contain a large quantity of electrons, the relative number of replaced electrons is small, thereby resulting small change of resistance. The same principle also applies to the p-type silicon where relative magnitude of hole redistribution between heavy and light hole bands is lower in highly doped silicon. In conclusion, the gauge factor is higher in lowly doped than in highly doped silicon for both p- and n-type.

The gauge factor also depends on the temperature (Figure 2.1b). It appears that lowly doped silicon with large gauge factor shows higher temperature dependency compared to highly doped silicon. The occupation of conduction bands by electrons is solely determined by the doping concentration in highly doped n-type silicon. As a result, the temperature does not dramatically affect the electron density or, consequently, the gauge factor of the strain gauge. On the other hand, thermally excited electrons in lowly doped silicon contribute greatly to the electron density in conduction bands. This indeed results in a high temperature coefficient of resistance as the relative redistribution due to the temperature is high. In conclusion, the tradeoff between gauge factor and temperature dependency is controlled by the doping concentration; therefore, adjusting the doping level is required to achieve relatively high gauge factor and low temperature dependency of the sensor.

2.3 Experimental

The fabrication of silicon nanomembrane (Si-NM) based strain sensor exploits transfer printing of doped Si-NM generated from silicon-on-insulator (SOI, 200 nm top p-type silicon layer, resistivity of 14-22 Ω-cm) onto polyimide substrate. The process starts by defining highly doped regions through a thermal impurity diffusion. Here, higher impurity concentration improves the temperature independence and ohmic contact between metal electrode and semiconductor at the cost of lower piezoresistive effect. The boron concentration of $\sim 5 \times 10^{18}$ /cm^3 in our strain gauge provides 80 % of gauge factor [8] and temperature dependence reduced by factor of five compared to 1×10^{16} /cm^3 [9]. Subsequent patterning via holes on silicon nanomembrane and etching the SiO_2 layer underneath the silicon selectively in the hydrofluoric acid produce a freely sagged membrane tethered to the underlying wafer. The membrane is then printed on polyimide substrate coated with a thin adhesive layer of polyimide. Finally, the deposition of a layer of SiO_2 (200 nm deposited by plasma-enhanced chemical vapor deposition) and metallization of Cr/Au (50 nm / 200 nm deposited by electron beam evaporation) yields interdielectric layer and electrode, respectively. Figure 2.2a-b shows a schematic illustration and optical image of a strain gauge in Wheatstone bridge design, as well as a separate isolated silicon resistor, all on a plastic substrate. The corresponding circuitry and measurement configuration for the Wheatstone bridge strain gauge is shown in Figure 2.2c, where input voltage is applied to nodes B and D, and output voltage is measured between nodes A and C.

2.4 Results and Discussion

Uniaxial tensile strain is applied in the longitudinal direction to a polyimide substrate which has a printed single silicon resistor (size of $20 \times 200 \times 0.2$ μm^3). The results show the linear dependency of resistance change by the applied tensile strain. The extracted gauge factor of this heterogeneous system is ~43 as shown in Figure 2.3a. The change in the output voltage of the strain gauge in Wheatstone bridge configuration is measured in the same manner (Figure 2.3b). To model the output voltage, we use the well-known equation

$$\frac{Vout}{Vin} = \frac{R_3}{R_3+R_4} - \frac{R_2}{R_1+R_2} \tag{2.1}$$

where R denotes the resistance of each bridge (i.e. each silicon resistor), which is

$$\mathrm{R} = R_0(1 + GF \times strain) \tag{2.2}$$

where strain is the external applied strain and R_0 is the initial resistance.

Figure 2.3c shows mechanical reliability of the strain gauge in repetitive bending cycles. The result indicates constant output voltage through the repetitive cycles up to 1000 at different bending radii. Figure 2.3d presents the change in resistance of the resistor with varying substrate temperature. The obtained temperature coefficient of resistance (TCR), 1.5×10^{-3} / °C, is in agreement with the reported value for p-type silicon with $\sim 10^{18}$ / cm^3 dopant concentration [9]. The Wheatstone bridge configuration minimizes the temperature dependency in the unstrained condition due to the same TCR associated with four silicon resistors, although the temperature affects the device performance in the strained condition.

Integration of sensors with multiplexing PN diodes yields an array structure. PN diodes are chosen as the active multiplexer of the array for their simple structure and stable performance. Figure 2.4a-b shows the schematic layout and optical image of such an array and its single unit cell where PN diodes are integrated at the output node of each Wheatstone bridge. Multiplexing works by applying +3 V to each row, in turn, while holding the bias of all the other rows equal to -3 V. This condition causes all diodes except those that are biased by +3 V to be in the reverse condition; thus, only one Wheatstone bridge that is biased with +3 V contributes the output of each column. Figure 2.4c shows the results of a 6 × 6 strain sensor array with tensile, compressive, and combined strain conditions. The sign of the output voltage corresponds to tensile and compressive strain, applied by bending the substrate in different directions.

2.5 Conclusion

This chapter introduced a flexible array of single crystalline silicon for gauges and p-n diodes for multiplexer on plastic substrate. Mechanical and electrical measurement show high sensitivity and reliability highly suitable to various applications where lightweight and conformal contact on a curvilinear surface is necessary. Collectively, the results suggest the further opportunities of these ideas to address strain mapping in biomedical applications. In fact, this fundamental initial work of Si NM-based electromechanical sensor has been the basis for other projects that will be introduced in later chapters.

2.6 Figures

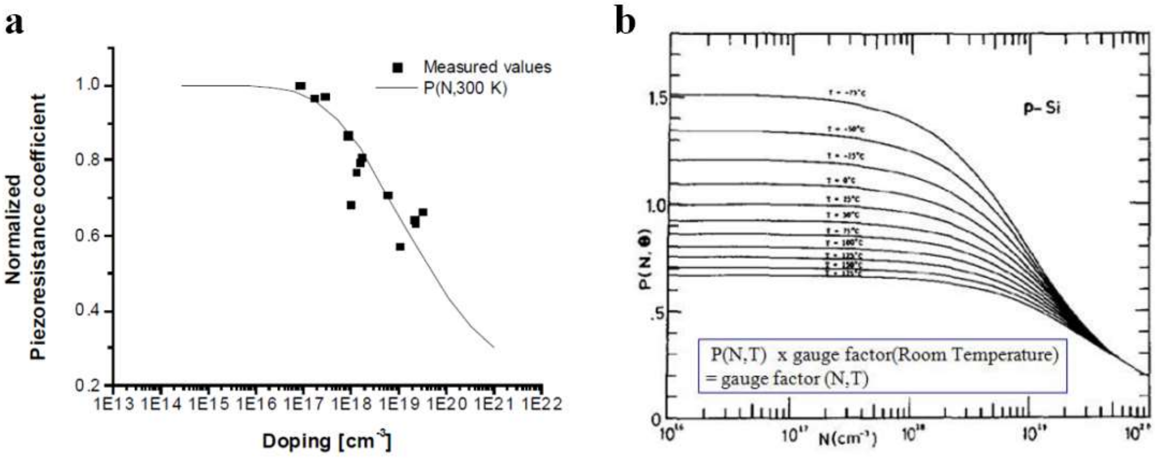

Figure 2.1. Piezoresistive effects in silicon. a) The change of normalized gauge factor of silicon strain gauge at various doping concentrations [10]. The gauge factor decreases with increasing doping concentration. b) Temperature dependency of gauge factor [9]. The factor P by which the gauge factor at room temperature should be multiplied to get the gauge factor at various temperatures is shown.

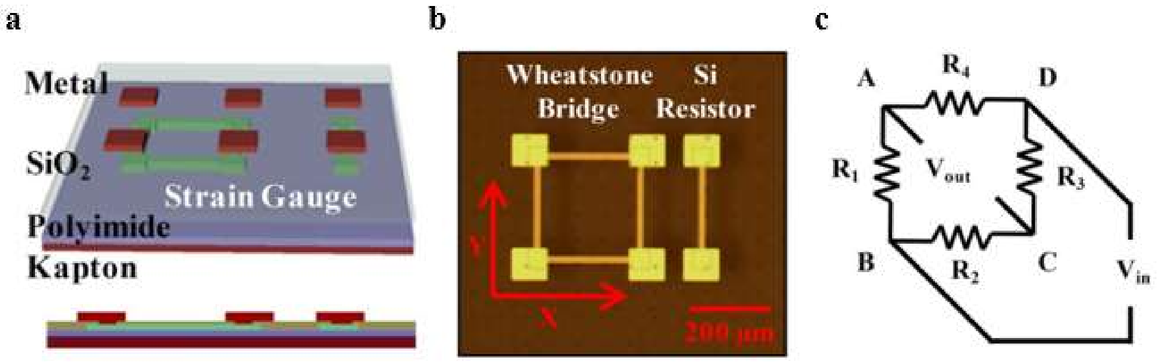

Figure 2.2. Ultrathin single crystalline silicon on polyimide substrate. a) Schematic illustration of silicon resistor on a thin plastic substrate. b) Optical image of a representative Wheatstone bridge and a single isolated silicon resistor. c) Circuit diagram of the Wheatstone bridge.

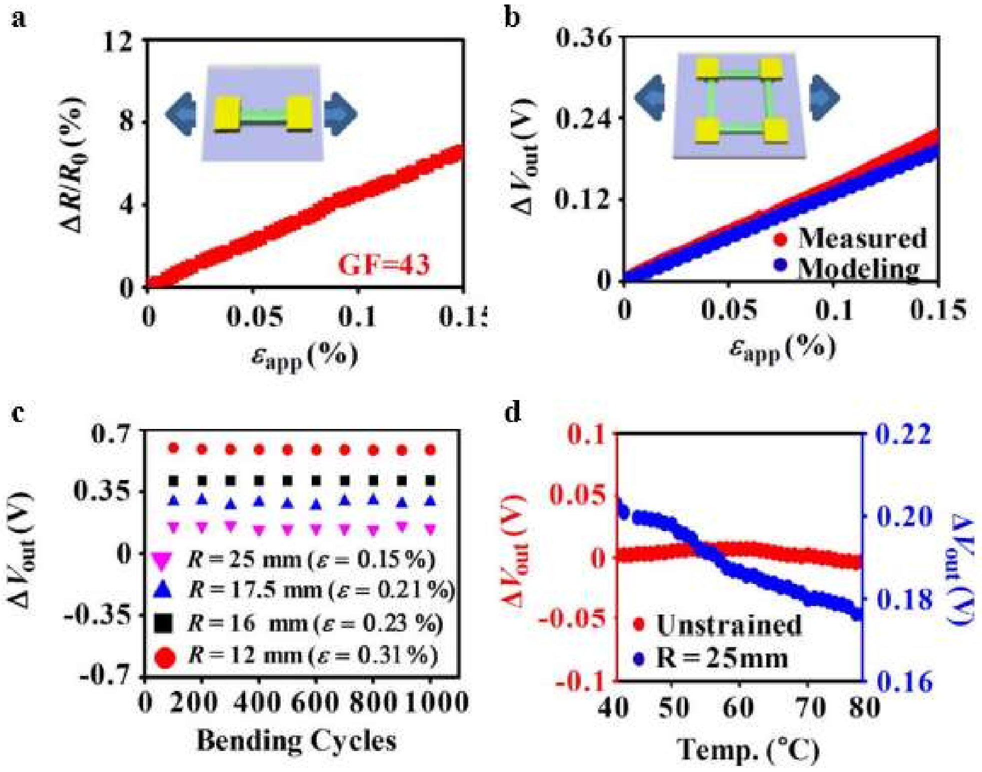

Figure 2.3. Mechanical and electrical characteristics. a) Fractional change in resistance of silicon strain gauge as a function of the uniaxial tensile strain. The slope corresponds to a gauge factor. b) Change of output voltage from a Wheatstone bridge as function of the uniaxial tensile strain. c) Voltage output from Wheatstone bridge while bending cycling test at different radii of curvature. d) Temperature dependence of strain gauge in Wheatstone bridge configuration.

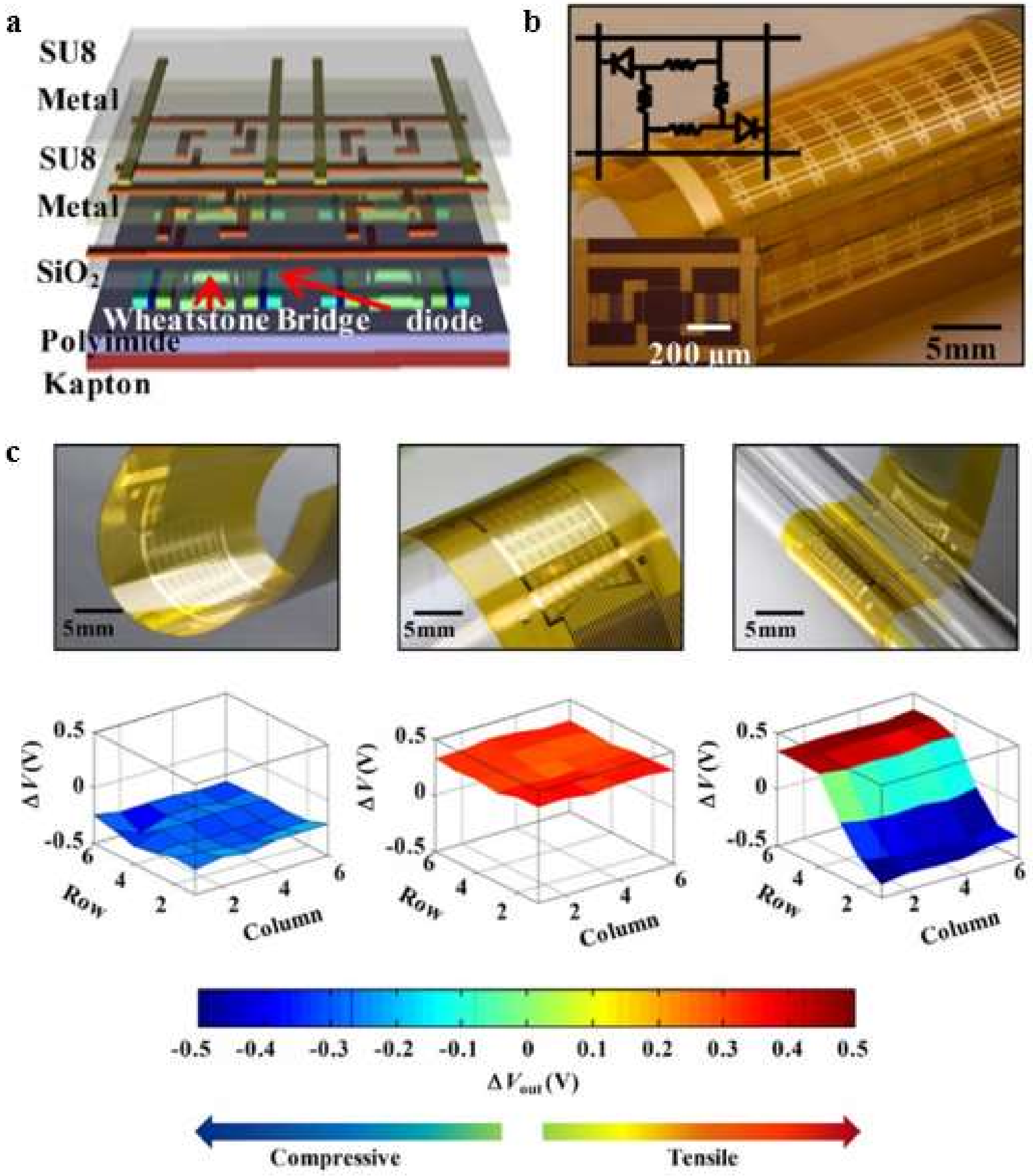

Figure 2.4. Flexible network array of piezoresistive sensors. a) Schematic illustration of a mapping array of silicon strain gauge coupling to PN diodes for multiplexed addressing. b) Optical image of a representative array on flexible substrate. c) Operation of silicon sensor array.

2.7 References

[1] S. M. Won et al., *IEEE Trans Electron Devices* 58, 4074 (2011).

[2] S.-K Kang et al., *Nature* 530, 71 (2016).

[3] J. Shin et al., *Nature Biomed. Eng.* 3, 37 (2018).

[4] S. Han et al., *Science Trans. Med.* 10, eaan4950 (2018).

[5] J. P. Lynch et al., *J. Aerosp. Eng.* 16, 108 (2003).

[6] R. Bogue, *Sens. Rev.* 27, 7 (2007).

[7] S. Middelhoek and S. A. Audet, *Silicon Sensors*. London, UK: Academic Press (1989).

[8] R. Hull, *Properties of Crystalline Silicon*. London, UK, pp. 214-215 (1999).

[9] P. Norton and J. Brandt, *Solid State Electron,* 21, 969 (1978).

[10] E. Lund, presented at MRS fall meeting (Boston, MA, 2000).

Chapter 3. Battery-Free Wireless Sensors for Full Body Pressure Mapping

3.1 Summary

Recent research establishes the foundations for thin, soft, skin-like systems capable of precise, continuous measurements of physiological health, with broad potential relevance to clinical healthcare. Although interesting possibilities that rely on one or a small number of such skin-mounted devices appear in the latest literature, significant advances could follow from the use of large-scale, distributed arrays for full-body, spatiotemporal mapping of physiological processes. This chapter introduces materials, device designs, wireless power delivery and communication strategies and overall system architectures for skin-like, battery-free pressure sensor that can be deployed and operated at scale, with examples of up to 65 independent devices, across the entire body. Combined experimental and theoretical investigations of the operation and modes for wireless addressing establish the key features of these systems. Successful trials on human subjects in clinical sleep laboratories and in adjustable hospital beds demonstrate functionality of immediate practical importance in monitoring circadian cycles and in mitigating risks for pressure-induced skin ulcers.

3.2 Introduction

Thin, soft, skin-like electronic devices with wireless, near field communication (NFC) capabilities offer simple, battery-free platforms with versatile modes of use with relevance to continuous monitoring of physiological health [1-6]. Applications range from those in hospital care and clinical medicine, to physical rehabilitation, fitness/wellness tracking, awareness and cognitive state assessment, and human-machine interfaces [7, 8]. Although deployment of an individual device of this type onto a targeted region of the body offers interesting opportunities and several clinically validated measurement modalities, time-multiplexed addressing of large-scale wireless networks comprised of a multitude of separate devices distributed at many different locations across the body could qualitatively expand the possibilities [8, 9]. Advances reported here achieve this mode of operation, in which NFC power delivery and data communication to a central acquisition/control system occur with long-range readers, and rapid scanning through a large-scale collection of devices mounted on the body provides continuous streams of data that can be assembled into spatiotemporal maps of physiological processes. The result enables full-body coverage in settings of practical importance, ranging from hospital beds to wheelchairs to office desks. Specific examples introduced here involve advanced, skin-like devices designed to precisely measure local pressure and temperature, as quantitatively validated through computational modeling and comparison to experimental controls. Simultaneous wireless operation of such devices laminated onto the skin at 29 - 65 distinct sites across the limbs, torso, neck and head illustrate the possibilities, where single or multiple large-scale loop antennas interfaced to RF power delivery and data acquisition electronics allow multiplexed operation with a range of tens of centimeters to meters. Demonstrations of this technology include tests on several human subjects, with a focus on tracking of sleep patterns in a clinical laboratory, and monitoring of pressure distributions relevant to formation of ulcers in patients confined to hospital beds. Significant components of this chapter were published as S. Han, J. Kim, S. M. Won et al., “Battery-free, wireless sensors for full-body pressure and temperature mapping,” *Science Trans. Med.* 2018, 10, eaan4950.

3.3 Results and Discussion

Figure 3.1a presents a conceptual schematic illustration of the system. Here, 65 wireless, epidermal NFC devices are mounted on the skin at locations across the human body, for monitoring parameters of interest in real time, using a multiplexed, wireless scheme and a single reader antenna. Based on the known locations of the devices, time-dependent data captured in this manner can be rendered as spatial-temporal color plots mapped onto the body shape. Figure 3.1b presents an image of a representative device. The component highlighted with the red dotted line corresponds to the integrated circuit chip that provides the NFC communication capability, along with sub-systems for wireless energy harvesting, temperature sensing and analog-to-digital (A/D) conversion (e.g., ams AG; NFC die SL13A, 100 µm thick, 2.38 × 2.38 mm). The part encompassed by the blue dotted line is a pressure sensor that relies on the piezoresistive response of an ultrathin layer of monocrystalline silicon patterned into a spiral shape (diameter; 6.6 mm, wide; 250 µm). The element indicated with the green dotted line is a simple resistor (0.6 × 0.3 × 0.3 mm) selected to ensure that the response of the pressure sensors falls into a range compatible with the A/D converter.

A detailed, exploded view schematic illustration in Figure 3.1c shows the layout of these components, their interconnections with one another and their integration with the magnetic inductive loop antenna that serves as a wireless interface to an external reader antenna. The construction involves a multilayer stack of (1) an NFC chip, loop antenna (Cu, ~5 µm thick, diameter; 16 mm, width; 75 µm), and silicon piezoresistive pressure sensor, (2) thin films of polyimide (PI, e.g., Microsystem, USA, ~1.2 µm thick) as electrical insulators, (3) an overcoat and base of polydimethylsiloxane (PDMS, e.g., Sylgard ® 184, Dow Corning; mixed at a 30:1 ratio of base to curing agent by weight, ~1 MPa) as encapsulating coatings, and (4) a biocompatible, skin-adhesive tape (Scapa, e.g., Scapa Health Care, thickness; ~50 µm thick, low modulus; ~17 kPa). The overall thin, deformable construction affords skin-compatible mechanics. The thin geometry of the PDMS base (~50 µm thick) minimizes the thermal equilibrium time of the temperature sensor with the skin. The fabrication process is sufficiently routine that many devices can be created easily, at high yield (traditional production yield, 90%).

The spiral structure of thin, monocrystalline silicon serves as the pressure sensing element. The overlayer and base of PDMS protect the sensor and enable conformal contact onto the skin, as shown for the case of the left forearm in Figure 3.2a. The operation uses the piezoresistance response of the silicon in a voltage divider circuit illustrated in Figure 3.2b, where one of two resistors varies by the external pressure. Here, reference resistor, R2 in the circuitry, determines the voltage range to be readable in the capability of NFC chip (0.3~0.6 mV).

Based on the results, the pressure sensor mounted on the left forearm was pressed with the index finger in various ways such as finger poking (green box), touching (black box), and holding (red box) (Figure 3.2c). The enlarged red box shows a temperature change graph when wireless pressure sensor gets continuous force for a while (holding). The silicon pressure module used in this system had a resistance of 29.3 kΩ and employed a 220 kΩ resistor (R_1). The measured voltage range (0.4 ~ 0.6 V), and relative resistance change (Figure 3.3, ΔR/R: ~1.2%), indicated an actual pressure range on human skin of ~6 kPa (poking: ~6 kPa, touching: ~ 3.2 kPa, and holding: ~ 4.1 kPa). The pressure response is further quantitatively analyzed by finite element modeling (FEM). Figure 3.4 shows the analyzed structure and the distributions of strain at an external pressure of 10 kPa. The following equation provides the relationship between the changes in resistance due to piezo-resistivity through a gauge factor (G):

$$R = R_0(1 + G\varepsilon) \tag{3.1}$$

where ε is the strain on the piezo-resistive sensor, and R and R_0 are the final and initial resistance, respectively, under external pressure loading. The average strain was calculated from FEA for pressure ranging from 0 to 10 kPa. With R_0 as 29.3 kΩ the gauge factor was estimated to be ~50. In addition, FEA result shows that the spiral shaped pressure module gets evenly distributed strain change from external force. Here, we selected spiral shape to enhance the uniformity in pressure-induced distribution of strain compared to simple, linear design.

The wireless operating range depends on the sizes of the reader (inductive loop) and sensor, the radio frequency (RF) input power to the antenna, and sensor orientation relative to the reader. The ranges for a sensor oriented parallel to the reader antenna are 12 cm and 32 cm as the maximum for RF power of 4 W and 12 W, respectively. For the multiple sensor reading, communication and power delivery occurred to multiple separate sensors (65 sensors) in a time-sequential manner, continuously, such that all sensors were read within 3 seconds.

Measurement of a patient's skin pressure while lying on a bed has clinical relevance for preventing skin sores, irritation, and decubitus ulcers in hospitalized patients. Development of a full-body wireless pressure sensor NFC system is an important step towards reducing hospital-acquired pressure ulcers. Figure 3.5a-b show 29 dorsal-mounted, NFC pressure sensors on a human subject with specific positions while lying on the bed as indicated. For the study, a 27-year-old male (weight: 90 kg) has been tested. The results show that the shoulder and buttocks were exposed to relatively higher pressure. Color spatial mappings of pressures at various body positions are shown in Figure 3.5c, comparable to published data obtained using a conventional wired sensor [10]. In addition, the sensor was sensitive enough to detect pressure changes due to minor movements of the subject (Figure 3.6)

3.4 Methods

Fabrication of wireless NFC pressure sensor. The fabrication began with spin-coating of a layer of polyimide (PI; 1.2 µm) on a copper foil (Cu; 5 µm), as the first step in defining the loop antenna. Laminating the sheet, with PI side down, onto a glass slide coated with polydimethylsiloxane (PDMS) prepared the structure for photolithography and wet etching to create the loop. Another layer of PI (1.2 µm) uniformly spin-cast on top served as an encapsulation layer. Photolithography and dry etching (RIE; 20 sccm O_2, 200 mTorr, 150 W, 900 s) created small vias through the PI at each end of the loop, for electrical connection. Electron beam evaporation formed another layer of Cu (1 µm). Photolithography and wet etching defined traces and contacts through the vias. Spin-casting yielded an additional coating of PI (1.2 µm). Electron beam evaporation, photolithography and dry etching (RIE; 20 sccm CF_4, 50 mTorr, 100 W, 10 min) defined a hard mask of SiO_2 (50 nm). Further dry etching (20 sccm O_2, 300 mTorr, 200 W, 1800 s) removed the exposed regions of the PI to create openings for electrical connection to the NFC die. A cellulose-based, water soluble tape (Aquasol Corporation, ASWT-2) enabled retrieval of the resulting structure from the PDMS/glass substrate. Electron beam evaporation of a uniform layer of Ti/SiO_2 (5 nm/100 nm) onto the backside of this structure followed by exposure to UV-induced ozone allowed strong bonding to a base layer of PDMS. After removal of the water-soluble tape, application of an In/Ag based solder (Indium Corporation, Ind. 290, 180 ºC) established a mechanical and electrical interface between a NFC bare die, the loop antenna and traces that lead to the components for pressure sensing.

As separate set of fabrication steps outlined below formed a p-doped thin membrane of silicon in the shape of a spiral on a film of polyethylene terephthalate (PET, SKC, Inc.) as a pressure sensor. Silver epoxy (Ted Pella, Inc.) bonded this sensor to corresponding electrode pads on the device. An additional layer of PDMS encapsulates the whole system. Cutting through this layer and the base layer in a disc shape with a slightly larger radius than the loop antenna completed the fabrication.

Fabrication of p+ doping silicon-based pressure module. The fabrication began with p-doping the top silicon layer of an SOI wafer. Undercut etching of the buried oxide layer followed by transfer printing integrated this layer of silicon onto a film of PET (5 μm) coated with a layer of epoxy (SU-8, Microchem Corp.). Photolithography followed by wet and dry etching formed a spiral shape from the silicon membrane. Electron beam evaporation, photolithography and wet etching defined patterns of metal of Cr/Au layers (13nm, 150 nm) for contacts to the ends of the spiral shape. Spin-casting a layer of polyimide and selective etching defined an electrically insulating encapsulation layer with openings aligned to the metal contacts.

Evaluations in pressure sensing. The studies involved a volunteer (male, 29 years old) reclined in a chair with his left forearm gently secured to the armrest. An encapsulated pressure sensor placed on the ventral side of the left forearm captured variations associated with force applied with a fingertip. Qualitatively, the response correlated to the magnitude of the force, with larger values for poking and smaller ones for gentle touch, and transients that correlated to the time duration of the applied force. Continuous pressure led to constant response.

Use in a clinical sleep laboratory. The studies involved a volunteer (male, 27 years old) with 65 wireless sensors mounted at locations across his entire body, with measurements performed while sleeping on a mattress with a pair of reader antennas underneath in a sleep study laboratory at

Carle Hospital, Urbana, Illinois. Each sensor transmitted data for 0.045 seconds every 3 seconds, from 10 pm to 7 am.

3.5 Conclusion

The results presented here illustrate concepts for operating large-scale distributed collections of multimodal wireless sensors across the body, with important capabilities in the context of clinically relevant applications. The thin, soft construction of the devices and their battery-free operation allow them to integrate with the skin in a comfortable, physically "imperceptible" fashion that also avoids any irritation associated with pressure or thermal loads. The basic platforms are compatible with many other types of functionality, including but not limited to measurements of electrophysiology, blood oximetry, heart and respiration rate and photoplethysmograms. Exploiting these modalities, and including other sensing and actuating functionality, represent promising directions for additional research

3.6 Figures

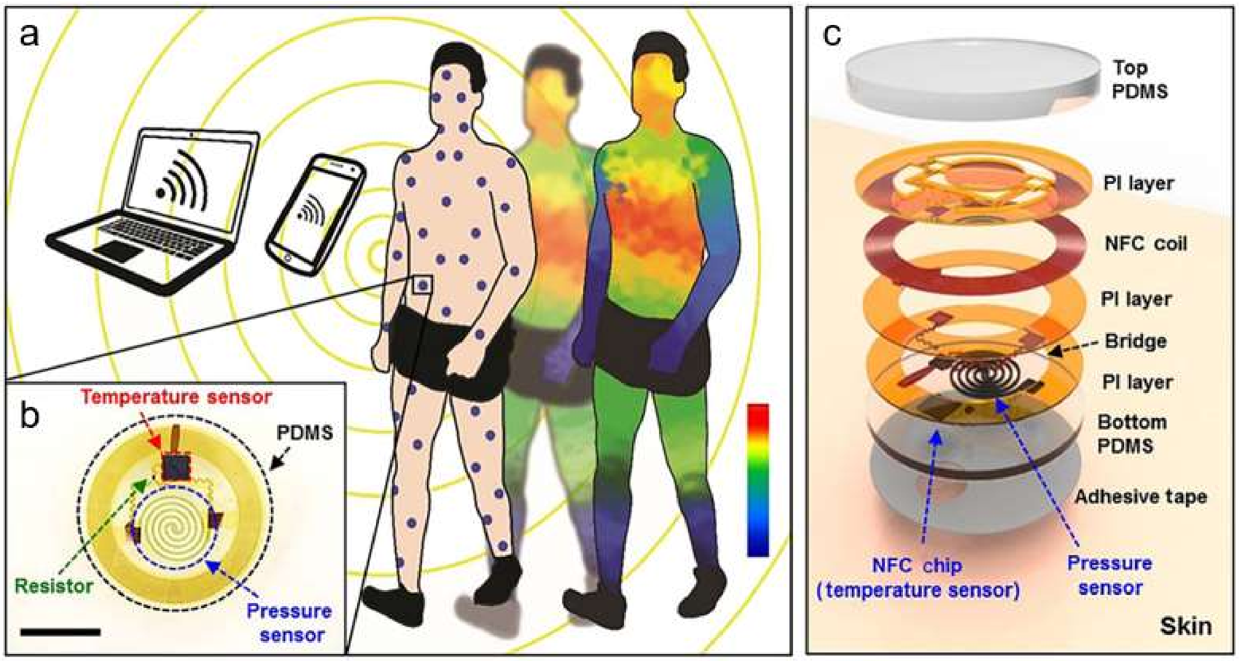

Figure 3.1. Concept illustrations, exploded view schematic illustrations and optical images of wireless, epidermal sensors of temperature and pressure mapping. a) Concept illustration of a collection of skin-mounted sensors across the body, with continuous, wireless transmission of temperature and pressure data in a time multiplexed fashion. b) Top-view optical image (scale bar: 8 mm) of a representative sensor. c) Exploded view schematic illustration of device structure.

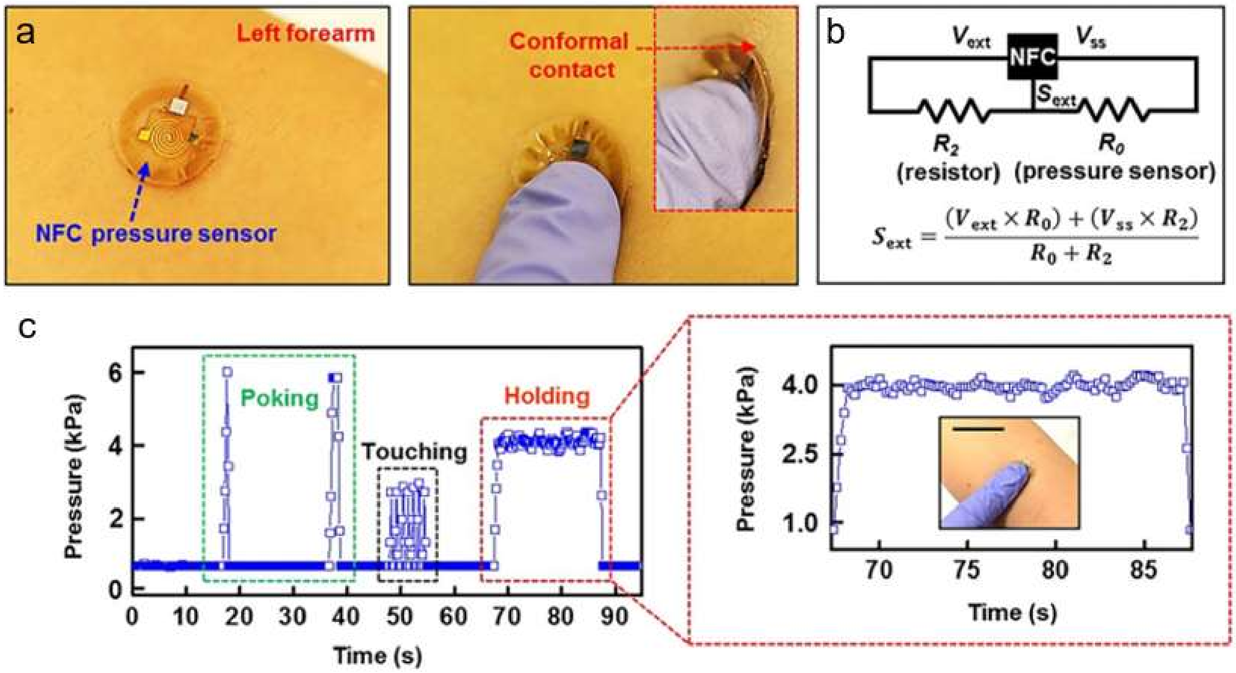

Figure 3.2. Characterization and demonstration of sensors. a) Images of a sensor mounted on left forearm (left) and pressed with a fingertip (right). The inset shows a magnified view to highlight the robust, conformal contact with the skin. b) Equivalent circuit diagram of the pressure sensing part of the device. c) Wirelessly recorded (sampling rate: 6Hz) data with a device on the left forearm during application of various forces with the fingertip (green box: poking; black box: touch; red box: holding). The frame on the right corresponds to the red dashed box on the left, with inset image (scale bar: 4 cm).

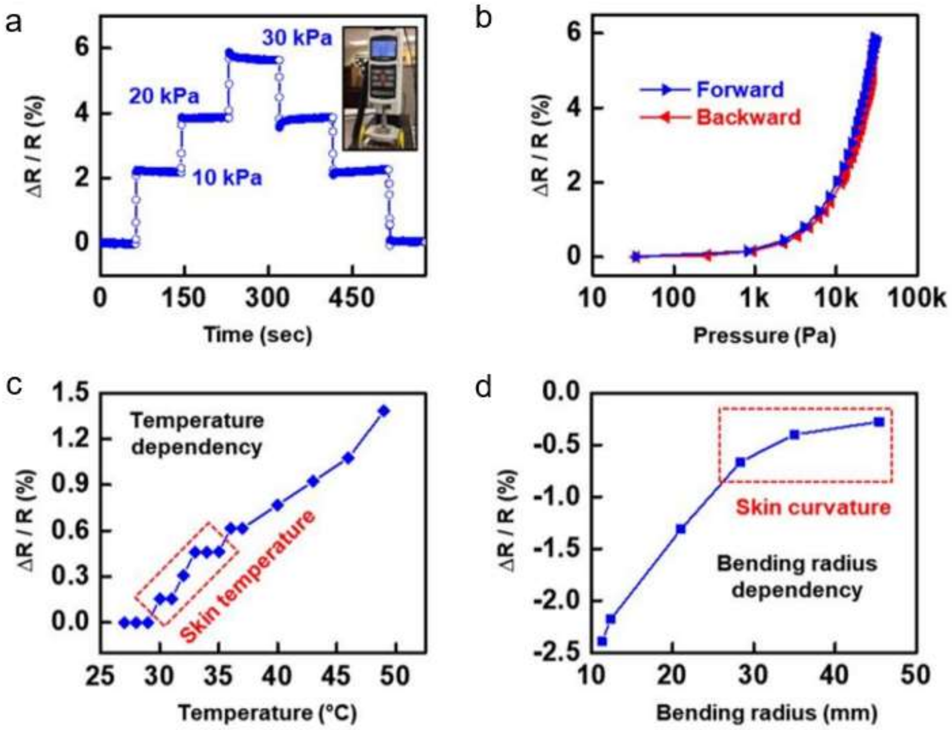

Figure 3.3. Electrical and mechanical characterization and pressure sensor. a) Fractional resistance change of the silicon membrane under various pressure. b) Resistance change under pressure ranged from 0 kPa to 30 kPa. c) Fractional change of resistance due to the temperature variation. d) Fractional change of resistance due to the bending of whole system.

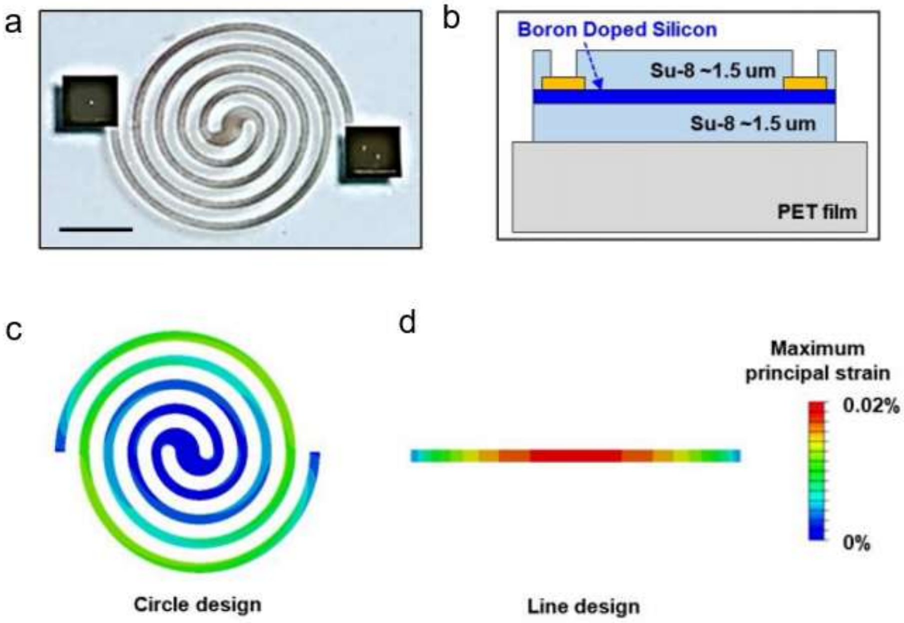

Figure 3.4. Structure and strain distribution of silicon membrane. a) Image of a spiral shaped silicon membrane on a PET film (scale bar: 2mm). b) Side view of the structure of the pressure sensing module. Pressure induced strain distribution on silicon membrane in a (c) circle design and (d) line design.

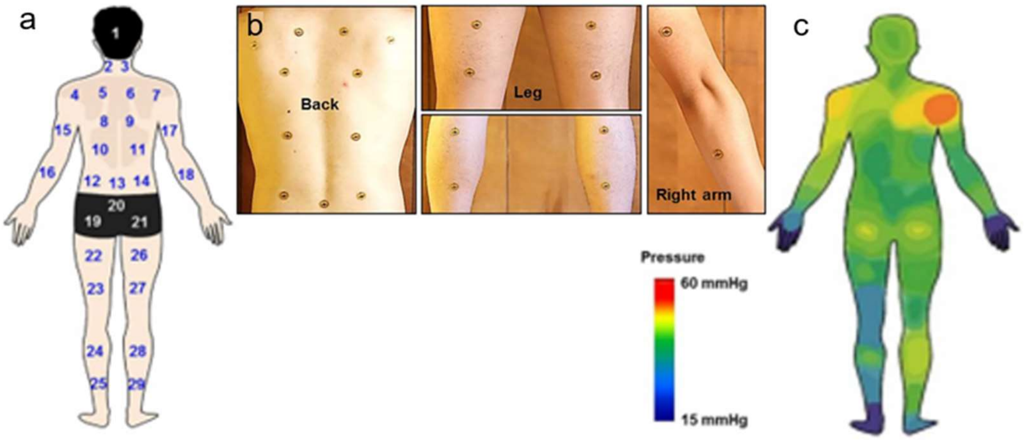

Figure 3.5. Bedside pressure measurement for preventing skin sores, irritation, and ulcers. (a-b) Image of 29 NFC pressure sensors' locations on the back side of body and photo-images of each part of body with sensors. c) Color map of body pressure, generated by measured results. It is easy to determine that shoulder and buttocks receive relatively higher pressure.

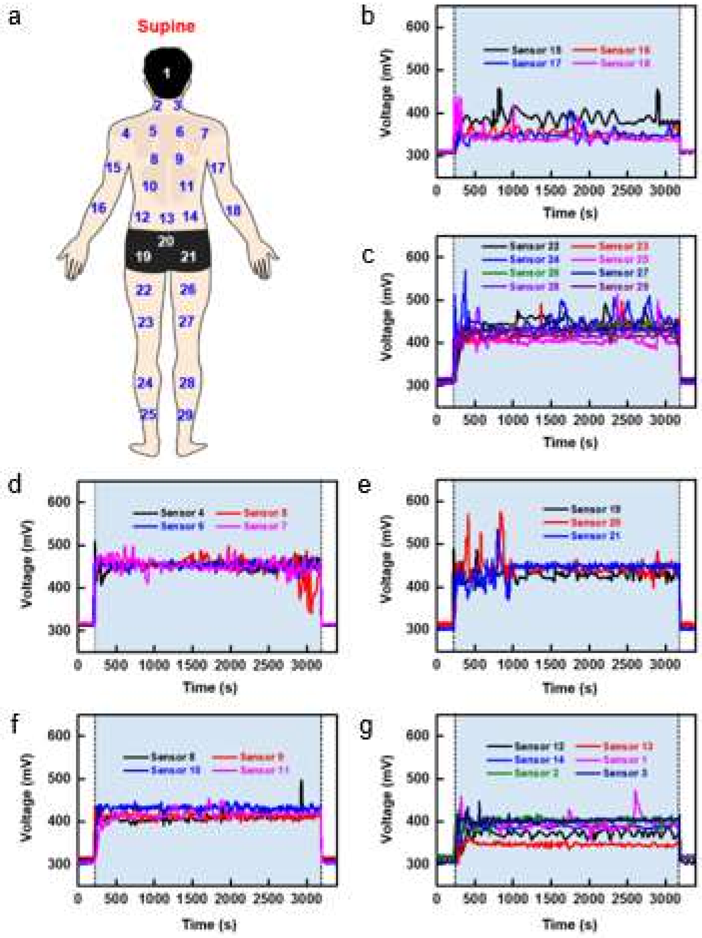

Figure 3.6. Graphs of pressure measurements in a hospital bed while lying at a supine angle of 0°. a) Schematic illustration of the position of the 29 NFC pressure sensors across the (b) arm, 15~18, (c) leg, 22~29, (d) shoulder, 4~7, (e) buttock, 19~21, (f) dorsum, 8~11, (g) lumbar, 12~14; head, 1; neck, 2~3.

3.7 References

[1] J. Kim et al., *Nat. Biomed. Eng.* 1, 0049 (2017).

[2] S.-K. Kang et al., *Nature* 530, 71 (106).

[3] S. K. Vashist et al., *Trands Biotechnol.* 33, 692 (2015).

[4] W. Gao et al., *Nature* 529, 509 (2016).

[5] S. R. Steinhubl et al., *Sci. Transl. Med.* 7, 283rv3 (2015).

[6] E. Monton et al., *IET Commun.* 2, 215 (2008).

[7] A. M. Hussain et al., *Adv. Funct. Mater.* 25, 6565 (2015).

[8] J. Kim et al., *Adv. Funct. Mater.* 27, 1604373 (2017).

[9] A. Araki et al., *Adv. Funct. Mater.* 27, 1604465 (2017).

[10] T. Defloor, Appl. Nurs. Res. 13, 2 (2000).

Chapter 4. Three-Dimensional Multimodal Sensor

4.1 Summary

A tactile sensor that mimics the complex characteristics of cutaneous sensory receptors is a key component in an artificial system for the detection of external stimuli from surrounding physical environments. In particular, a capability of multimodal responses to various external stimuli with high sensitivity and wide dynamic range is essential to reproduce parameters needed for meaningful tactile sensing. In this chapter, unique complex three-dimensional piezoresistive sensors based on monocrystalline silicon nanomembranes as responsive element exhibit separate, simultaneous measurements of multiple mechanical stimuli, such as normal pressure, shear force, bending, and temperature with high mechanical sensitivity and immediate responses in the range of milliseconds. Cycling fatigue test showed mechanically robust and stable operation. Integrated into a wireless platform, the sensor communicates with conventional consumer devices in a robust, reliable fashion without degradation in functionality or performance.

4.2 Introduction

Sensory receptors such as mechanoreceptors, nociceptors, and thermoreceptors are part of the somatosensory system and are found throughout the body including at the skin's surface. Cutaneous sensory receptors play a critical role in detecting stimuli (e.g. mechanical, pain, and temperature) from the surrounding physical environment. Damage to these receptors inhibits an essential mode of defense against physical danger originating at the skin's surface. That is, without cutaneous sensory receptors the body is unable to accurately detect pain, temperature, and mechanical forces such as pressure and strain. The inability of an individual to sense their environment is a serious health hazard and could lead to severe bodily damage or worse. Thus, the development of sensory receptor conduits is critical to bridging the dynamic transduction gap (following receptor damage) between the body and environmental stimuli (*i.e.* conduits that mimic complex touch modalities). Tactile sensors are one such emerging advancement, which also have widespread application elsewhere including real-time health monitoring [1-3], biomedical prosthetics [4,5], electronic skin [6,7], and human-machine interfaces [6,7]. Examples of tactile platforms that mimic touch include sensors to detect and interpret external stimuli, such as pressure, shear, torsion, and temperature, with high sensitivity and wide dynamic range. Many approaches exist for measuring the first and last parameters; the second and third are more challenging, although essential in reproducing object shapes, textures, frictional forces and other parameters needed for meaningful tactile sensing of the physical environment.

Research involving novel methods for measuring tactile stimuli combine exploratory efforts in both materials science and device design to form the base for the physical transduction via capacitive [8-10], piezoelectric [11-13], piezoresistive [14], and triboelectric sensing [15,16]. Commonly used materials for tactile sensors such as ultrathin metallic wire, silicon nanomembranes, carbon nanotubes, liquid metals, nanoparticles, and nanowires on a flexible and/or stretchable support offer the necessary sensing performance in architectures that are compatible with large-area fabrication. Most of these prominent sensors can exhibit exceptional performance, albeit only within a single performance category. New strategies are necessary to develop multifunctional sensing platforms, which meet or exceed all performance criteria. For example, a tactile sensor with two interlocking arrays of Pt-coated nanofibers shows excellent sensitivity response to pressure, shear and torsion [17], but its uniform sensing response across multiple stimuli limits signal decoupling. Use of microstructured pyramid arrays is another example of a multifunctional tactile sensory platform. Here the device can measure and discriminate between normal and shear forces, but operates with linear response only within a small sensing range [18].

This chapter presents a unique three-dimensional (3D) piezoresistive tactile sensor design with responsive monocrystalline silicon nanomembrane (Si-NM) elements that integrate together for in-concert transduction of multiple external stimuli. The 3D tactile sensor resembles a table-like structure (planar surface with four posts) and originates from a two-dimensional (2D) planar precursor that consists of four Si-NM elements. The resulting system provides high sensitivity due to the high gauge factor of monocrystalline silicon in a geometrical construct that enables separate, simultaneous measurements of multiple mechanical stimuli including normal pressure, shear force, and bending, along with temperature. A key feature of the robust 3D device structure is the ability to discern both in-plane and out-of-plane mechanical deformations via separate electrical interfaces to the four piezoresistive Si-NM elements. The multifunctional tactile sensor further integrates with Bluetooth for reliable wireless connection and interface with conventional consumer electronics. Significant components of this chapter have been submitted for publication as S. M. Won et al., “Multimodal sensing with a three-dimensional piezoresistive structure.”

4.3 Results and Discussion

The current fabrication procedure exploits recent advances in the construction of 3D piezoelectric assemblies in which doped Si-NMs integrate onto patterned polyimide (PI) substrates that then transform into 3D hierarchical shapes via mechanically guided buckling by release of prestrain in an elastomeric substrate (Figure 4.1a). The first fabrication step involves establishing p-doped (boron) Si-NM piezoresistors by using previously described impurity diffusion processes [14]. Here, high doping concentration improves the quality of ohmic contacts at the cost of reduced sensitivity. Silicon with boron concentration at ~3×10^{19} /cm^3 represents a good balance for present purposes, with a longitudinal piezoresistance factor of ~40 % of that of silicon at a concentration of 1×10^6 /cm^3 [19]. Precise control of the diffusion temperature and time yields efficient doping reproducibility (less than 10% variation of the mean value within a batch) (Figure 4.2). The 2D precursor consists of two rectangular Si-NM piezoresistors positioned in the vertical direction (aligned head-to-tail and denoted as R2, and R3) and two more Si-NM piezoresistors positioned in the horizontal direction (aligned head-to-tail and denoted as R1, and R4, Figure 4.1b). Deposition of a bilayer of Ti/SiO_2 (5 nm / 50 nm) on the backside of this platform using a shadow mask defines sites for strong bonding to a prestrained silicone substrate. The bonding here involves condensation reactions between ultraviolet-induced ozone treated silicone surface and the exposed SiO_2 layer on the 2D precursor. Slow release of the prestrained platform transforms the 2D precursor into the 3D table-like configuration as shown in Figure 4.1c, where the four Si-NM piezoresistive elements reside at locations of the supporting legs. In a final fabrication step, the device receives a thin coat (~1 mm) of polydimethylsiloxane (PDMS) encapsulant. Figure 4.3 shows detailed fabrication steps.

Responses of each of the piezoresistive elements in this 3D configuration yield distinguishable electrical outputs that allow the independent characterization of a stress tensor (Figure 4.4a). Figures 4.4b-d show output ($\Delta R/R_0$ %) as a function of applied strain for three different loading conditions: normal pressure, shear force, and bending force. Under normal pressure (Figure 4.4b), identical compressive deformations at each of the four legs yield similar strain-induced changes in resistance in all four piezoresistive elements. The measured pressure and resistance values vary linearly with applied strain, with a slope of -0.1 % / kPa, consistent with finite element analysis (FEA) results and a gauge factor of ~50 for the Si-NMs, which is comparable to that reported for other silicon based electromechanical sensors [14]. Uniaxial shear force applied along the direction from R2 to R3 in Figure 4.4c leads to tensile strain and a corresponding increase in resistance at R2, and compressive strain and corresponding decrease in resistance at R3, with negligible strain, and change in resistance, at R1 and R4. Here, the responses of the stretched and compressed legs as a result of shear force are almost equal, ~0.07 % / N, but differ by direction of the change in resistance, and are consistent the direction of the applied shear force. Under the combined loading of pressure and shear force, the changes in resistance at R1-R4 are the linear superposition of those when the load is applied separately, and therefore can be used to determine the pressure and shear force simultaneously (see details in section 4.4). Under a convex bending condition (Figure 4.4d), all sensors experience tensile strain, but with higher values for the two elements along the bending direction (R2 and R3) than those perpendicular (R1 and R4) to it. Again, FEA results suggest a gauge factor of ~50, which agrees well with each response to applied shear force and bending radius.

Another measurement parameter of interest is temperature, where the changes in resistance occur via both strains due to the thermal expansion of encapsulant and the temperature coefficient of resistance (TCR) of Si-NMs. Figure 4.4e shows the resistances of each of the four piezoresistive elements as a function of temperature. FEA based on linear thermal expansion (3.2×10^{-4} /^{o}C) of encapsulant yields ~ 0.035 %/^{o}C of average strains on Si-NMs. The TCR determined for the complete system is ~2.2×10^{-3} /^{o}C, which is comparable to the published value for the p-type silicon at a similar doping concentration [20], and resistance changes due to the calculated strain on Si-NMs. Here, all four piezoresistive elements respond similarly, as expected. All these results show how multiple sensors in a single device react differently to various external stimuli, and suggest their output for decoupling multiple tactile inputs.

Dynamic electrical and mechanical responses with minimal hysteresis are important in practical applications. All constituent materials show approximately linear elastic behavior of ranges of temperature and mechanical forces of relevance for use in human-interfaced systems. Measurements of changes in resistance as a function of frequency during loading and unloading for many cycles under various pressures, all performed with a digital force gauge and multimeter (NI-USB 4065 Digital Multimeter), appear in Figure 4.5. The results show negligible hysteresis upon pressure loading and unloading, perhaps due to the minimal effect by the viscoelasticity of the silicone encapsulant to sensors with relatively large stiffness and modulus materials (e.g., >100 GPa for Si-NM, ~2.5 GPa for PI) (Figure 4.5a). The sensor also exhibits good durability, showing no variation over 1000 cycles under normal pressures of 5 kPa, 10 kPa and 30 kPa (Figure 4.5b). FEA also confirms that the maximum strains in all materials (Si-NMs, Au and PI) are below the fracture limit in these pressure loadings. The sensors respond quickly without delay for loading/unloading under pressures from 5 kPa to 30 kPa (0.2 ms sample rate). The immediate responses in the range of few tens of milliseconds (Figure 4.6) are in good agreement with previously reported sensors based on similar encapsulant and sensing materials [21].

To demonstrate the scalability and the ability to detect the spatial distribution of the stimuli, we fabricated an interconnected 7 x 7 sensor network with a pixel size of ~2 x ~2 mm^2, covering an area of ~14 x ~14 mm^2 (Figure 4.7a). Figure 4.7b-c shows the operation of the array when glass tube (inner diameter, ~17 mm; outer diameter, ~15 mm; weight, 35 g) is positioned on top of sensors. As shown, the pressure exerted by the glass tube induces the compressive deformation at outer sensors and corresponding negative change of resistance, while tensile strain from the shear force toward the tube location results in positive change of resistance at inner sensors (Figure 4.7c). The color contrast clearly indicates the local pressure and shear force distribution consistent with the shape of the glass tube.

Electrically integrating this multimodal sensor with a wireless electronics module (Bluetooth) yields a tether-free measurement system with large-operating-range device suitable for various applications (Figure 4.8a). The fabrication approach integrates the sensors with flexible printed circuit boards (flex-PCBs) as supports for active and passive electronic components such as batteries, Bluetooth chips, power regulators, amplifier, capacitors, and resistors. Here, the platform utilizes the nRF52832 Bluetooth Low Energy protocol, a Li-ion 12 mAh battery (10 hours operation lifetime), and a low energy dropout power converter which regulates the 4.2 V output of the battery to 3.3 V. The platform uses four analog-to-digital converters (ADCs), which operate with 0.6 V reference voltage, 1/6 software gain, and 14-bit resolution, to measure changes in resistance of the four piezoelectric elements. Subtle changes in resistance (~1%) created by external stimuli convert into changes in voltage via a simple voltage divider with reference resistor. The device also has four gain amplifiers set to a gain of 1, but which can be modified for applications that require high sensitivity to low pressure. Custom circuit simulation and data analyzing software allow for fine tuning of the circuit before integration. Figure 4.8b presents wirelessly recorded and recalculated fractional changes of resistance that show responses to shear and normal applied force.

4.4 Methods

Device fabrication. Boron doping (1000 °C, 10 min) defined doped areas on silicon layer (SOI, top silicon ～200 nm, SOITEC INC) for an active region. Removal of the buried silicon oxide layer by use of hydrofluoric acid (HF) releases the top silicon layer from a mother wafer, and enables transfer printing of the resulting Si-NMs onto a receiver substrate composed of polyimide (PI, ~1.5 μm, HD microsystems INC), PMMA (~100 nm, MicroChem INC), and a glass slide from top to bottom. Reactive ion etching (RIE, SF_6, 30 mTorr, 50 W, 20 sccm, 200 s) and e-beam evaporation processes (Cr/Au, 5/200 nm) were used to form silicon pixels and metal interconnects, respectively. Coating a thin layer of PI (~1.5 μm) as a passivation layer and forming a mesh structure by RIE (O_2, 100 mTorr, 100 W, 20 sccm, 15 min) completed the formation of a 2D precursor. Dissolving a PMMA layer with acetone released the circuit from the silicon wafer. Retrieving a 2D precursor onto a PDMS stamp and evaporating layers of Ti/SiO_2 (5/100 nm) selectively onto bonding sites on the exposed backside surface prepared the system for a covalent bonding onto a prestrained silicone elastomer pretreated by exposure to UVO (5 min). Releasing the prestrain led to geometrical transformation of the 2D precursor into a 3D configuration. Final PDMS coating (~1 mm) completed the fabrication.

Measurement setting. The measurement setup consists of a customized vertical and horizontal stage used with a force gauge (Mark-10), and digital multimeters (NI-USB 4065 Digital Multimeter) for the electrical resistance measurement. For shear force measurement, the sensor is attached on the ground and the force gauge pulls the polyimide film (width of ~1 cm), adhering on the sensor.

Simultaneous determination of pressure and shear forces. Under pressure P, the relative resistance changes $\frac{\Delta R}{R_0}$ in the piezoresistors R1~4 are

$$\left(\frac{\Delta R}{R_0}\right)_{1\sim4} = C_P P \tag{4.1}$$

where $C_P \approx -0.1\%/\text{kPa}$ and R_0 is the resistance without pressure. Under shear force F_x along *x*-direction, the resistance changes are

$$\left(\frac{\Delta R}{R_0}\right)_2 = -\left(\frac{\Delta R}{R_0}\right)_3 = C_F F_x, \ \left(\frac{\Delta R}{R_0}\right)_1 = -\left(\frac{\Delta R}{R_0}\right)_4 = 0 \tag{4.2}$$

where $C_F \approx 0.07\%/\text{N}$. Similarly, under shear force F_y along *y*- direction,

$$\left(\frac{\Delta R}{R_0}\right)_4 = -\left(\frac{\Delta R}{R_0}\right)_1 = C_F F_y, \ \left(\frac{\Delta R}{R_0}\right)_2 = \left(\frac{\Delta R}{R_0}\right)_3 = 0 \tag{4.3}$$

When the pressure P and shear forces F_x, F_y are applied simultaneously, the resistance changes are the linear superposition of Eqs. (1)-(3) for small deformation. Therefore P, F_x and F_y can be determined from $\left(\frac{\Delta R}{R_0}\right)_{1\sim4}$ as

$$P = \frac{1}{2C_P}\left[\left(\frac{\Delta R}{R_0}\right)_2 + \left(\frac{\Delta R}{R_0}\right)_3\right] = \frac{1}{2C_P}\left[\left(\frac{\Delta R}{R_0}\right)_1 + \left(\frac{\Delta R}{R_0}\right)_4\right] \tag{4.4}$$

$$F_x = \frac{1}{2C_F}\left[\left(\frac{\Delta R}{R_0}\right)_2 - \left(\frac{\Delta R}{R_0}\right)_3\right] \text{ and } F_y = \frac{1}{2C_F}\left[\left(\frac{\Delta R}{R_0}\right)_4 - \left(\frac{\Delta R}{R_0}\right)_1\right] \tag{4.5}$$

4.5 Conclusion

The results presented here demonstrate the use of piezoresistive sensors in 3D configuration to interact with various tactile stimuli. The output tells the types and magnitudes of various external input stimuli, such as pressure, shear, bending, and temperature. The combination of sensor and Bluetooth platform is able to collect, transmit, and analyze the data in a fully wireless manner, which is more suitable for wearable, biomedical, or human-robotic devices. This system and set of demonstration studies suggest new opportunities for the use of 3D dynamic platforms in sensors/actuators as the basis for advanced biomedical or health monitoring systems.

4.6 Figures

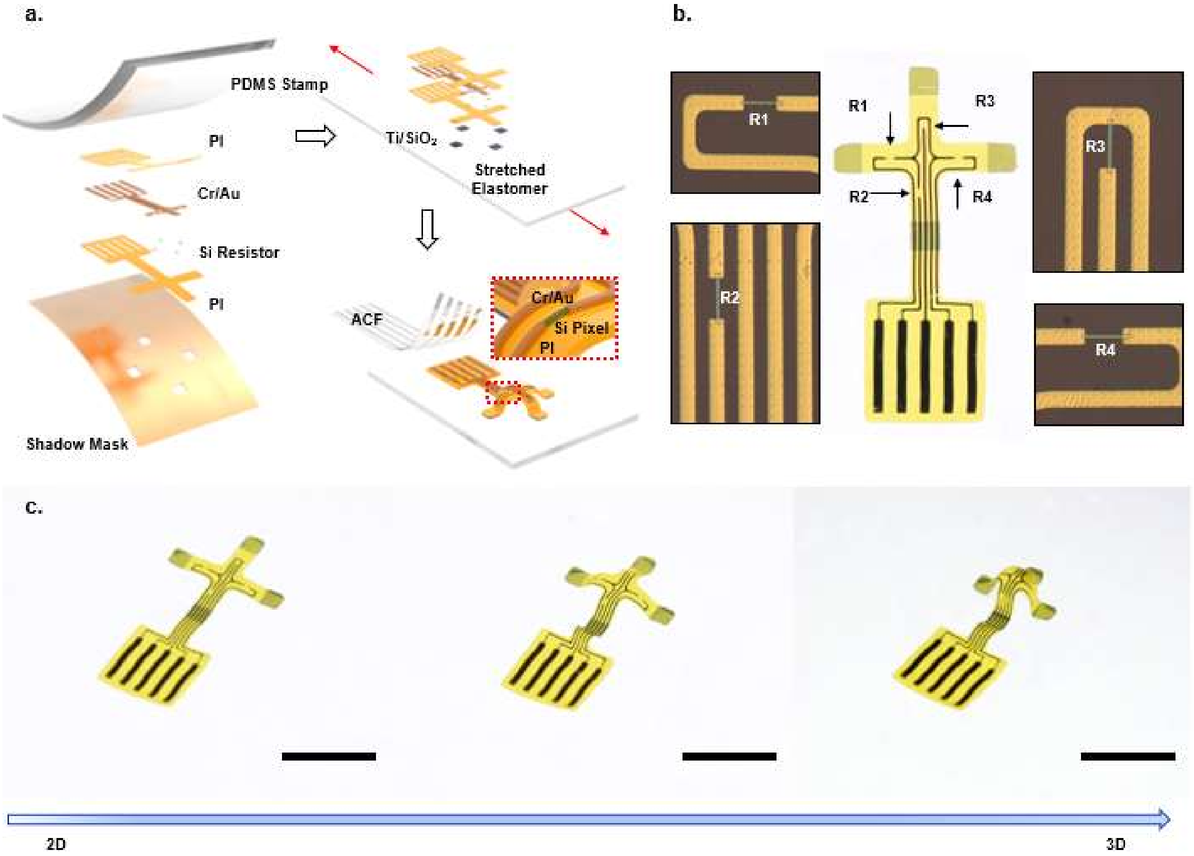

Figure 4.1. Materials and construction of 3D piezoresistive tactile sensor on an elastomer substrate. a) Schematic illustration for the fabrication of 3D tactile sensor after retrieving the circuit onto a PDMS stamp and deposition of Ti/SiO2 onto defined bonding site on the backside (left). Transfer printing process delivers the circuit onto a prestrained silicone substrate (top right). Release of strain transforms the piezoresistive sensor in 3D table-like configuration (bottom right). b) Optical microscope image of 2D precursor that has two piezoresistors (R2 and R3) in the vertical direction and two (R1 and R4) in horizontal direction. c) Release of the prestrained silicone to transform the 2D structure (left) into a 3D configuration (right) (scale bar: 2 mm).

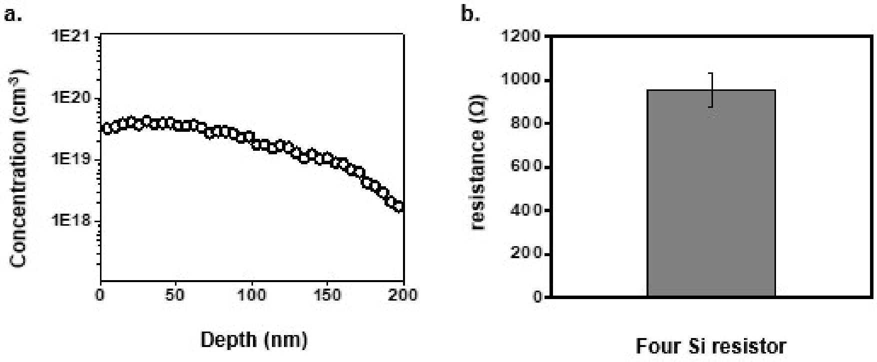

Figure 4.2. Silicon nanomembrane characterization. a) Secondary ion mass spectrometry profile of boron distributed throughout the thickness of silicon nanomembrane. b) Variation of Si-NM resistance in a single batch.

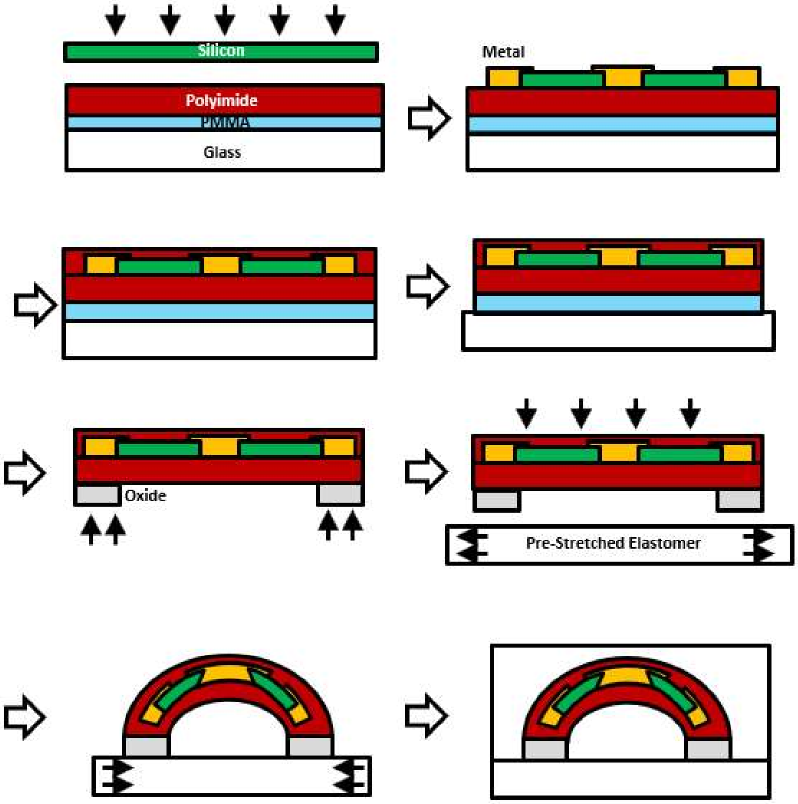

Figure 4.3. Schematic illustration to show the process of 3D tactile sensor fabrication.

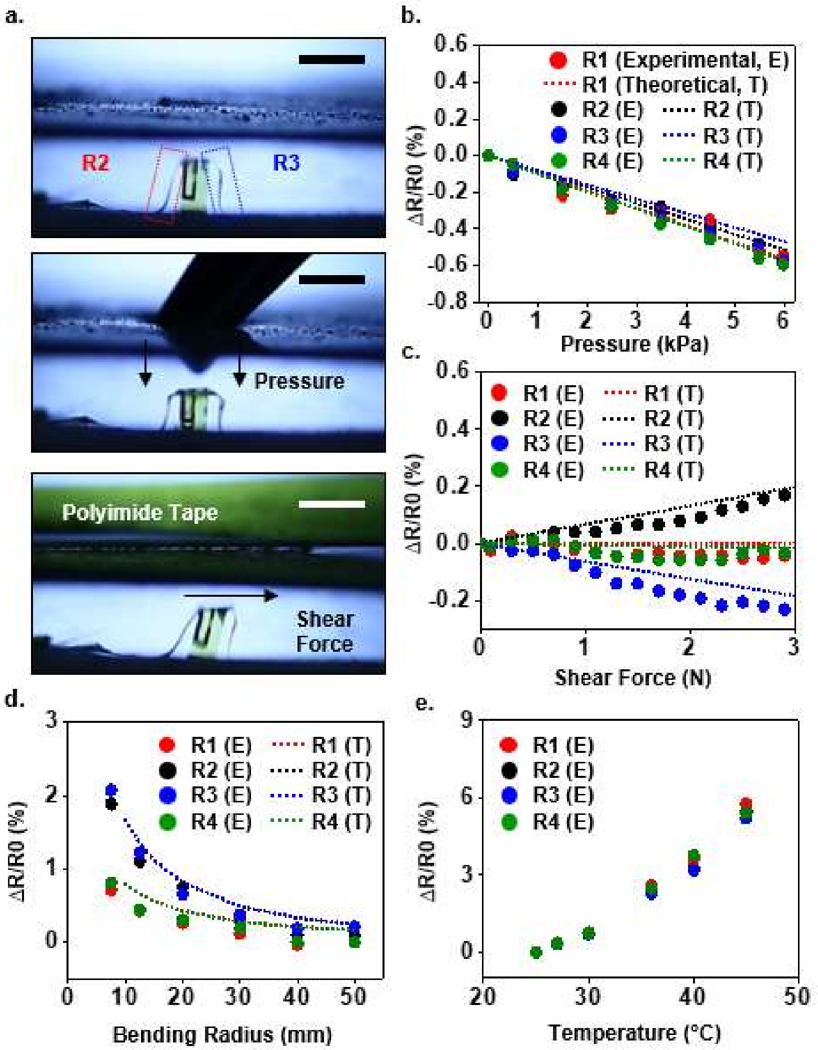

Figure 4.4. Characterization of tactile sensor in response to normal pressure, shear force, bending, and temperature. a) Optical image of tactile sensor without stimulus (top), under normal pressure (middle), and shear force (bottom) (scale bar: 2 mm). Fractional change in resistance of four piezoresistors as a function of the applied normal pressure (b), shear force (c), bending (d), and temperature variation (e).

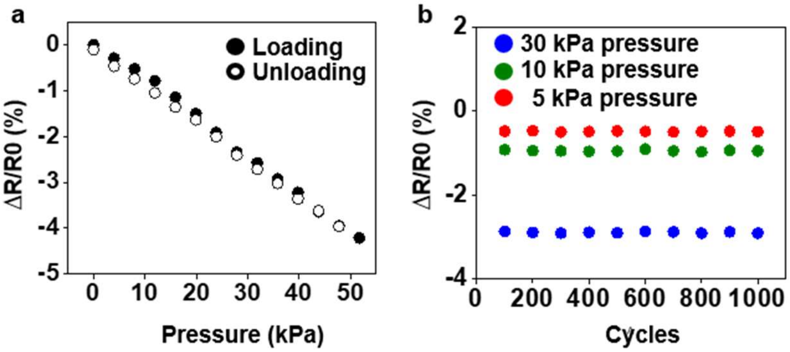

Figure 4.5. Evaluation of reliabilities. a) Hysteresis curves for the sensor corresponding to normal pressure loading. b) Fractional change of resistance at different stages of fatigue testing, which involves 1000 cycles, to different normal pressures indicated in the legend.

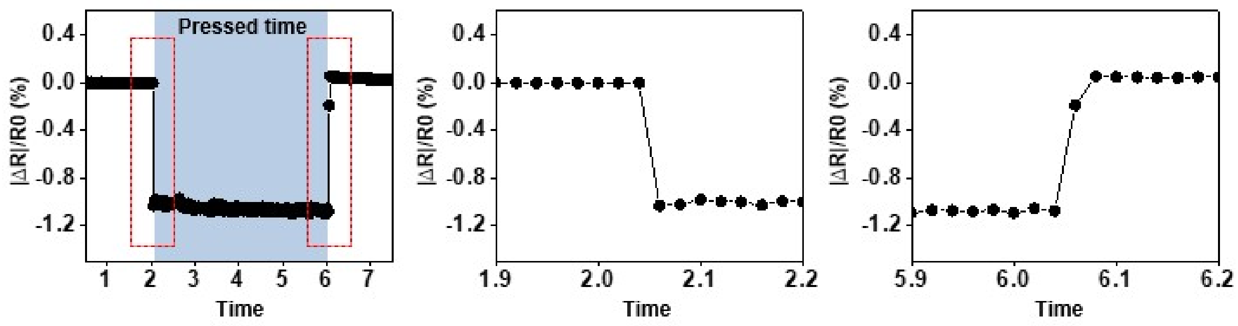

Figure 4.6. Evaluation of response time. The response times of a few tens of milliseconds are in good agreement with reported sensor with similar sensing material and substrate/encapsulations [21].

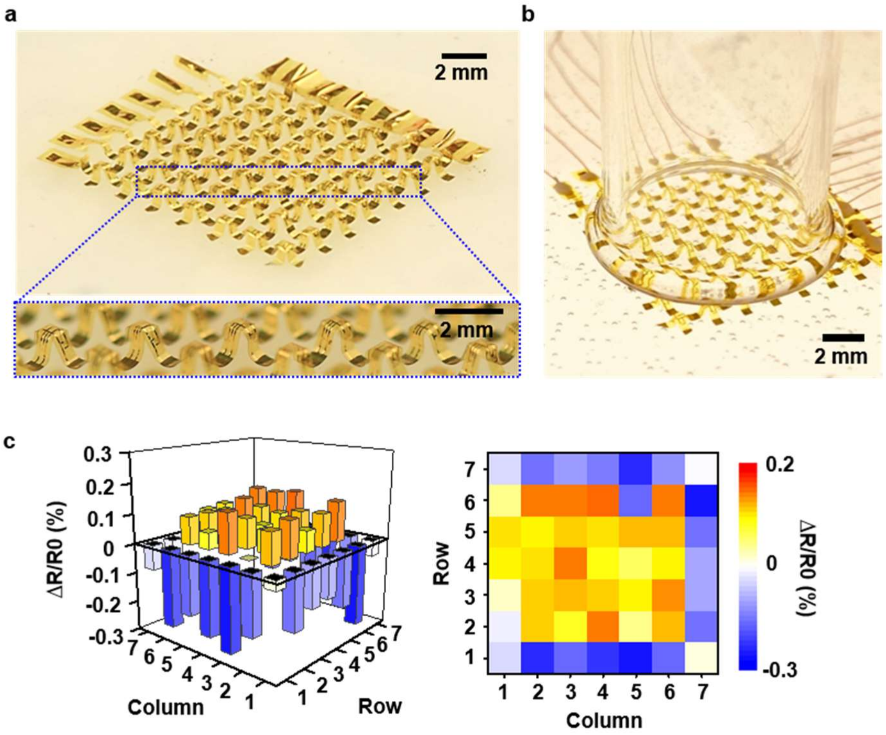

Figure 4.7. Large-area integration. a) Optical image of entire 7 x 7 sensor array and magnified unit cells (inset) to measure the spatial distribution of external loadings. b) Image of the device with glass tube placed on top. c) The resulting three-dimensional (left) and two-dimensional (right) resistance change profile of sensors in array.

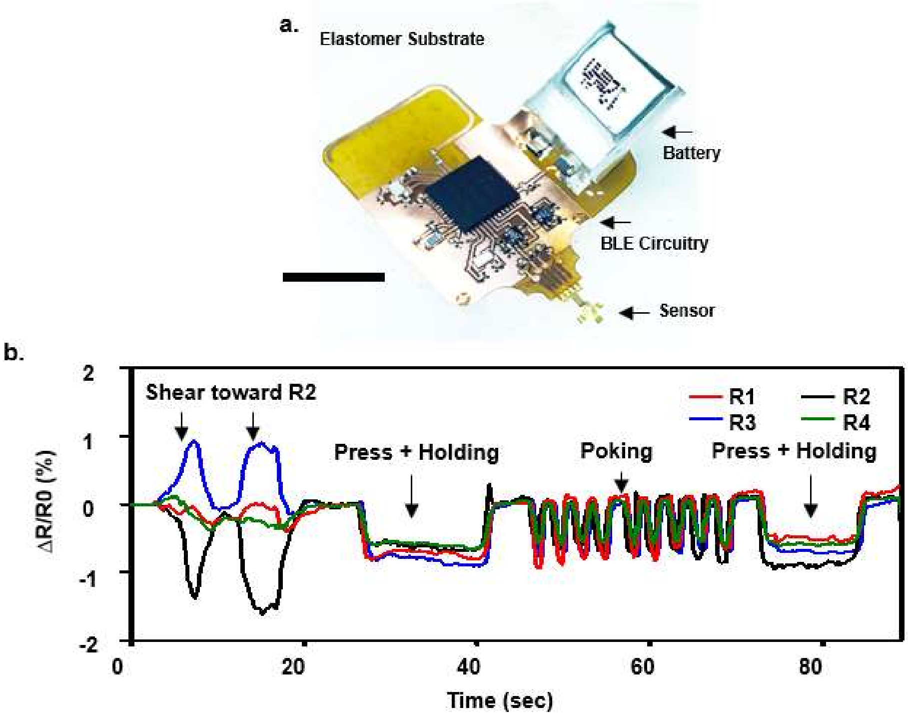

Figure 4.8. Wireless data acquisition. a) Optical micrograph of 3D tactile sensor, fully integrated with a wireless electronics module, including flex PCB, surface-mounted electronic components, and silicone substrate/encapsulant (scale bar: 4 mm). b) Wirelessly recorded sensing data that shows responses to shear force and normal pressure.

4.7 References

[1] M. Amjadi et al., *Adv. Funct. Mater.* 26, 1678 (2016).

[2] Y. Zhang et al., *Sens. Actuators A Phys.* 253, 165 (2017).

[3] D. Y. Choi et al., *ACS Appl. Mater. Interfaces* 9, 1770 (2017).

[4] S. K. Yildz et al., *Sens. Actuators A Phys.* 247, 514 (2016).

[5] V. Sencadas et al., *Sens. Actuators A Phys. 266*, 56 (2017).

[6] H.-J. Kim et al., *Sci. Adv.* 3, e1701114 (2017).

[7] Y. R. Jeong et al., *NPG Asia Mater.* 9, e443(2017).

[8] S. Wan et al., *Carbon* 114, 209 (2017).

[9] Y.-M. Chen et al., *Nanoscale* 8, 3555 (2016).

[10] V. Mitrakos et al., *Micromachines* 8, 41 (2017).

[11] J.-H. Lee et al., *Adv. Funct. Mater* 25, 3203 (2015).

[12] Z. Chen et al., *ACS Nano* 11, 4507 (2017).

[13] C. Dagdeviren et al., *Extreme Mechanics Lett*. 9, 269 (2016).

[14] S. M. Won et al., *IEEE Trans Electron Devices* 58, 4074 (2011).

[15] K. Y. Lee et al., *Adv. Energy Mater*. 6, 1502566 (1016).

[16] P.-K Yang et al., *ACS Nano,* 9, 901 (2015).

[17] C. Pang et al., *Nature Mater*. 11, 195 (2012).

[18] C. M. Boutry et al*., Science Robotics* 3, eaau6914 (2018).

[19] R. Hull, *Properties of Crystalline Silicon*. London, U.K. pp. 214-215 (1999).

[20] P. Norton and J. Brandt, *Solid State Electron,* 21, 969 (1978).

[21] S. Han et al., Sci. Transl. Med. 10, eaan4950 (2018).

Chapter 5. Wireless Monitoring and Optogenetic Modulation of Bladder Function

5.1 Summary

Bioelectronic technologies that modulate activity of the peripheral nervous system offer powerful options in targeted treatment of organ dysfunction and pain. As an example, electrical stimulation of the sacral nerve provides an effective intervention for bladder dysfunction. Due to the diverse functions of the sacral nerve, this stimulation can have off-target effects and produce pain and discomfort. Furthermore, the continuous mode of stimulation at the electrode/tissue interface means that these unwanted side effects may be persistent. Here we introduce a miniaturized, fully implantable wireless bio-optoelectronic system that circumvents these challenges by monitoring and modulating bladder function in an active, closed-loop fashion through optogenetic, as opposed to electrical, modulation of bladder-projecting sensory afferents. These platforms use soft sensors to capture bladder activity in real time and data analysis algorithms to identify pathological patterns of voiding as they occur, and they trigger optogenetic modulation via proximally located microscale light-emitting diodes to attenuate increased voiding associated with bladder inflammation. In addition to serving as the foundation of an advanced, electroceutical-based intervention for bladder dysfunction, this system embodies a generalizable idea for bio-optoelectronic approaches to treating disease.

5.2 Introduction

Bioelectronic technologies that modulate activity of the peripheral nervous system offer powerful options in targeted treatment of organ dysfunction and pain. These electroceutical technologies modulate the peripheral nervous system (PNS) to provide therapeutic effects as treatments for a wide range of diseases such as diabetes, overactive bladder, pain, gastrointestinal disorders and hypertension, among others [1-8]. The goal of these approaches is to develop approaches that complement traditional pharmacological strategies, through capabilities in targeted interventions with minimal side effects. Existing and emerging technologies of this type rely largely on electrical stimulation to provide neuromodulation of organ function or pain. Although recent advances in biocompatible and bioresorbable electronic systems [9,10] significantly expand the prospects for bioelectronic medicines, the foundational concepts in electrical stimulation are nearly 100 years old and remain fraught with persistent, daunting challenges in achieving stable, noninvasive operation at the biotic/abiotic interface.

One example of a successful electroceutical intervention is sacral nerve stimulation to attenuate symptoms associated with overactive bladder, urinary incontinence and interstitial cystitis/bladder pain syndrome [1,11,12]. Current approaches, however, utilize continuous stimulation protocols that can cause discomfort and pain, particularly when treating bladder symptoms that can be intermittent in nature (e.g. a sudden urgency to urinate) [13]. This mode of direct electrical stimulation targets large nerve bundles to produce therapeutically relevant neuromodulation, but without organ or cell type specificity, as these bundles often contain nerve fibers that innervate multiple structures. Furthermore, direct physical coupling of conventional electrodes to nerves can produce injury and inflammation, therefore complicating the use of electroceuticals for chronic conditions [14-16].

The combined use of biophysical/chemical sensors and active, closed-feedback control can improve the viability of these technologies [7,8]. Examples include physiological signals such as blood glucose sensors with artificial pancreas devices [17] and electrical monitors with implantable defibrillators for cardiac dysrhythmias [18] to determine the timing and duration of pharmacological and bioelectronic interventions, respectively. Expansion of such closed-loop interventions to treat other PNS diseases, particularly those that address conditions such as bladder disorders where sensor integration represents an extreme challenge, could lead to reduced side effects, increased efficacy and improved consistency of therapeutic results. An unexplored area that could greatly expand the range of possibilities is in feedback schemes that exploit sensors of biophysical responses, such as changes in dimension, shape, pressure, flow, mechanics, temperature and other essential physical parameters, as opposed to more traditional biopotential or biochemical queues.

This chapter introduces a fully implantable, miniaturized bio-optoelectronic platform that represents an advance for this emerging field of engineered medicines, via the use of (1) a proximity mode, optical stimulation interface to the nerves that exploits microscale inorganic light emitting diodes (μ-ILEDs) to activate opsins, (2) a soft, precision biophysical sensor system that allows continuous measurements of organ function, and (3) a control module and data analytics approach that allows coordinated, closed-loop operation of the system to eliminate pathological behaviors as they occur in real time. This all-optical scheme for neuromodulation bypasses limitations in chronic stability and noninvasive operation of traditional, contact-based electrical approaches and it also provides straightforward means for cell-type-specificity in stimulation. Thin, mechanically soft physical embodiments and battery-free, fully wireless designs enable temporal specificity and active control of stimulation timed to periods of organ dysfunction. This chapter highlights these ideas in a demonstration system for continuous monitoring of bladder function using a stretchable strain gauge with ultralow modulus, real-time data analytics to identify pathological behavior based on the sensor responses, and automated, closed-loop optogenetic neuromodulation of bladder sensory afferents to normalize bladder function in the context of acute cystitis. Significant components of this chapter were published as A. D. Mickle, S. M. Won et al., "A wireless closed-loop system for optogenetic peripheral neuromodulation," *Nature* 565, 361-365, 2019.

5.3 Results and Discussion

The fully implantable, wireless neuromodulation system introduced here utilizes a soft, low modulus implantable strain gauge to monitor bladder function and μ-ILEDs to control virally expressed inhibitory opsins expressed in the bladder sensory afferents. To achieve the desired closed-loop control of bladder dysfunction, the system includes five interconnected sub-systems: (1) a low-modulus, stretchable strain gauge that encircles the bladder to measure bladder activity (filling/voiding), (2) a pair of μ-ILEDs that deliver light directly to the bladder for optogenetic neuromodulation, (3) a thin, soft base-station that inserts between the abdominal skin and muscle for bidirectional communication and wireless control of the μ-ILED actuators, (4) a wireless harvesting unit that distributes power to the entire system and (5) customized software deployed on a handheld device to enable real-time visualization, storage and analysis of operational data, and to provide an automated control interface for setting illumination protocols and parameters for open- or closed-loop interventions (Figure 5.1a and b). Sub-systems (1) & (2) and (3) & (4) integrate into two separate modules, electrically connected within the body of the animal by insulated fine wires. This system provides a critical advantage over other real-time bladder function measurements in that it does not require direct nerve interfaces or invasive pressure monitoring systems. Implantation of sub-systems (1) & (2), referred to as the optoelectronic sense/stimulate (OSS) module, involves conformal circumferential interfacing of the strain gauge with the bladder, secured by an integrated buckle with a small dissolvable suture to the detrusor muscle. Subsystems (3) & (4), referred to as the wireless control/power (WCP) module, compose a thin, low modulus component that inserts subcutaneously in the abdomen (Figure 5.1c and d). One month after implantation, the OSS and WCP modules both remain in their original positions (Figure 5.1e), with no signs of degradation in functionality or performance.

The OSS module combines a thin (15 μm) layer of silicone doped with carbon-black as a strain gauge, with a pair of μ-ILEDs for optogenetic stimulation (Figure 5.2a). A low modulus silicone material serves as the substrate and overall encapsulation. Photolithographically patterned traces of copper on a dry-etched film of polyimide provide the electrical interconnections. The entire platform is noninvasively fastened around the bladder, such that dimensional changes in the bladder that occur with natural filling and voiding stretch the strain gauge. Resulting changes in resistance correlate to bladder size. The shape of the OSS module and its low modulus construction allow for reliable detection of bladder expansion and contraction without constraint on normal bladder function. Strain-stress curves obtained by dynamic mechanical analysis indicate that the modulus of the thin layer of doped silicone for the strain gauge, after encapsulation above and below with undoped silicone (40 μm), is 70 kPa. Finite element analysis of experimental measurements of changes in the dimensions of the bladder caused by filling with saline solution suggest that the modulus of the material that makes up the bladder walls is in a range between 10 and 40 kPa, consistent with previous reports [19]. These modulus values allow finite element analysis simulations of the bladder radius, assuming an ellipsoidal shape, during expansion with and without the strain gauge (Figure 5.2b). Deformations of the bladder due to the presence of the strain gauge are less than 2% of the overall expansion due to filling, consistent with negligible mechanical loading. In vivo measurements of cystometric pressures during filling and voiding show no effects of the device, consistent with FEA results (Figure 5.2c).

The μ-ILEDs are mounted on a thin, flexible substrate of stainless steel (25 μm) and exploit transparent layers of polyisobutylene and polydimethylsiloxane as frontside encapsulation. Activation of the μ-ILEDs causes 44.3 ± 10.9 μW of light (540 nm) to pass through the full thickness (non-stretched) bladder wall. The small dimensions of the μ-ILEDs and the high thermal conductivity of the stainless-steel result in efficient dissipation of thermal load associated with operation, even with continuous illumination. Measurements indicate that one hour of constant illumination leads to increases in the temperature of the contacting tissue that are less than 1˚C.

To communicate strain gauge sensor readings to a user interface, the WCP module incorporates a low-powered radio frequency (RF)-embedded microcontroller and wireless power management circuitry. Power delivery to the WCP module occurs wirelessly via resonant inductive coupling through a three-coil wireless power transfer (WPT) link (Figure 5.2d-e). The transmitter side incorporates a 13.56 MHz radio frequency identification (RFID) driver, impedance matching circuitry, and a primary coil. A secondary resonating coil, wrapped around the bottom of the cage to enhance the efficiency of power transfer, and a load coil in the WCP module constitute the receiver end. Matching the impedance of the receiver coils such that they resonate at 13.56 MHz yields a loosely coupled WPT system, designed to alleviate sensitivities to mismatches in antenna characteristics and allow the WPT coverage throughout the rat cage. The received voltage on the parallel-resonant load coil is rectified with a full-bridge rectifier and regulated using a charge pump converter to simultaneously power the wireless system and charge a pair of supercapacitors within the WCP module. These supercapacitors act as a short-term energy buffer (two 70 mF supercapacitors with 720 mJ at 3.2 V) during periods when the wirelessly received power is insufficient to operate the system, typically caused by rotations of the animal (most commonly, rearing upward for one to five seconds) that lead to an angular mismatch between the load antenna on the WCP module and the primary transmission antenna. The supercapacitors can power the system for over 3 minutes without external power; wireless charging occurs in ~30 s when the transmitting antenna outputs 4 W. A thin layer of copper (12 µm) and a ferrite shield placed at the base of the WCP module and patterned in the geometry of its constituent components magnetically shield the system from the incoming RF to minimize parasitic heating and noise of electronic components.

The full closed-loop optogenetic control (CLOC) system accurately monitors bladder activity, where large decreases in resistance (decreases in bladder size) correlate with voiding events as measured by a metabolic cage (Figure 5.3a). Importantly, implantation of the CLOC system does not significantly affect bladder cystometric properties 7 days after implantation compared to animals that received a sham implantation surgery. This result provides confirmation that the strain gauge does not constrict the bladder, and that there is no significant formation of fibrosis around the bladder, which could decrease bladder compliance. Additionally, no significant inflammatory response, alterations to gait, movement, or weight changes occurred 7 days after device implantation compared to animals receiving sham surgery. Altogether, these results indicate that the implanted CLOC system accurately measures bladder function, has minimal effect on bladder physiology, and does not cause detectable harm or distress to the animal.

An optogenetic strategy allows for modulation of bladder function, enabled by injection of a herpes-simplex viral (HSV) vector containing genetic payload to express the inhibitory opsin archaerhodopsin 3.0 (Arch) [20] directly into the bladder wall. This approach enables specific neuromodulation of sensory afferents innervating the bladder as differentiated from traditional electric stimulation of the sacral root, which activates neurons innervating the colon and other pelvic structures. Because HSV vectors provide tropism for sensory neurons [21], this injection results in expression of Arch in sensory neurons innervating the bladder; Arch protein is detectable in peripheral terminals in the bladder wall, as well as cell bodies of the dorsal root ganglion (DRG) neurons 7 days after injection. Injection of viral vectors alone does not significantly alter cystometric properties or cause alterations in mast cell degranulation, a marker for inflammatory response, 7 days after injection. Isolated bladder-projecting DRG neurons transduced with Arch-eYFP demonstrate reduced neuronal excitability on exposure to 530 nm light. Additionally, Arch activation reduces neuronal excitability in DRGs cultured from human donors and transduced with Arch-eYFP. Together these results illustrate that HSV vectors transduce the inhibitory opsin Arch in bladder projecting sensory neurons without overt tissue damage, and that activation of Arch in rat or human DRG neurons decreases neuronal excitability.

Anesthetized cystometry, a measure of bladder physiologic properties, reveals the effect of Arch-mediated neuronal inhibition on bladder function. In rats that express Arch-eYFP in bladder-projecting neurons, illumination of the bladder significantly increases the intercontraction interval (ICI) compared to rats expressing only eYFP (Figure 5.3b-c), as demonstrated with implanted OSS modules and intravesicular catheters to measure bladder pressure. These groups, however, show no differences in peak, baseline, or threshold pressures. Similar degrees of ICI delay appear in data collected using the strain gauges and intravesicular pressure sensors, providing further evidence that the OSS module accurately measures bladder function.

Implanting CLOC platforms in animals that express Arch-eYFP or eYFP allows for the assessment of Arch activation on normal voiding in awake freely moving animals. In these rats, bladder illumination does not alter void frequency, or the time to first void, in the 3-hour illumination period, in contrast to Arch-eYFP/LED-ON, eYFP/LED-ON and virus-injected/LEDOFF groups. Rats previously treated with cyclophosphamide (CYP, 75 mg/kg, i.p.), which induces a model of voiding dysfunction [22], show significant increases in the frequency of voids. In CYP-injected rats, bladder illumination results in a significant decrease in the number voids in the Arch-eYFP/LED-ON group compared to eYFP/LED-ON and virus-injected/LED-OFF groups, during the 3 hours post-injection (Figure 5.3d-e). Additionally, a significant increase in the time to the first void after CYP injection appears in the Arch-eYFP/LEDON group compared to the eYFP/LED-ON and virus-injected/LED-OFF groups (Figure 5.3e).

Fully automated utilization of the CLOC system requires algorithmic identification of strain gauge data signatures of abnormal bladder voiding. Real-time signal processing methods classify abnormal bladder activity based on identification of voiding events, indicated by relatively prolonged increases in strain gauge resistance (increases in bladder size) followed by rapid decreases (rapid decreases in bladder size). Preliminary “training” data from the strain gauge collected concurrently with data from the metabolic cage facilitates the development of signal processing methods that accurately differentiate voiding events from noise due to motion artifacts or other parasitic signals. Voiding events are identified by filtering the raw strain gauge data (1 Hz sampling rate) with a 60-point moving average, down-sampling the results to 0.25 Hz, and then computing the derivative of these processed data (Figure 5.4a). These steps suppress high-frequency noise associated with nonvoiding events, such as internal organ movement and motion artifacts, but retain voiding data that occur on timescales of 10-30 s. Analysis of these data sets shows that voiding events correlate strongly with three consecutive values of the derivatives that are less than a preset threshold. The value of this preset threshold corresponds to the standard deviation of one hour of normalized strain gauge data, collected on each animal/device, to account for device-to-device and animal-to-animal variability. A final step rejects false voids as instances of larger rapid increases in the strain gauge response, a movement artifact that would represent a nonfeasible bladder expansion (Figure 5.4b). Altogether, this algorithm identifies voids with >85% accuracy in naïve animals and >95% after induction of abnormal voiding with CYP. Further analysis of the training data set found that three voids within one hour indicate abnormal voiding behavior associated with CYP injection, and do not occur in normal voiding patterns.

Closed-loop operation involves the execution of a software application that enables real-time processing of the signal, logging of the response of the strain gauge for subsequent analysis, activating/deactivating of the μ-ILEDs and implementing the analysis algorithms described previously. The application also includes a user interface to define calibration variables such as derivative thresholds for identifying voiding events and normal contraction intervals. When the patterns of voiding meet the criteria defined by these inputs values, the μ-ILEDs activate for 2 hours, as determined to be effective in reducing the voiding frequency after CYP-induced inflammation. Seven days after viral transduction of Arch-eYFP or eYFP and CLOC system implantation, the closed loop software was initiated (Figure 5.4c). The closed-loop software does not activate the μ-ILEDs prior to CYP-injection. However, ~4 hours after CYP injection (150 mg/kg, i.p.) the closed loop software activates the μ-ILEDs (Figure 5.4d). Activation of the μ-ILEDs results in a reduction in the frequency of voiding in the Arch-eYFP transduced animals compared to the eYFP controls, similar to the experimenter μ-ILED experiments (Figure 5.4d). These results demonstrate the ability of the CLOC system to automatically recognize abnormal voiding patterns based on algorithmic detection of voiding events and conditional activation of μ-ILEDs to attenuate this CYP-induced increased voiding.

5.4 Methods

Fabrication of the wireless control/power (WCP) module. The first step involved spin-casting a polyimide (PI) film on a copper foil. Laminating the sheet, with the PI side down, onto a glass slide coated with polydimethylsiloxane (PDMS) enabled patterning of the copper layer into a coil geometry by photolithography (photoresist AZ 4620; spin-casting at 3000 rpm for 30 s, baking on a hot plate at 110°C for 3 min, UV irradiance for 300 $\mathrm{mJ \cdot cm^{-2}}$, and development for ~40 s with developer AZ 400K/deionized water solution of 1:3 volume ratio) and wet etching (CE-100 copper etchant, Transense; ~2 min with frequent rinsing by water). Dry etching (reactive-ion etching; 20 sccm O2, 200 mTorr, 150 W, 1800 s) removed the PI everywhere except underneath the copper traces. A cellulose-based, water-soluble tape (e.g., Aquasol Corporation, ASWT-2) allowed retrieval of the structure from the PDMS/glass substrate. Deposition of a bilayer of Ti/SiO2 on the backside of the structure allowed the strong bonding to a base layer of PDMS pre-exposed to UV-induced ozone. After removing the water-soluble tape, solder joints formed between the electronic components and corresponding bond pads on the Cu/PI platform yielded functional systems. Layers of polyisobutylene (PIB) and PDMS served as encapsulation.

Fabrication of the optoelectronic stimulating component. Solder joints and epoxy electrically and mechanically bonded two μ-ILEDs (TR2227, Cree) onto a polyimide substrate with exposed traces of copper. The same strategy bonded a pair of copper wires in a polyurethane tube (PU-025, SAI infusion technologies) onto copper metal pads at the opposite end of polyimide substrate to serve as the interconnection between the μ-ILEDs and the WCP module. This component was mounted onto a stainless-steel casing with epoxy (Loctite epoxy marine) coated on the back side. A dip-coating process followed by thermal curing formed encapsulating layers of PIB (two coats) and

PDMS (three coats) on the front, bladder-facing side.

Fabrication of the strain gauge (SG) component. A thin layer of silicone elastomer (Ecoflex-30, 40 µm thickness) on a water-soluble film of poly(vinyl alcohol) served as a support for a piece of screen-printed silicone doped with carbon black (XC-72R, Fuel Cell Store) at 15% by weight (CB-S). Patterns of copper formed on the polyimide substrate, attached to the CB-S ends, provided means for electrical measurement. Silver (H20E Epo-Tek, TED PELLA) paste and epoxy (Loctite epoxy marine) mechanically and electrically secured the junctions. A spin-cast overcoat of silicone provided encapsulation. A mechanical cutting process defined the final shape of the device. Mechanical deformation of such a soft platform induced the change in resistance correlated to bladder size (Figure 5.5).

Experimental subjects. Adult (200–300 g) female Sprague Dawley rats (Taconic) housed in pairs with access to food/water ad libitum were maintained on a 12 h:12 h light:dark cycle (lights on at 6:00 AM). All procedures, unless specifically stated otherwise, were performed during the light cycle. All experimental procedures were approved by the Animal Care and Use Committee of Washington University and in strict accordance with the US National Institutes of Health (NIH) Guide for the Care and Use of Laboratory Animals.

Surgical implantation of the optoelectronic device. The optoelectronic sense/stimulate (OSS) module was implanted around the bladder with the µLEDs facing the bladder. The strain gauge first was secured around the bladder with the lower band. Kwik-Sil adhesive (WPI) was used to secure the strap to the base of the device (near the µLEDs), then the top buckle was passed through the connective tissue on the back of the bladder and connected to the other side of the T-shaped buckle. A small absorbable suture (Plain Gut 6-0, Covidien) was placed through the band and into the smooth muscle layer of the bladder, with care taken to not puncture the bladder lumen. The wires, connecting to the wireless control/power (WCP) module, were then externalized through the abdominal muscle layer, and the WCP (3 x 3 x 0.3 cm) was implanted between the skin and muscle rostral to the muscle incision. Sham surgeries followed the same protocol and timing without implantation of the device. Both wirelessly and battery powered devices were implanted and used throughout the following experiments.

Dynamic mechanical analysis. A dynamic mechanical analyzer (Q800 DMA; TA Instruments) served as a tool for determining Young's moduli through analysis of measured strain-stress curves. The measurement involved a film tension clamp, a strain rate of 1% / min, and a maximum strain of 25%, all performed under ambient conditions.

Finite element analysis of bladder expansion. FEA was performed using the commercial software ABAQUS. 3D shell elements (ABAQUS element type S4R) were used for modelling of the bladder and 3D continuous elements (ABAQUS element type C3D8R) for the strain gauge. The mechanical properties of bladder wall are described by its nominal bi-axial stress-strain relation obtained from pressure-expansion data. The moduli of the carbon-black-doped silicone and the silicone encapsulation are 270 kPa and 60 kPa, respectively. The initial length of the strain gauge is 15 mm, which guarantees its conformal contact with the bladder for the expected range of pressure differences for awake rats (3 kPa for full state and 1 kPa for empty state, referenced to air pressure), while minimizing constraints on natural motions of the bladder (Figure 5.6)

Light penetration through the bladder. To measure the light penetration, a rat bladder was removed and placed over a light sensor (Thor Labs). A syringe inserted into the neck of the bladder and secured with a suture (4-0 Silk) allowed for manual inflation with saline. The μ-ILEDs were placed on top of the bladder, directly in contact with the bladder surface. Light power recordings were made with the bladder in the fully inflated and empty states, each with and without μ-ILED illumination to account for ambient light. The bladder was then cut open and a sheet of bladder tissue was placed on the sensor for measurements of light transmission (Figure 5.7)

Thermal finite element analysis of operation of an μ-ILED. The calculations of the temperature increase with time were obtained by finite element analysis using ABAQUS commercial software (ABAQUS Analysis User's Manual 2010, V6.10). The μ-ILED device (4 × 1.1 × 0.7 mm) consists of PDMS (390 μm thick), PIB (10 μm thick), epoxy (195 μm thick), copper (8 μm thick), PI (12 μm thick) and stainless steel layer (25 μm thick) from top to bottom. The rectangular μ-ILED consists of a layer of SiC and InGaAs with length, width and thickness of 270 × 220 × 40 μm and 270 × 220 × 10 μm, respectively. The parameters used in the modeling include conductivity, density, and specific heat. The blood perfusion rate was 0.008 ml/ml/s [23]. The computed temperature increases resulted from heat uniformly distributed across the rectangular surface of the μILED, with thermal output power of 70 mW/mm2. The modeling results of temperature increment matched experimental findings. Linear hexahedral elements of type DC3D8 were used to ensure accuracy and convergence of simulation results.

Wireless communication. Experiments used both battery-free and battery-powered devices. For the latter, a 90 mAh coin cell battery and a low-dropout regulator replaced the load-coil, impedance matching circuit, and power management circuitry of the former. The remaining circuitry consisted of the microcontroller (nRF51, Nordic Semiconductor) for wireless communication and the bridge circuit to measure the resistance of the strain sensor. A microcontroller embedded with a radio-frequency transceiver and an analog-to-digital converter sampled measurements and controlled the μ-ILEDs (Figure 5.8). The resistance of the strain sensor was measured using a bridge circuit and an instrumental amplifier, converted with an internal analog/digital converter (ADC) in the microcontroller, and transmitted to a user-interfacing device every second for further signal processing. A sampling rate of 1 Hz was sufficient to capture the bladder activity (~1 hour for bladder to fill and ~30 seconds void). Further signal analysis on the iOS application classified overactive bladder activity to determine when to activate the μ-ILEDs (current-controlled at 6.2 mA using a general-purpose input/output on the microcontroller).

In-vitro testing of operational stability. Benchtop in vitro experiments characterized the stability of the encapsulation layer against water penetration. The experiments involved immersion of the full system in saline solution at 37 °C in an oven. The normalized resistance of the strain gauge, the optical output power of the μ-ILEDs and the received signal strength indication (RSSI) of the WCP were recorded. The data verified stable operation for 30 days, with no sign of water penetration (Figure 5.9).

Anesthetized cystometry. Rats were first anesthetized with urethane (U2500, Sigma), (two i.p. injections totaling 2 mg/kg, 1 hr apart; 0.8 and 1.2 mg/kg; stock solution 150 mg/ml) and then a midline incision was used to expose the bladder dome. A PE50 catheter (BB31695-PE/3, Scientific

Commodities, Inc.) was inserted into the dome of the bladder and secured with a purse string suture [24]. After the catheter was placed, if an LED strain gauge was used it was placed around the bladder as described above. The LED was then connected to a current source (U8031A, Agilent) and controlled manually. The strain gauge was connected to a digital multimeter device (USB-4065, National Instruments) and data were recorded in LabVIEW (National Instruments) with a developed script to measure changes in resistance. Then the syringe pump was started and the bladder was filled at 0.1 ml/min with room-temperature saline to evoke a regular voiding pattern. Intravesicular pressure was measured using a pressure transducer amplified by a Transbridge 4M amplifier (WPI) and recorded using WINDAQ data acquisition software (DataQ Instruments) at a sampling rate of 5 Hz. After a regular pattern was established, for experiments using the LED strain gauge, five consecutive contractions (4 intercontraction intervals) were recorded for baseline and then the LED was illuminated for the subsequent 5 contractions. This was repeated for each animal (total of 2 x). The first contraction after the light was turned on was not counted for either the baseline or LED period. For comparison of chronic strain gauge implantation vs. sham surgery and sham injection vs. viral injection, 1 hour of cystometric voiding was acquired from each animal after a stable pattern developed. Data were analyzed using a Matlab (Mathworks) script to determine baseline pressure (BP), threshold pressure (TP), maximum pressure (MP) and intercontraction interval (ICI) (terminology conformed to [25]. Compliance was calculated as (Flow rate x (TimeBP-TimeTP)) / (TP-BP). Rats that did not develop a regular cystometric pattern were excluded from analysis.

Open-loop/user controlled μLED experiments. Rats were injected with either HSV-CMV-eYFP or HSV-CMV-Arch-eYFP at day 0 and implanted with the CLOC system on day 3. On day 5 rats were acclimated in modified metabolic rat cages above computerized balances (Columbus Instruments) for at least 2x 45-60 min sessions at least 1 hour apart. On day 6 they were put in the metabolic cage or kept in home cage in the same room and the μLEDs were turned on or left off for 3 hours, depending on the treatment group. Some experiments were performed in metabolic cages to confirm voiding events to understand the relationship between SG resistance and voids (training set). On day 7 rats were injected with CYP 9 (75 mg/kg, i.p.) at the same time of day as the baseline test and put in the metabolic cage or left in the home cage. μLEDs were turned on (or not) and strain/metabolic data was recorded for 3 hours. All void analysis was done post hoc (Microsoft Excel). Voids were identified by methods outlined below.

Void identification signal analysis and verification. To identify voiding events, raw strain gauge data were analyzed using multiple-step signal processing. Standard deviation (SD) was calculated from each animal to account for device-to-device variability in noise and degree of change during filling and emptying events. The SD was taken from ~1 hour of raw data without a void. Raw data voids were identified by the following 4 steps: (1) take a moving 60-point (1 min) average, (2) down-sample to 4 points per second (from 1 pt per second), (3) calculate the derivative of the down sampled data, (4) if three consecutive derivative values are less than 3X the negative SD, this is counted as a preliminary void. There are two conditions when preliminary voids calculated in this way are rejected: when there was a void in the previous 5 min and if there was a significant positive derivative value, indicating animal movement, preceding the void. A significant positive derivative value was calculated by averaging only the positive derivative values from the previous 10 points (2.5 min). If this value was higher than 40% of the SD (with a minimum value of 7) then the preliminary void was eliminated and counted as noise.

User interface (UI) and voiding identification. Software developed using XCode and operating on a tablet computer (iPad mini 2 and iPad Air 2, Apple) served to capture and compile SG data. The iOS application (1) logs SG data for post-data analysis, (2) defines LED protocols for optogenetic activation, and (3) sets calibration parameters for closed-loop experiments. Also, the UI displays 30 min graphical plots of raw, filtered, and derivative SG data for troubleshooting. Operationally, the application first logs SG data (sampled at 1Hz) in a text file format in the iOS device after establishing Bluetooth connection to the implanted WCP device. Comparing SG data with metabolic cage data sets the foundation for the signal processing required for closed-loop function. Second, the manual LED switch and textboxes located at the top of the GUI enable open-loop optogenetic experiments. Turning on the "Manual LED" switch activates an LED protocol that follows an on/off timing pattern defined in the text boxes. Lastly, the closed-loop experimental function engages after a series of open-loop experiments. The "Automated ClosedLoop" switch turns on closed-loop functionality with calibration parameters defined in the textboxes. The parameters "Device STD," "Noise Threshold," and "Voiding Interval" are calibration metrics determined via data collected before the closed-loop experiments to account for variances among devices and rats. A series of signal processing steps determine whether a voiding has occurred (described above). If three voiding events occur within a preset interval, the LED protocol is activated.

Closed loop experiments. Rats were injected with HSV-eYFP or HSV-Arch-eYFP and implanted with the CLOC system 6 days prior to the experiment. On post-operation day 6 (POD 6) SG data was collected to calculate the SD to calculate the threshold for voiding, for each individual animal.

On the morning of POD 7 (~0800) the closed loop program was activated while the rat was in its home cage. At ~1200 the closed loop program was turned off and the animals were injected 10 with 150 mg/kg CYP. The program was turned off to prevent accidental activation due to experimenter handling the animal. Fifteen minutes after the injection of CYP, the closed loop program was turned on. Data were analyzed as described above.

5.5 Conclusion

In summary, the fully wireless, implantable bio-optoelectronics systems reported here represent a unique class of technology that allows for closed-loop modulation of peripheral organ function by combined, coordinated operation of a soft, biophysical sensor for feedback control and a proximal light source for optogenetic stimulation. The specific results illustrate that the approach of utilizing virally delivered opsins as PNS neuromodulators [26-32] can be effective in normalization of bladder dysfunction in unanesthetized, freely moving animals, and suggests scaled systems could be developed for optogenetic neuromodulation of bladder dysfunction in human patients to increase specificity and dynamic control relative to electrical stimulation. To that end, we demonstrate that Arch activation can successfully decrease excitability of human DRG neurons in a manner similar to what we show in rats. Initial clinical trials utilizing opsins are under way [33,34] but improvements in safety and efficacy of gene delivery systems are needed to fully realize the clinical potential of optogenetic neuromodulation. Furthermore, light delivery technology will need to be scaled to provide adequate illumination to the much thicker and larger volumes of tissue in the human bladder. Possible approaches to this scaling include implementation of a large number of light sources (e.g. a net of μ-LEDs covering the bladder), likely utilizing red-shifted opsins which permit better tissue penetrance [35,36], or the implantation of an LED-based device into the lumen of the bladder to provide light delivery to the sensory neuron terminals in the urothelium.

Although the current study demonstrates the utility of this approach in monitoring and modulating bladder function, the core ideas and the supporting technology platforms can be easily adapted to address a range of application possibilities beyond those associated with the bladder. For example, the OSS module can be modified to integrate multiple biophysical (temperature, flow, pressure, etc.) and/or biochemical (metabolites, proteins, hormones, etc.) sensors, and can be configured with various types of actuators (optical, electrical, pharmacological, etc.) to provide the desired modulation, all through control provided by adapted forms of the WCP module and data analytics approaches at the software level. In this sense, the platforms introduced here have versatile uses in preclinical and clinical studies into physiology and pathophysiology of the PNS. Altogether, this system and set of supporting demonstration studies provide a framework for future closed-loop technologies suitable for treatment of diseases affecting the PNS, offering alternatives to nonspecific pharmacological or electrical stimulation approaches.

5.6 Figures

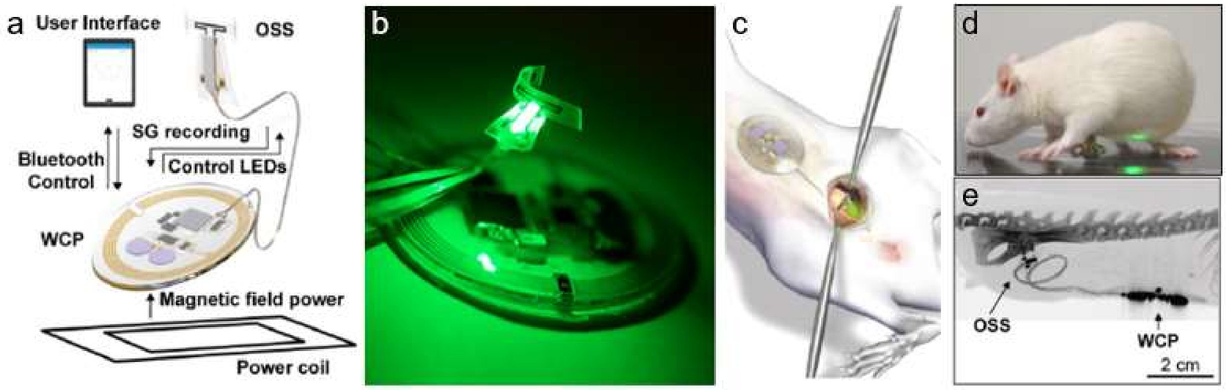

Figure 5.1. Schematic illustrations and images of a fully implantable, soft optoelectronic system for wireless, closed-loop optogenetic modulation of bladder function. a) The platform consists of the three sub-systems. The first, the optoelectronic sense/stimulate (OSS) module, is a low modulus, stretchable strain gauge (SG) with integrated microscale light-emitting diodes (μ-LEDs) in the form a thin band that wraps around the bladder to monitor changes in its volume and to provide optogenetic stimulation to the neurons innervating the bladder. The second, the wireless control/power (WCP) module, records the response of the strain gauge, controls operation of the μ-LEDs and provides power management. Wireless data communication to and from the WCP module relies on Bluetooth protocols and a tablet computer with a custom graphical user interface. The third subsystem delivers power wirelessly via resonant magnetic coupling through a dual antenna transmitter, to allow robust coverage across a targeted cage environment. b) Photograph of OSS module including the strain gauge, the μ-ILEDs and wireless base station for data communication. c) Schematic illustration that highlights the placement of the strain gauge around the bladder, with an implanted, wired connection to the WCP module subcutaneously implanted anterior to the bladder. d) Photograph of a rat with a complete system implanted, where a green μ-ILED on the WCP module serves as an indicator to verify function. e) Computed tomography (CT) image of a device implanted for 1 month.

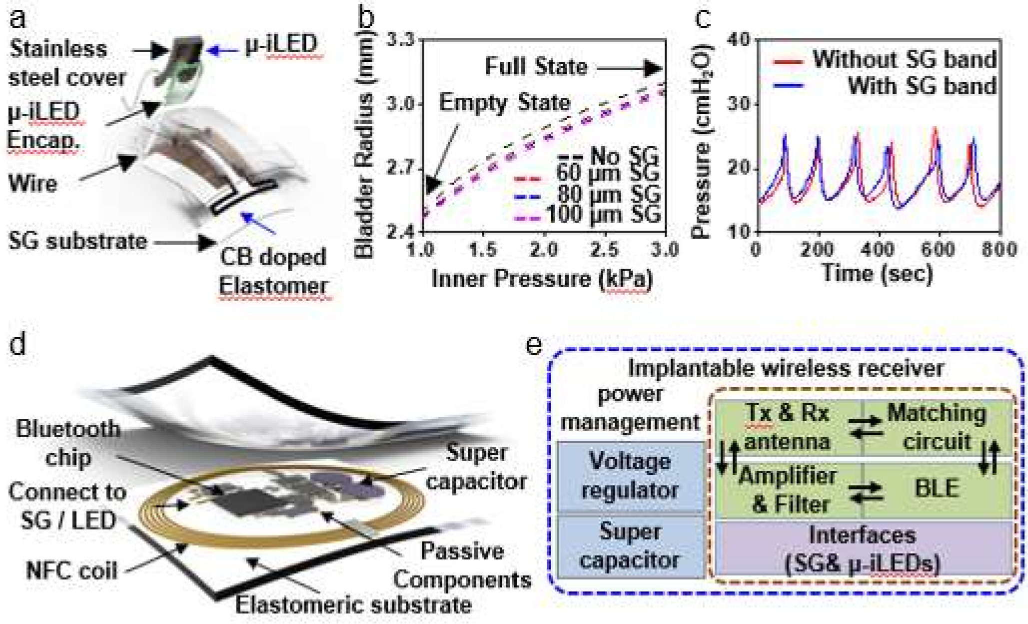

Figure 5.2. Electrical and mechanical properties of the OSS module for precise detection of micturition, targeted optogenetic stimulation of bladder sensory neurons and data communication to/from the WCP module. a) Schematic illustration of the OSS module. b) Simulated radius of a bladder during expansion with and without an integrated OSS module. c) Acute cystometry of a rat bladder before and after placement of the OSS module, demonstrating no discernable alterations to intravesical pressure due to the presence of the device. d) Schematic illustration of the implantable WCP module. e) Operational block diagram of the overall system design (Rx-receiving, Tx-transmitting).

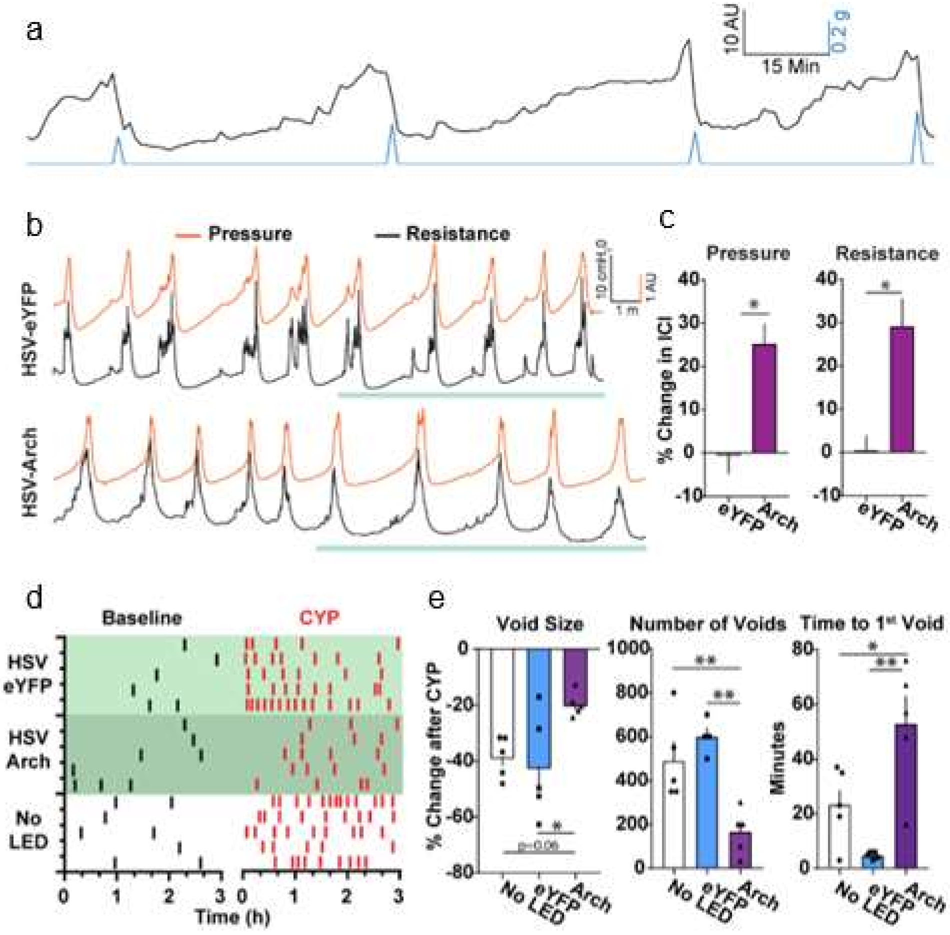

Figure 5.3. Optogenetic modulation of bladder function. a) Time dependence of strain gauge data (60 point running average) collected from a freely moving rat implanted with a CLOC system, showing rapid decreases in resistance that correlate with micturition events measured by a computerized balance in a micturition cage. Representative traces (b) and grouped data (c) that demonstrate a significant increase in cystometric intercontraction interval (ICI) during green light illumination in HSVArch injected animals compared to HSV-eYFP injected controls, as defined by the strain gauge and pressure recordings. (n=4 rats/group; *p<0.05, Mann-Whitney t-test.) d) Raster plot representing voiding of individual animals (horizontal rows) before and after CYP in HSV-eYFP LED-ON, HSV-Arch LED-ON and virus-injected LED-OFF groups before and after CYP. e) Quantification of mean number of voids 3 hours after CYP and time to 1st void after CYP injection in all groups. (n=6 rats/group; *p<0.05, **p<0.01; Two-way ANOVA with Tukey's multiple comparison test.) All error bars represent SEM.

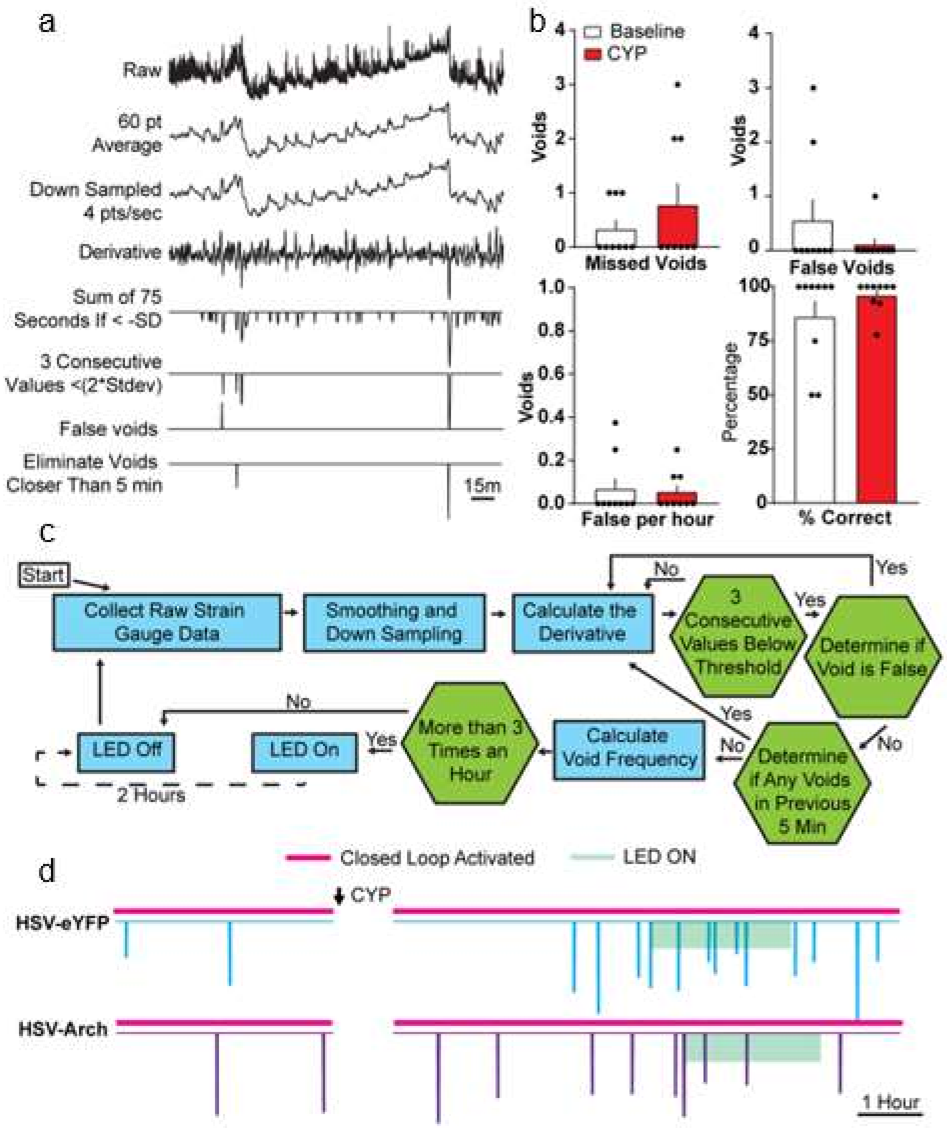

Figure 5.4. Closed-loop optogenetic control of bladder function. a) Diagram demonstrating the step-by-step process for identifying voids from raw strain gauge data. b) Quantification of the number of missed voids, false voids, false voids per hour and % correct during 8 hours of recording at baseline and 8 hours after CYP using the void detection algorithm (5 n=9 rat per group). c) Flow chart of the steps implemented in the closed-loop software to activate the μ-ILED when voiding becomes hyperactive. d) Demonstration of closed-loop μ-ILED activation, initiated at an average of 265 min post-injection after injection of CYP with corresponding decrease in voiding events in HSV-Arch-eYFP injected rats compared to HSV-eYFP control injected rats.

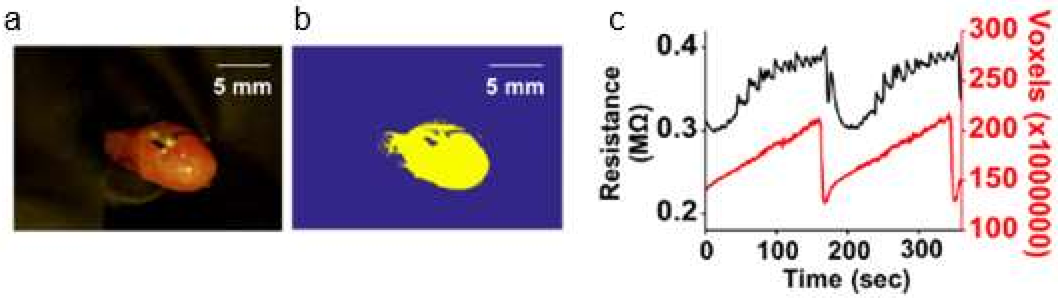

Figure 5.5. Correlation of strain gauge data with bladder deformation. a) Image of a rat bladder. b) Digitally manipulated version of a rat bladder. c) Measurement of the volumetric changes in size during cystometry.

a

Inner Pressure (mmHg)	3.2	4.6	5.8	9.2	13.1	16.5	18.4
Bladder Width (mm)	3.52	4.4	4.45	5.61	5.8	5.87	6.25
Bladder Length (mm)	5.83	6.3	6.4	7.5	7.8	8.05	8.23

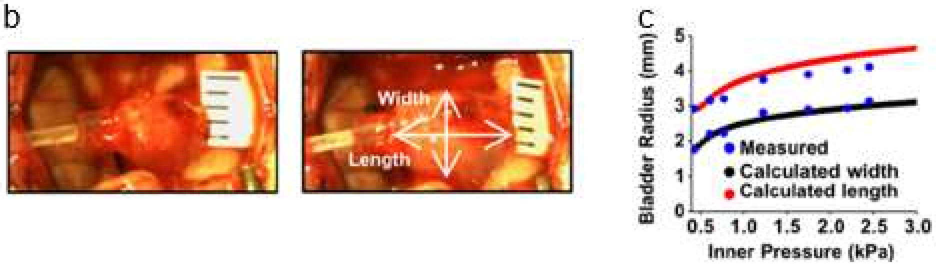

Figure 5.6. Representative bladder deformation while filling. a) Length and width of the bladder measured using Vernier caliper, at different inner pressure. b) Representative optical image of rat bladder at different inner pressure: empty (left), full (right). c) Simulation results for the width and length of the bladder based on measured value of the inner pressure and the initial length and width.

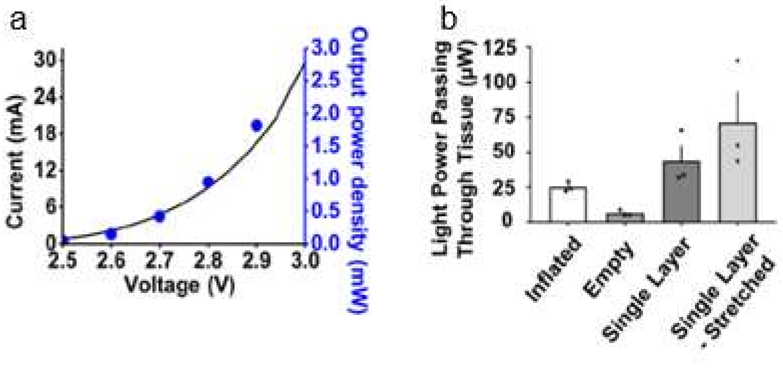

Figure 5.7. Optical characteristics of the μ-ILEDs. a) Electrical and optical characteristics of pair of μ-ILEDs. b) Measured power associated with penetration of light from a μ-ILEDs through the whole rat bladder.

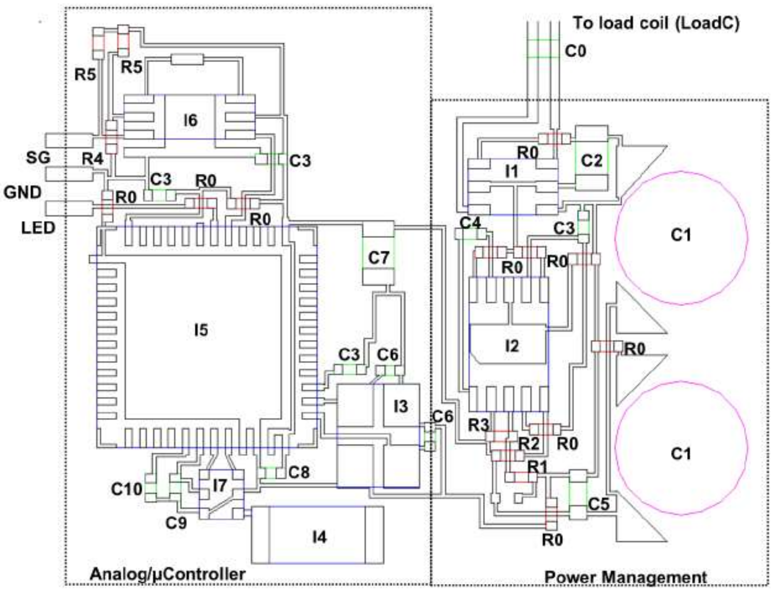

	Component	Product number
C0	86.5 pF	WCAP-CSGP 0402
C1	80 mF	XH414HG-IV01E
C2	1 µF	GRM033R71E102KA01J
C3	0.1 µF	CL03A104K03NNNC
C4	1 µF	CL03A105MP3ZSNH
C5	10 µF	CL05A106MP5NUNC
C6	12 pF	GRM0335C1E120GA01D
C7	47 µF	GRM188R60J476ME150
C8	10 pF	GRM033R71E102KA01J
C9	2.2 nF	GRM033R71A222KA01D
C10	47 nF	GRM033C80J473KE19D
R0	0 Ω	RC0603J000CS
R1	40.2 kΩ	RC0201FR-0740K2L
R2	220 kΩ	ERJ-1GEF2203C
R3	68 kΩ	ERJ-1GEF6802C
R4	22 kΩ	RC0201FR-0722KL
R5	1 MΩ	RC0201FR-071ML
I1	Schottky Diode	BAS40XY, 115
I2	DC Converter	LTC3255
I3	Crystal	CX2520DB16000D0WZRC1
I4	Antenna	2450AT18A100E
I5	Microcontroller	NRF51822
I6	Amplifier	INA333AIDGKR
I7	Balun	2450BM14E0003T

Figure 5.8. Layout and component information for the wireless control and power module.

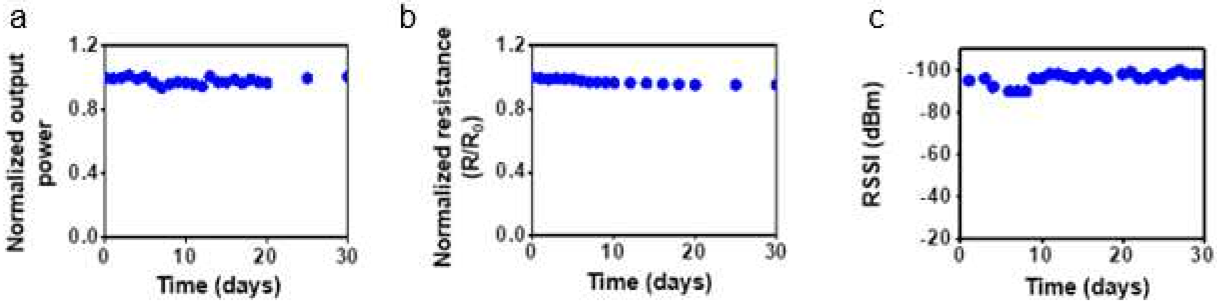

Figure 5.9. In-vitro durability test. Measurements of (a) optical output power from the LEDs, (b) resistance of the strain gauge, and (c) received signal strength (RSSI) of the wireless system operating while immersed in saline at temperature of 37 °C.

5.7 References

[1] W. C. de Groat, C. Tai, *Bioelectronic Medicine* 2015, 25 (2015).

[2] R. A. Willemze etal., *Nat. Rev*. 12, 353 (2015).

[3] C. H. Malbert et al., *Diabetes* 66, 848 (2017).

[4] G. M. De Ferrari et al., *Eur. Heart J.* 32, 847 (2011).

[5] A. R. Murray et al., *Auton. Neuro. Sci. Basic* 199, 48 (2016).

[6] T. Cameron J. *Neurosurg*. 100, 254 (2004).

[7] K. Birmingham et al., *Dug Discovery* 13, 399 (2014).

[8] K. Famm et al., *Nat*. 496, 159 (2013).

[9] X. Yu et al., *Adv. Mate*r, e1707624 (2018).

[10] S. K. Kang et al., *Accounts Chem. Res*. 51, 988 (2018).

[11] R. A. Janknegt et al., *Eur. Urology* 39, 101 (2001).

[12] S. W. Siegel et al., *Urology* 56, 87 (2000).

[13] T. Kavvadias et al., *Arch. Gynecol. Obstet*. 295, 951 (2017).

[14] K. Yoshida et al., *Proceeding of the IEEE* 98, 432 (2010).

[15] P. M. Rossini et al., Clin. *Neurophysiol.* 121, 777 (2010).

[16] J. del Valle, X. Navarro, *International Review of Neurobiology* 109, 63 (2013).

[17] H. Thabit et al., *The New England Journal of Medicine* 373, 2129 (2015).

[18] G. H. Bardy et al., *The New England Journal of Medicine* 352, 225 (2005).

[19] R. Miftahof, H. G. Nam, *Biomechanics of the Human Urinary Bladder*. (Springer, Heidelberg: New York, 2013).

[20] J. Mattis, K. M. Tye et al., *Nat. Methods* 9, 159 (2011).

[21] L. Zerboni et al., J. *Virology* 87, 2791 (2013).

[22] J. J. Deberry et al., *Front. Integr. Nuerosci.* 12, 5 (2018).

[23] J. Liu et al., *J. Biomech. Eng.* 122, 372 (2000).

[24] P. Uvin et al., *J. Vis. Exp.* 66, e3869 (2012).

[25] K. E. Andersson et al., *Neurourol. Urodyn.* 30, 636 (2011).

[26] H. Beaudry et al., *Pain* 158, 2329 (2017).

[27] M. D. Boada et al., *Pain* 155, 2646 (2014).

[28] S. M. Iyer et al., *Nat. Biotechnol*. 32, 274 (2014).

[29] S. M. Iyer et al., *Sci. Reports* 6, 30570 (2016).

[30] B. Li et al., *Brain Research* 1609, 12 (2015).

[31] K. L. Montgomery et al., *Nat. Methods* 12, 969 (2015).

[32] C. Towne, *Plos One* 8, e72691 (2013).

[33] ClinicalTrials.Gov, RST-001 Phase I/II Trial for Advanced Retinitis Pigmentosa. https://ClinicalTrials.gov/show/NCT02556736, (2018).

[34] ClinicalTrials.Gov, Dose-escalation Study to Evaluate the Safety and Tolerability of GS030 in Subjects with Retinitis Pigmentosa. https://ClinicalTrials.gov/show/NCT03326336, (2018).

[35] A. S. Chuong et al., *Nat. Neuroscience* 17, 1123 (2014).

[36] J. Y. Lin et al., *Nature Neuroscience* 16, 1499 (2013).

Chapter 6. Chronically Functional, High-Density (Kilopixel) Neural Interface

6.1 Summary

Long-lived, ultrathin, high-resolution, neural interfaces are essential for precise brain mapping. Specifically, ultrathin and flexible devices are capable of maintaining signal quality over long periods of time with dramatically lower tissue injury and irritation after implantation. In addition, higher density sampling of neural activity reveals rich spatial and temporal information that is hidden in other traditional electrophysiological techniques, such as EEG and ECoG. Achieving both high density and high flexibility while sampling from large area of the brain requires tight integration with actively powered electronics. However, all actively powered electrode arrays using existing polymer-based encapsulation strategies are unable to function long-term in the body without failure. This chapter presents actively powered electrode arrays that can record stable and long-term (over a year) neural signals from rat and nonhuman primate neocortex. This work demonstrates the feasibility of using a thermally grown, ultrathin layer of silicon dioxide ($tSiO_2$) to act as the dielectric medium for capacitive sensing of neural signals and as the biofluid barrier with a projected lifespan between 6 and 60 years. This device design and encapsulation strategy can be generalized to all neural electrode arrays enabling high-density and high-channel count interface between the brain and electronic systems.

6.2 Introduction

Neural interfaces are widely used for chronic disease management, sensory restoration, and motor rehabilitation. Recordings from these devices have provided great insight in studying basic neural processes underlying human behavior and causes of neurological disorders. Among these interfaces, penetrating electrodes have yielded important insight into neural correlates of behavior, and have been the gold standard in electrophysiology due to their ability to isolate signals from individual neurons. However, implantation damage, tissue inflammatory response, and corrosion of the electrodes remain major issues limiting the long-term stability of these penetrating implants.

These limitations have motivated the use of electrocorticography (ECoG) interfaces, which record from the cortical surface without damaging brain tissue. Centimeter-scale (macro) size and spacing devices used clinically have demonstrated long-term recording and stimulation stability in advanced therapies, such as long-term ECoG implants in humans for seizure monitoring (up to seven years [1]), and responsive cortical stimulation for seizure arrest (more than two years [2, 3]). In research applications, submillimeter-scale (micro) size and spacing interfaces revealed additional biomarkers that could be used to improve outcomes for seizure diagnostics. Microscale electrode arrays can better detect high-frequency oscillations [4-6], and micro-seizures [7-9] which are either not observed on existing macro-electrodes or poorly sampled. Furthermore, the combination of high-resolution microelectrodes with large area coverage has revealed directional spatiotemporal patterns during epileptic seizures that were previously undetected using traditional macro-ECoG electrodes.

The grand challenge for neural interfaces is the ability to acquire reliable microscale neural signals simultaneously over large areas of the brain. Scaling neural interfaces to have thousands or millions of sensors requires direct integration with electronics, i.e. active electrode arrays. Integrating electronics directly into the sensor eliminates the wiring bottleneck and enables highly scalable electrode arrays. However, until now, active electrode arrays could not be implanted in the brain long-term due to encapsulation failure. Active electrode arrays include metal lines that are continuously powered, creating a voltage differential between these metal lines and the brain which accelerates the failure of any polymer-based encapsulation. Further, a single pin-hole defect in the encapsulation will cause an active electrode to fail by introducing a leak current into the brain. For the purpose of chronic stable operation, a daunting challenge is to find a material strategy for flexible, robust thin-film encapsulation that can serve both as a large-scale biofluid barrier and as a long-term neural interface.

This chapter reports a flexible, actively powered electrode array that can chronically and stably function in both rat and non-human primate neocortex. To evaluate the performance of capacitive sensing and the long-term stability of the active array, we developed a rodent array with similar size and density as the previously published microscale passive Faradaic electrode array [10]. To demonstrate the scalability of the active array, we also developed a larger 1008-channel active array for use in nonhuman primates (NHP). Our approach demonstrates, for the first time, a long-term implantable active neural sensor using flexible electronics that are scalable in coverage, channel-count and resolution. Neural recordings were stable over a year of implantation in rats and showed stability similar to that of gold-contact, Faradaic passive electrodes. The device design and encapsulation strategy can be generalized to all other neural electrode arrays for high-density and high-channel-count neural interfaces. Significant components of this chapter will be submitted for publication as K. Chiang, S. M. Won et al., “Long-lived, ultra-thin, high-resolution, neural interfaces.”

6.3 Results and Discussion

The overall system exploits recent advances in the flexible, capacitively coupled array, in which thermally grown silicon dioxide (t-SiO2) serves not only as the biofluid barrier (t-SiO2 on front and back side), but also as the dielectric for the capacitive coupling (t-SiO2 on front side) between adjacent tissues and silicon nanomembrane transistors. Two layers of metal interconnects and embedded multiplexers enable recording from 1008 electrodes (28 columns and 36 rows), each with the dimensions of 250 μm x 330 μm, covered uniformly over the area of 9 x 9.24 mm^2 (Figure 6.1a). Within each unit cell, a constant current sink external to the array and a transistor with capacitively coupled input (T2 in Figure 6.1b) form a source-follow amplifier configuration. Here, a positive DC potential set by a remote acquisition system and an additional AC potential from the output of the source follower in a drain of the transistor enable active shielding (AS) that reduces the effect of the parasitic drain-gate capacitances, improving the overall gain of the circuit. Another transistor (T1 in Figure 6.1b) in the unit cell multiplexes the electrical signal from the tissue in a rapid time sequence manner. Consequently, the total number of wires needed is 2 * C + R, where C is the number of columns and R is the number of rows in the array. This number of wires can be further reduced by increasing the multiplexing ratio and/or integrating the active shielding circuitry into the flexible array with additional transistors. *In vitro* soaking testing in a phosphate buffered solution reveals very high yield (99.8%) and uniform voltage gain (0.88, where 1 is the ideal value) throughout the 1008-ch array (Figure 6.1c). Figure 6.2 shows the transfer curves for a representative transistor in each unit cell.

The flexibility and corresponding mechanical fatigue property are important to study due to the brittle nature of t-SiO2 that covers the entire system. The overall array thickness is only 29 μm in the sensing area (Figure 6.3a), resulting in minimal induced strains on each layer during the bending (Figure 6.3b). The finite element analysis (FEA) indicates that the maximum strains induced in key layers (i.e. Si, tSiO2, and metal layers) for 2.5 mm bending radii are less than 0.2 %, below the fracture limit (~1%) (Figure 6.3c). Repeated mechanical cycling of fatigue test to a minimum bending radius of 2.5 mm shows no change in yield or increase in leakage current up to 10,000 cycles.

For the assessment of capacitive sensing performance, an actively multiplexed electrode array with capacitive sensing electrode is fabricated in a form factor comparable to previously published passive electrode arrays [10-12] (Figure 6.4a). The electrode array includes 64 channels, arranged in an 8 × 8 grid, with an electrode pitch of 400 μm. In an acute experiment, we epidurally implanted the active electrode over rat auditory cortex, sampling electrical activity from a ~3.2 × 3.2 mm^2 area of the brain. This size and density of the active electrode are designed to be the same as the passive designs [10] to allow for direct comparison of the acquired signals. Field potentials are recorded from an anesthetized rat during (1) pseudo-randomized presentation of tone pips ranging from 0.5-32 kHz, and (2) brief, 0.2 ms in duration, broadband click sound stimuli. A three second example of a single channel in the array, filtered 2-100Hz, shows clear evoked responses generated by click sounds (Figure 6.4b).

To investigate whether each electrode in the actively multiplexed array provides an independent measurement of electrical activity in the brain, we calculate the spatial semivariogram. Spatial semivariogram analysis measures the dissimilarity of signals as a function of distance, and indicated a spatially varying random field with covariance properties that are well described by the Matérn covariance model. The length scale (2.49 mm), smoothness (0.73), and amplitude of the variance model are consistent with rat auditory cortex potentials previously observed with passive arrays [10], while the notable vertical shift in semivariance reflects the higher noise in the active device (Figure 6.4c).

The spatial specificity suggested by the semivariogram is also evident in the spatially organized tone preference of sites. An example of mean and single-trial responses for the best-tuned frequency at two sites on the array is shown in Figure 6.4d. These two sites are located 1.44 mm apart and respond most strongly to pure-tone stimuli of different frequencies (location marked in Figure 6.4e). The best-tuned frequency at each site is determined by mapping each tuning curve's center of mass at each electrode site using the Mahalanobis distance of tone-responses from the mean and covariance of baseline vectors. The best frequency tonotopic map of the array recapitulates the expected tonotopy of primary auditory cortex (Figure 6.4e) [10-12].

To demonstrate the long-term reliability of the active electrode, we implanted devices chronically in five freely behaving adult Sprague Dawley rats. The longevity of a long-term implant typically depends on the speed of biofluid ingress. For an implantable system with integrated active electronics, biofluid penetration not only damages the recording capability of the device, but also may induce unsafe leakage currents that can damage the brain. We have designed our data acquisition system to continuously monitor for leakage current throughout all recording sessions. Leakage current in all implants protected by $tSiO_2$, except one, remained at the noise floor of the recording system and well below our safety threshold of 1 μA for more than a year (Figure 6.5a). During this chronic experiment, recordings were collected at intervals of 1-2 weeks over the implantation period, mean duration of 287 days (min 63, max 435). Only a single device was terminated early due to observing leakage current. Later analyses suggested that the leakage current could have been due to dirt in the implant connector. The endpoints of the remaining four implants are caused by sudden and irreparable loss of the headcap structure. When it is possible to retrieve the electrode, we used focused ion beam (FIB) etching and scanning electron microscope (SEM) imaging to measure the remaining thickness of the $tSiO_2$ encapsulation. The average in-vivo dissolution rate was 0.46 nm/day, projecting a lifespan of ~6 years. Neural signals were successfully recorded through the $tSiO_2$ encapsulation for implant durations over one year. We recorded both tone and click-evoked responses during each recording session. In click-evoked responses, the median evoked-signal-to-noise ratios (ESNR) levels were low (0.46 dB mean), but remained above parity of 0 dB each week over the course of a year (Figure 6.5b).

The frequencies of auditory tones were predicted using the same linear classification scheme as used in the acute experiment. Single-trial tone decoding error remained above chance level in all animals, throughout the duration of the implants (Figure 6.5c). Examples of spatial semivariograms observed at multiple points of two implants are shown in Figure 6.5d to demonstrate that noise power (the vertical offset of the semivariogram) and local field potential power (indicated by the height of the semivariance curve) remained consistent.

To demonstrate scalability of the active electrodes, we fabricated and implanted ECoG arrays with 1008 contacts spanning a 9 x 9.24 mm^2 sensing area. The array was implanted semi-chronically over sensorimotor cortices using an artificial-dura-based ECoG implant. Arrays were embedded into an artificial dura, which was then implanted into a recording chamber. The electrode interconnection cables exiting the array in the artificial dura were bent at ~90 degrees with bending radius of < 2 mm. In order to enhance the robustness of such area, a protection layer of 12.5 μm of polyimide (PI) was added to the top surface of the cable. Here, the PI shifts the neutral mechanical plane closer to the front t-SiO2 barrier, reducing induced strain there (Figure 6.6). Consequently, the molded array retains its functionality and performance without any degradation. The implantation of the system covered premotor, primary motor, and primary sensory cortices. We recorded from the electrode while the animal performed a delayed-reach task to 7 peripheral targets arranged in a center-out configuration. Broadband signals showed movement-related activity, with motor evoked-potential responses across the array (Figure 6.7a). Motor evoked potentials also showed clear spatial organization across the array and varied with the direction of arm movement (Figure 6.7b). We further examined movement-related signals through spectral-domain analysis. We found low-frequency motor-related potentials in the 3 Hz band with direction tuning (Figure 6.7c and d). The degree of tuning varied across both time and contacts within the array. To further examine spatial organization of direction tuning, we fit a cosine tuning model to each electrode across different times within the trial. Prior to movement (Figure 6.7e), tuning was strongest in a focal region in premotor cortex. During movement (Figure 6.7f), the foci of tuning shift towards the primary motor cortex. Together, these results show our array was able to resolve spatiotemporal evolution of cortical processing across the sensorimotor cortices.

6.4 Methods

Device fabrication. The fabrication procedures build on concepts demonstrated for capacitively coupled, flexible silicon electronic systems, in which a thin layer of thermally grown layer of SiO_2 (t-SiO_2; derived from buried oxide layer of silicon on insulator (SOI, Si(260nm)/SiO_2(1000 nm)/Si; SOITEC) wafer) serves as a biofluid barrier and a capacitive measurement interface. The process began with mechanical grinding of the silicon substrate of the SOI to a thickness of 200 μm (Syagrus Systems). Dry thermal oxidation formed a SiO_2 hard mask to define the source/drain regions of the transistors via a high-temperature phosphorous doping process (1000 °C for 7 minutes). Photolithography (AZ 5214E) and dry etching (50 mtorr pressure, 40 sccm SF_6, and

100W RF power for 1 min) isolated the transistor areas, and dry thermal oxidation (1150 °C for 16 min) and atomic layer deposition of 14 nm Al_2O_3 formed the gate dielectric. Next, photolithography and wet etching (buffered oxide etchant) defined openings for source and drain contacts. Electron beam evaporation formed metal bilayers for interconnects (Cr/Au, 5nm/200nm). Spin-coating, soft-baking and hard curing created an overcoat and interlayer dielectric of polyimide (PI 2545, HD MicroSystems). Finally, electron-beam evaporation produced a bilayer of Ti/SiO_2 (5 nm/ 50 nm) to facilitate bonding to a PI sheet (12.5 µm, Kapton, Dupont) with layer of t-SiO_2 (thickness of 1 µm) on its back side. The bonding process, as described in detail elsewhere[4] involved UV-ozone treated PDMS as an adhesive. Inductively coupled plasma RIE (ICP-RIE) removed the Si substrate to expose the pristine surface of the SiO_2 as the biointerface.

Capacitive sensing. Each unit cell had two n-channel MOSFETs as key active components. The source follower provided the amplification on the voltage reading that we collected capacitively from sensing electrode, and the multiplexer eliminated the need for metal wires going to every single unit cell of the system. The large area of the sensing electrode provided capacitance roughly three times the gate capacitance of the transistor. The areas of sensing electrodes are 100 × 180 µm and 195 × 270 µm for devices used in NHP and rat model, respectively. The thin-film capacitance equation is

$$C = \varepsilon_r \varepsilon_0 \mathrm{A/t} \tag{6.1}$$

where ε_r is the relative permittivity, ε_0 is the vacuum permittivity, A is the area and t is the thickness of the dielectric. From this we get

$$\mathrm{C}_{Sensing\ NHP} = 3.3\mathrm{C}_{gate\ NHP} \tag{6.2}$$

and

$$C_{Sensing\ rat} = 4.9C_{gate\ rat} \tag{6.3}$$

The total capacitances driving the channel in the sensing transistors for NHP and rat model were then $0.77C_{gate\ NHP}$ and $0.83C_{gate\ rat}$, respectively, from combining sensing and gate capacitance in series. This high capacitance value ensured high transconductance, and consequently high gain and low-output impedance from the sensing transistor.

Mechanical analysis. The strain distribution in the neural sensing array under pure bending was obtained by finite element analysis (FEA). The device was pressed conformally onto a rigid cylinder with well-defined radius. Three-dimensional solid elements (C3D8R in ABAQUS finite element software) were used for thicker layers including the Kapton layer, PDMS layer, PI layer and top thermal silicon oxide layer, while shell elements (S4R) were used for thin Au layers. For 2.5 mm bending radius, the maximum strain is ~0.2% in the top thermal oxide layer, 0.17% in the 1st metal layer, and 0.1% in the 2nd metal layer.

Electrode screening. All electrodes used in the animal experiment were screened based on *in vitro* recordings in saline with respect to yield, gain, and correlation. To evaluate gain, the array was tested in saline with an input of sinewave at 10 Hz. Devices with a gain of 0.6 or above were considered good. To ensure the array was fully functional without short circuits, we recorded device noise levels from the array in grounded saline. Since the device noise should be random and uncorrelated, a correlation analysis revealed shorted or nonfunctional channels with excessive correlation. Devices that failed this test were not used. As a final screen, we examined the two-dimensional spatial autocorrelation function of the array signal. The spatial autocorrelation of normally functioning arrays was seen to be a nearly isotropic decreasing function of distance.

Excessive correlation among columns of the array manifested as a decreasing function of distance horizontally (across columns) but nearly constant vertically (within columns), indicating one or more multiplexers with poor switching.

Awake recording (Rat). All chronically implanted rats were recorded while freely behaving. All recording sessions were carried out in a sound-attenuated chamber. Equipment and experiment stimuli were the same as described in the Rat Acute Experiment. The first recording sessions were made 7-days post-surgery. Each rat was recorded every 1-2 weeks. Leakage current was continuously monitored during all recordings to ensure safety.

In vivo recording (NHP). Prior to recordings, the animal was trained to perform a delayed center-out reach task on a touch screen. The task requires the animal to touch an initial central target for a short baseline interval (400-600 ms), after which one of seven possible peripheral targets appears on the screen (circular arrangement with 45° spacing, excluding the bottom-most target). After an instructed delay (250 – 750 ms), the central target disappears, cuing the animal to reach to the peripheral visual target. Successfully acquiring the peripheral target results in a liquid reward. Target directions were presented in a pseudo-random order with balanced distributions of successful target acquisitions to all targets. We define reach onset as the time at which the animal lifts its hand off the screen to begin moving to the peripheral target.

We recorded neural activity from the 1008-contact electrode array while the animal performed the delayed center-out reaching task. The array was semichronically implanted into the recording chamber by replacing the artificial dura with one with an embedded ECoG array prior to the recordings. Data presented is from one behavioral session with 412 successful reach trials.

6.5 Conclusion

The results presented here demonstrate a promising route towards safe, robust and high-performance flexible electronics for large-scale and high-resolution recordings in both clinical and research settings. High-resolution neural interfaces will be increasingly important to the next generation of neural diagnostic, therapeutic, and prosthetic devices, given recent discoveries that link neural oscillations to traveling waves [13]. These traveling waves reveal propagating wave patterns that are more difficult or impossible to fully resolve with traditional macro-electrode recordings.

The optimal spatial sampling density for low-frequency neural signals (i.e. local field potential, LFP) is currently unknown. However, active devices can sample large areas of the brain at very high density and resolve multi-unit activity from the surface of the brain. Further, spatial oversampling of the lower frequency LFP may enable additional noise reduction techniques to mitigate the additional aliased noise introduced by multiplexing at the electrode before low-pass filtering. Future devices leveraging commercial CMOS manufacturing will also help to dramatically reduce noise in the device by incorporating higher quality transistors and local amplification. In addition, the use of the mature commercial CMOS technologies could enable neural interface systems to scale to contain millions of electrodes, well beyond what is possible using current passive electrodes that are individually wired to remote electronics. Although recording from millions of electrodes will present new challenges in data transfer, storage and processing, tight integration with CMOS circuitry on the same substrate will enable on-board signal processing and data reduction techniques. Future circuit designs can also incorporate electrical stimulation capabilities for therapeutic and prosthetic applications.

Amplification, digitization and wireless data and power transmission could also be incorporated directly into the active array, creating an implantable device where the integrated circuit is the entire system. This approach would dramatically reduce the volume and invasiveness of implantable devices and lead to new implantable systems with improved capabilities from current technology.

6.6 Figures

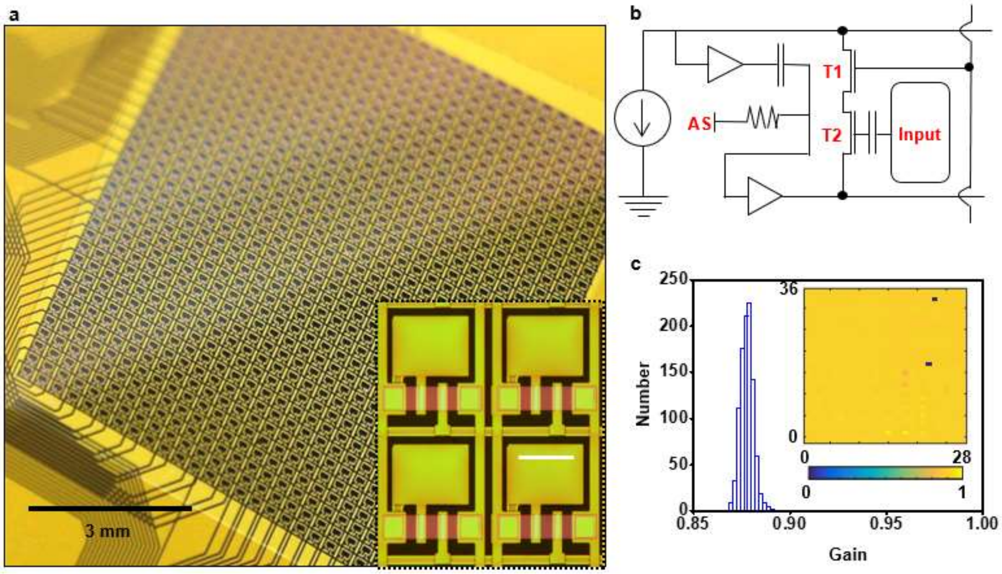

Figure 6.1. **Flexible, actively multiplexed electrode array for high-resolution and long-term micro-electrocorticography (µECoG).** a) Photograph of 1,008-ch actively multiplexed, capacitive electrode array. Inset: Each electrode is connected to a unit cell consisting of two flexible silicon transistors. Scale bar is 200 µm. b) Schematic circuit diagram of a single unit cell with two matched transistors for local signal amplification and multiplexing. Denoted AS is programmed active shield bias. c) Histogram summary of gain values determined from all 1,008 sensors of a representative device. The inset shows the spatial distribution of the gain.

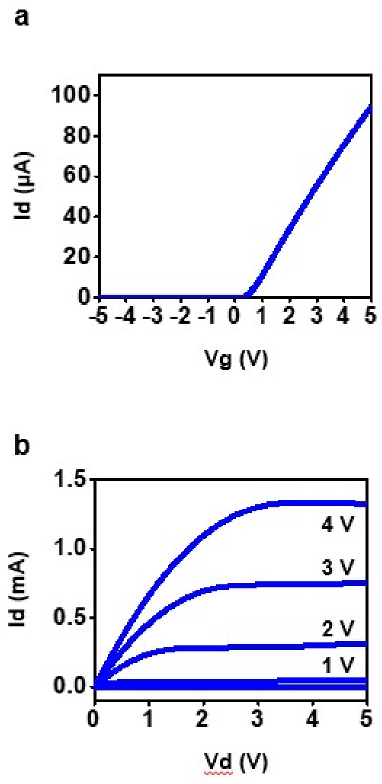

Figure 6.2. **Transistor characteristics.** a) Linear scale transfer curves for a representative transistor as gate voltage is swept from -5 to + 5 V while fixing drain voltage at 0.1 V. b) Output curve plotted as a function of drain voltage with varying gate voltage from 0 to 4 V in 1 V steps.

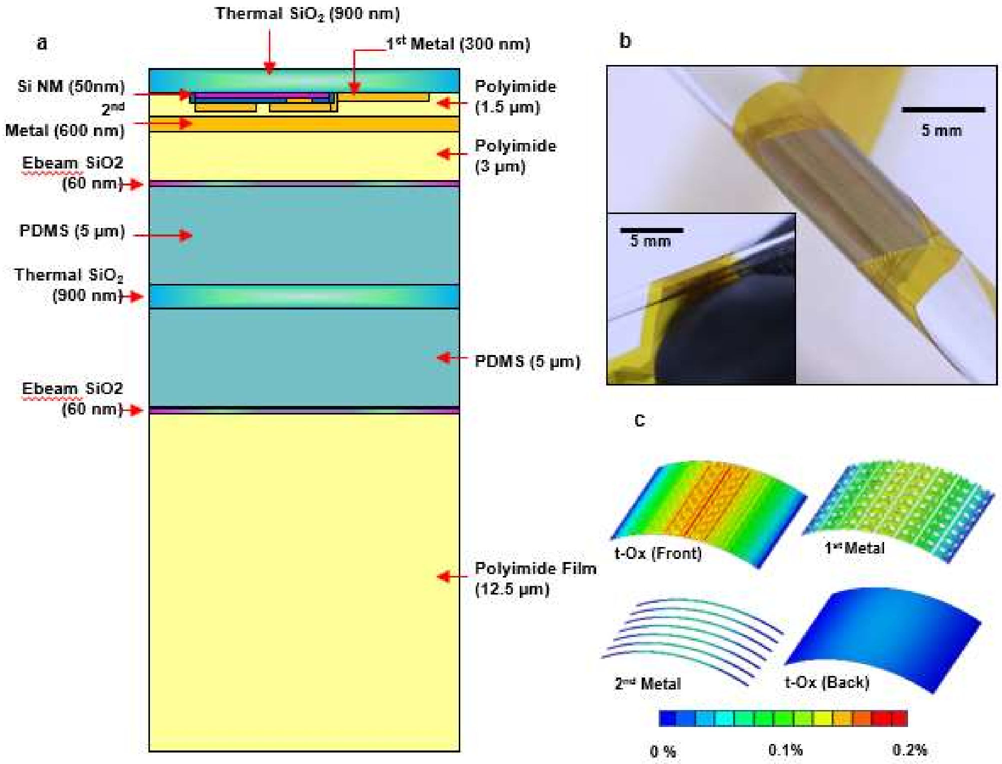

Figure 6.3. **Mechanical property of electrode array.** a) Schematic illustration to show the thickness of various layers in the device. b) Image of electrode array bent around cylindrical tubes with radii of 2.5 mm (main) and 1.25 mm (inset). c) Computed distribution of bending induced strains (radius of curvature 2.5 mm) in four different layers of the system shows strains well below the fracture limit of each material. The four layers are the SiO_2 biointerface layer, the first and second metal interconnect layers, and the backside encapsulating SiO_2 layer.

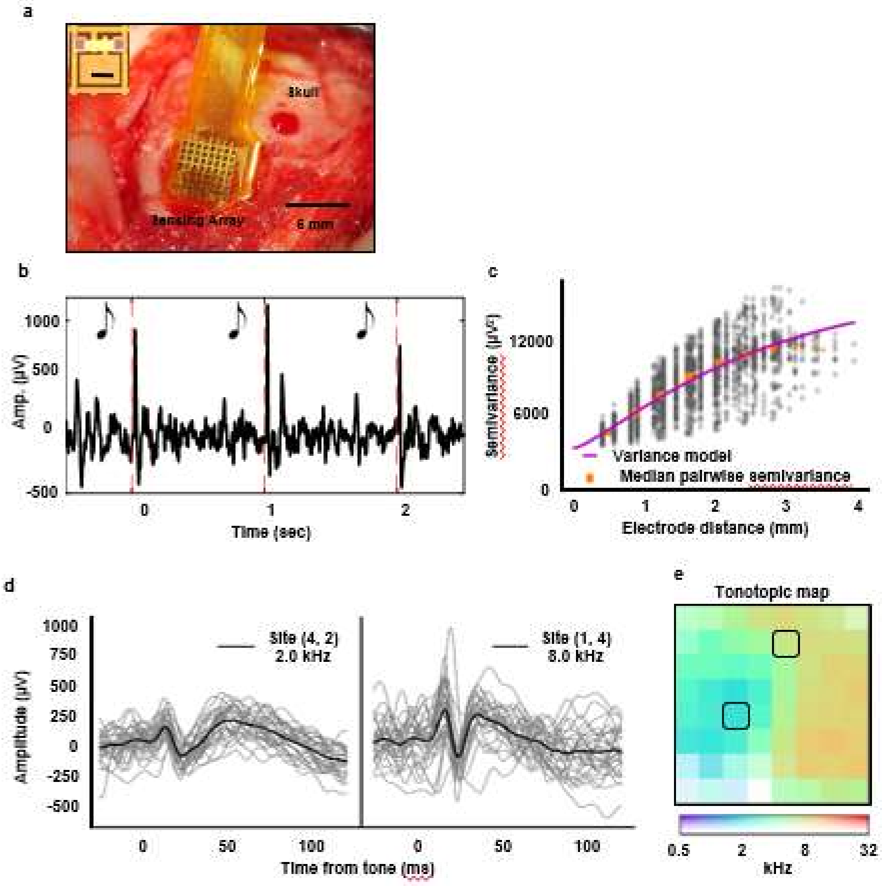

Figure 6.4. **Rat acute experiment demonstrating the capacitive sensing scheme.** a) The array was acutely implanted epidurally over rat auditory cortex. Field potentials were recorded during a pseudo-randomized presentation of tone pips ranging 0.5-32 kHz. Inset: Photograph of a single cell. Scale bar is 150 µm. b) Evoked responses with >500 µV amplitude were visible in the ongoing voltage recorded on one channel during click sound presentations. c) Spatial semivariogram analysis measured the dissimilarity of signals as a function of distance, and indicated a spatially varying random field that was consistent with rat auditory cortex potentials previously observed with passive arrays [10]. The vertical shift in semivariance reflects the higher noise in the active device. d) Mean and single-trial tone-evoked responses are shown for the best-tuned frequency at two sites on the array separated by 1.44 mm. The selected sites are boxed in panel (e). e) Mapping each tuning curve's center of mass recapitulated the expected tonotopy of primary auditory cortex.

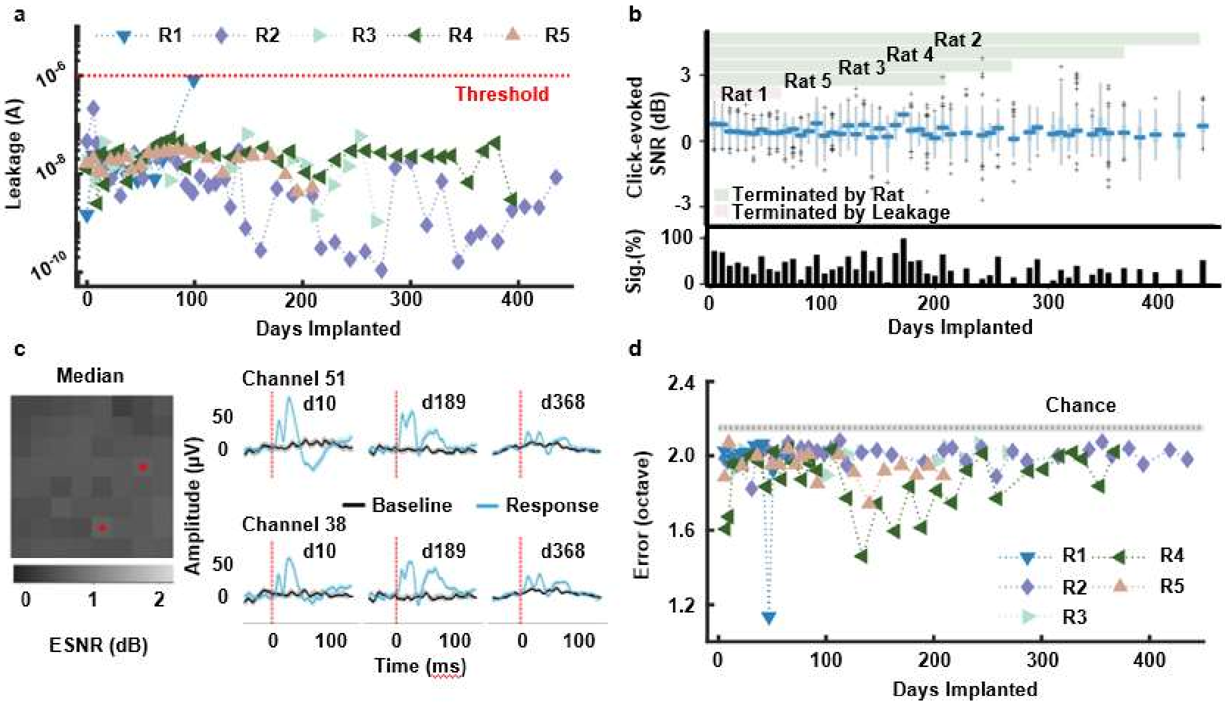

Figure 6.5. **Long-term implants of active electrodes.** a) Leakage current was continuously measured throughout all recording sessions and remained below our cutoff of 1 µA in all implants except rat 1. b) Example click responses (blue) and baseline potentials (black) recorded from Rat4 (R4) at three points in the implantation history show average evoked responses that remained distinct from the average baseline exceeding one year of implant duration. The median ESNR across recording sessions is mapped per electrode, revealing fairly homogeneous response sensitivity. c) Click-evoked responses were measured during each recording session. Recordings from each animal and week were binned together and are shown in box plots. Median evoked signal-to-noise ratios (ESNR) were low (0.46 dB mean), but remained above parity of 0 dB each week. The bar plot at the bottom shows the percentage of channels in each week with significant ESNR, measured with a response-baseline permutation procedure. In aggregate, electrodes were significantly responsive 42.7% of the time (2983 of 6993 electrode-sessions). d) Single-trial tone decoding error was measured, in octaves, in each recording session. Decoding remained above chance level (2.15 octaves) in all animals throughout the duration of the implants.

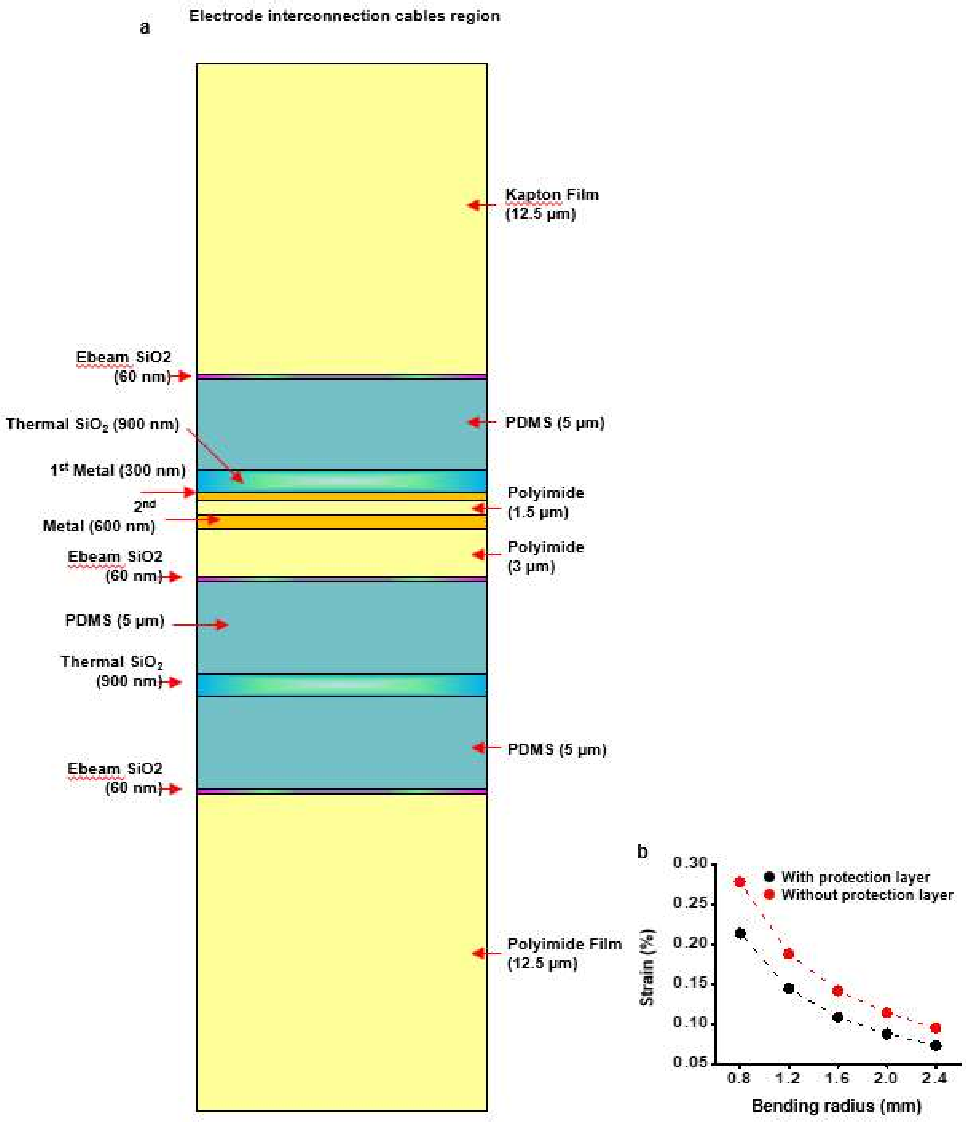

Figure 6.6. **Mechanical property of electrode array in arm (interconnection region).** a) Schematic illustration to show the thickness of various layers. b) The addition of a polyimide protection layer in the interconnection cable area of the device reduced the maximum strain in the top SiO_2 layer at all bending radii.

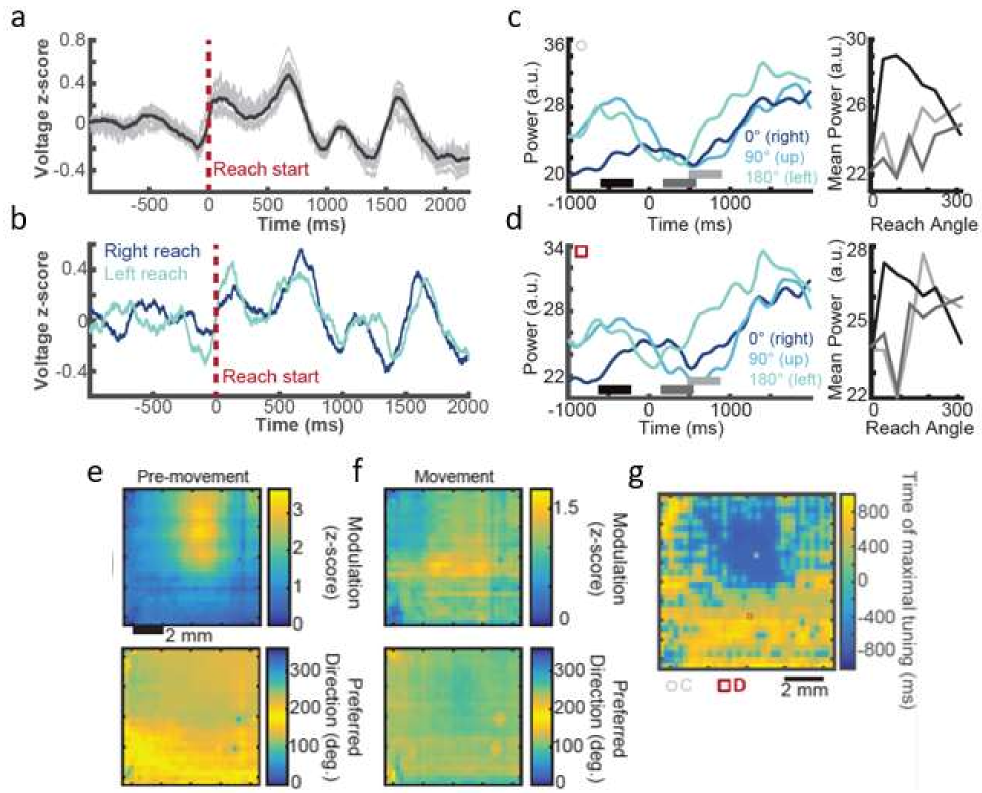

Figure 6.7. **Scalability of recordings to multibrain area recordings in nonhuman primates.** a) Evoked movement potentials (broadband), triggered at the time of movement onset, computed across all reach trials. Black trace shows the mean across all 1008 electrodes; grey traces show examples for 10 randomly selected electrodes. b) Evoked movement potentials as in (a), now separated by movement directions. Traces represent the mean across all 1008 electrodes. Two of the seven movement directions are shown (dark blue, rightward reach; light blue, leftward reach). c) Direction tuning in the 3 Hz band for an example electrode. Average power across trials, separated by reach direction, for three example directions (right); and mean power in 3 different time windows as a function of reach direction. Black trace corresponds to the pre-movement period ([-600ms -200ms]); dark grey trace corresponds to the early movement period ([200ms 600ms]); light grey corresponds to the late movement period ([500ms 900ms]). This electrode shows clear pre-movement tuning. d) As in (c) for another example electrode. This electrode shows modest pre-movement tuning and larger tuning emerging during movement. e) Spatial map of cosine tuning parameters across the electrode array for the pre-movement period ([-600 -200ms]). Modulation depth (top) and preferred direction (bottom) show focal tuning centered around the arm area of premotor cortices. f) As in (e) but for the early motor period ([200 600] ms). Tuning during movement is largest around the primary motor cortex. g) Spatial map of the time window when directional tuning was largest for each electrode reveals a clear temporal evolution of directional information starting in premotor areas that then shifts to primary motor and then sensory cortices. Locations of example electrodes from (c) and (d) are indicated by the grey circle and red square, respectively.

6.7 References

[1] M. J. Cook et al., *Lancet Neural.* 12, 563 (2013).

[2] C. T. Anderson et al., *J. Clin. Neurophysiol.* 32, 406 (2015).

[3] C. N. Heck et al., *Epilepsia* (2014). Doi: 10.1111/epi/12534.

[4] G. A. Worrell et al., *Brain* 131, 928 (2008).

[5] M. Le Van Quyen et al., *J. Neurosci.* 30, 7770 (2010).

[6] C. A. Schevon et al., *Brain* 132, 3047 (2009).

[7] F. E. Dudek, *Epilepsy Curr.* 9, 151 (2009).

[8] C. Schevon, *J. Clin. Neurophysiol.* 25, 321 (2008).

[9] M. Stead et al., *Brain* 133, 2789 (2010).

[10] V. Woods et al., *J. Neural Eng.* 15, 066024 (2018).

[11] M. Insanally et al., *J. Neural Eng.* 13 (2016).

[12] M. A. Escabi et al., *J. Neurophysiol.* 112, 1566 (2014).

[13] H. Zhang et al., *Neuron* 98, 1269 (2018).

Chapter 7. Natural Wax for Transient Electronics

7.1 Summary

Bioresorbable encapsulation, substrate, and conductive material are critically important in the development of an emerging class of biodegradable electronic devices and implants whose key characteristic is to biodegrade in a controlled fashion after stable operation, over extended time periods. In this report, natural wax that exhibits hydrophobic character and biodegradation by chain scission with very little water absorption is investigated as a possible candidate for robust bioresorbable encapsulants in homogeneous form as well as an electrically conductive component when processed in the form of a tungsten-wax composite. The systematic tests of stability and encapsulation offer operation lifetime of electronics from a few days to a few weeks in aqueous environments. The demonstration of these materials in partially biodegradable wireless LED and NFC circuits shows that they can be integrated into a functional bioresorbable electronic system. Additionally, we use in vivo studies to demonstrate that these materials are nontoxic and biocompatible.

7.2 Introduction

Biologically benign transient devices have recently been introduced and tested in various applications, mostly because of their great promise in reducing electronic waste and related environmental pollutants [1, 2]. Unfortunately, their lifetime is short due to the intrinsic water-soluble nature of the constituent material, thereby creating the need for nontoxic biologically resorbable materials, which can serve to encapsulate the water-soluble electronic components (such as Mg). Further, the identification of a biodegradable conductive material with slower degradation times compared to traditional transient electronics (use of Mg, Zn etc.) will allow for improved electronic device lifetime while reducing long-term electronic waste.

Biodegradation is a key factor in considering a material for use in transient electronics. Biodegradation is often accelerated in warm, aqueous, and aerobic environments [3, 4], which presents a critical issue when considering programmable, biodegradable encapsulants for compostable electronics. Furthermore, even if the selected materials degrade slowly (i.e. months, years), the water vapor permeability of biodegradable materials is inherently high such that the electronic device is rendered useless long before the encapsulation layer(s) degrade. It is necessary, then, to identify encapsulation materials which maximize the life-time of electronic devices by minimizing water vapor transport through the material prior to its biodegradation.

Wax materials such as soy, myrtle and candelilla are derived from natural sources such as soybeans (via soybean oil), myrica cerifera (myrtle) and candelilla shrubs. Natural wax materials are often used over their petroleum-derived wax counterparts because, while they maintain similar properties such as low melting temperature and hydrophobicity, they are also largely biodegradable compared to synthetic waxes such a paraffin – a critical attribute for transient electronics [5, 6]. Natural waxes are comprised of complex chemical mixtures that encompass a wide range of compounds including (but not limited to) long-chain poly- and mono-unsaturated esters, fatty-acids and anhydrides, along with short-chain hydrocarbons (ca. 29-33 carbons/chain), and a variety of resins (such as triterpenes) [7, 8]. The ratio of these compounds will vary depending on the wax source resulting in a series of natural materials with unique rates of water vapor permeability (WVP) and biodegradation (Figure 7.1).

In this chapter, natural wax is investigated as a possible candidate for robust biodegradable encapsulants in homogeneous form as well as an electronically conductive component when processed in the form of a tungsten wax composite. Natural wax materials can exhibit hydrophobic character while maintaining biodegradable functional groups when in the presence of water or moisture, which could potentially correspond to better water barrier transient encapsulants. When combined with conductive powder, such as tungsten, electrically conductive transient traces may also be generated. Significant components of this chapter were published as S. M. Won et al., "Natural Wax for Transient Electronics" *Adv. Func. Mater.* **2018**, 1801819. DOI: 10.1002/adfm.201801819.

7.3 Results and Discussion

While each wax is considered overall hydrophobic in nature (water contact angle measurement > 90° for each wax type) (Figure 7.2), it is anticipated that the degree of water uptake and moisture permeability will differ across the wax types due, in part, to their chemical compositions. To investigate these characteristics, water uptake for each wax is evaluated by measuring the change in water absorption (deionized) per sample area (mg/cm^2) as a function of time for a period of up to 15 days at constant room temperature (24 °C) and biological temperature (37 °C). Differences in water update/absorption between the three wax types are not apparent at room temperature (Figure 7.3a); however, at biologically relevant temperatures (37 °C) differences in water absorption rates occur. Specifically, candelilla exhibits almost no water uptake over the course of 15 days (Figure 7.3b; blue dots), myrtle absorbs water steadily up to ~12 mg/cm^2 at 15 days (Figure 7.3b; green dots), and soy wax absorbs a great deal of water, exceeding 24 mg/cm^2 after only 2 days (Figure 7.3b; red dots). Figure 7.3c presents time-dependent fractional resistance changes ($\Delta R/R_0$ % vs. time in days) of serpentine Mg wires (length 43 mm, width 300 μm, thickness 200 nm) encapsulated with wax films (thickness 300 μm) after immersion in phosphate buffer solution (PBS; pH 7.4, 0.01 mM) at 37 °C. Here, the increase in resistance corresponds to the gradual oxidation of the thin film Mg traces [$Mg + 2H_2O \rightarrow Mg(OH)_2 + H_2$] and is used to determine the relative water permeability of each wax encapsulation layer. The encapsulation with candelilla wax, having the least water absorption rate, yields Mg trace with invariant electrical properties over 10 days while electrical openings appear within one day when Mg traces are encapsulated with soy or myrtle wax ($\Delta R/R_0 \geq 300$ % in < 1 day) (Figure 7.3c). The combined results (water uptake and changes in resistance both as a function of time) suggest that candelilla wax is the most promising of the three natural wax materials for application of a biodegradable, water barrier layer, and will thus be the primary material evaluated throughout the remaining studies.

The effectiveness of any encapsulation depends on the thickness, as summarized by studies of candelilla wax at three different thicknesses using the same Mg test structure described above. The average times to reach fractional resistance changes of 100% are 4, 7 and 11 days for films with thicknesses of 100, 200 and 300 μm, respectively, as in Figure 7.3d. Here, a one-dimensional analytical model, detailed in the experimental section, was applied to study the reactive diffusion of water in wax-encapsulated Mg film, and the diffusivity was calculated as $D_{wax} = 6.05 \times 10^{-1}\ \mathrm{m^2 s^{-1}}$. Images collected at various stages of dissolution of a film of Mg (diameter of 1 cm) encapsulated with a 300 μm thick layer of candelilla wax during immersion in PBS (pH 7.4) at 37 °C are in Figure 7.3e. Consistent with tests of device stability in Figure 7.3c, dissolution of Mg occurs after a stable period of up to 6 days with no sign of water penetration. On the 7th day, effects of hydrolysis become visually apparent until the film completely disappears on the 13th day. Images at day 7 and 13 show that the dissolution of Mg occurs across the entire area of the film, consistent with spatially homogeneous water/moisture transport through the wax encapsulation layer.

The conductive solder paste, used to enable nonplanar interconnects, antennas and other features on/under the wax substrate, must also be transient in nature while maintaining stable function for extended time periods. Here we describe a transient conductive wax (C-wax) composed of a candelilla wax, as a hydrophobic bioresorbable matrix, loaded with tungsten (W) microparticles (diameter of ~5 μm). Figure 7.4a shows the scanning electron microscope (SEM) image of such C-wax (left), embedded W particles in wax matrix, and mapping of chemical composition (right); pink and green correspond to tungsten and wax respectively and are confirmed by energy dispersive x-ray spectroscopy. Figure 7.4b represents the direct current (DC) conductivity of C-wax material as a function of volume fraction of W microparticles. In the binary conductive composites model, the electrical conductivity can be modeled as

$$\sigma = \sigma_0(\phi - \phi_c)^t \qquad \text{for } \phi > \phi_c \tag{7.1}$$

where σ is the conductivity, σ_0 is a scaling factor, ϕ is the volume fraction, ϕ_c is the critical volume fraction (percolation threshold), and t is the critical exponent that defines the dimensionality of the network. Here, the critical exponent (t) should be in the range of 1.6 - 1.9 to follow the equation. The corresponding parameters of C-wax are consistent with a critical volume fraction (ϕ_c) of ~0.13 (weight fraction: ~0.75) and a critical exponent (t) of ~1.6, indicating good agreement with experimental values from similar study in previous literature [9].

Figure 7.5 shows various functional demonstrations of candelilla waxes in homogeneous as well as electrically conductive composite form (with W volume fraction of 0.35). Figure 7.5a shows the image of a radio frequency (RF) inductive coil (~50 μm thick magnesium foil) on biodegradable substrate, poly(lactide-*co*-glycolide) (PLGA), for wirelessly powering the micro light-emitting diode (μ-LED) that is electrically shorted to the coil by a small amount of C-wax applied by melt and drop casting at room temperature. Deep coating such electronics in melted candelilla wax (75 ºC) in homogeneous form results fully biodegradable electronics encapsulated by smooth and uniform wax layer, which enables the wireless operation of LED in PBS at room temperature for 10 days (Figure 7.5b). Screen printing of C-wax on wax substrate can further yield a fully wax based circuit platform as shown in Figure 7.5c, where LED is powered wirelessly through inductive coupling of C-wax based loop antenna.

Biocompatibility of both candelilla and C-wax are important for applications in both consumer electronic devices and biomedical implants. Previous studies have demonstrated the biocompatibility of tungsten and natural wax individually [10-12]. To further examine biocompatibility of these materials together, we implanted candelilla and C-wax (1 cm × 1 cm × 800 μm) subcutaneously in the abdominal region of mice and examined overall health and immune reaction in adjacent skin. Skin tissue sections stained with hematoxylin and eosin (H&E) show no changes in gross histology and immune cell infiltration compared to sham surgery skin (Figure 7.6a). To further quantify the immune reaction to these implanted materials, skin sections were stained with the antibody CD45, a pan-immune cell marker. There were no significant differences in overall intensity of CD45 staining between candelilla, C-wax, and sham surgery groups (Figure 7.6b and c). There were also no significant differences in weight gain between candelilla, C-wax, and sham groups of mice, suggesting that both wax materials have no effect on overall animal health and normal growth (Figure 7.6d). These results confirm and support the previous biocompatibility studies, demonstrating that both candelilla and C-wax are biocompatible and do not initiate significant immune responses.

7.4 Methods

Tests of water uptake. Melting and casting wax (melting points are in Figure 7.7) samples in a PDMS mold yielded cylinders with diameters and thicknesses of 4 and 1 cm, respectively. The initial weights were 13.72 g, 14.50 g, and 13.96 g for soy (Akosoy Natural Soy 125 (415) Wax, Mels Candles, Rolla MO USA), myrtle (Milliard Premium Vegan Bayberry Wax), and candelilla wax (Sigma-Aldrich), respectively. Immersing the samples in DI water at 37 ^{o}C, removing the samples from the solution, and weighing them at several different times yielded the weight of absorbed water.

Tests of water permeation. Photolithography and lift-off using negative photoresist (AZ nLOF2070, MicroChemicals) yielded patterns of Ti/Mg (5 nm/200 nm) on a glass slide. A layer of Cr/Au (5 nm/150 nm) patterned in the same manner defined pads for electrical probing. Dip coating in a molten wax and bonding a well structure of PDMS (Sylgard 184, Dow Corning, USA) on top yielded a platform for testing water permeation. The resistance values were averaged from seven different samples for each case.

Modelling of reactive diffusion for wax encapsulated Mg. The process of wax encapsulated Mg submerged in water (or PBS solution) can be described with reactive diffusion model. One-dimensional analytical model is applied in the thickness direction because the thickness of the wax encapsulated Mg sample ($h_0 + h_{wax}$, where h_0 and h_{wax} are the initial thickness of Mg film and wax encapsulation, respectively) is much smaller than its diameter. The reactive diffusion equations are given as

$$\begin{cases} D\frac{\partial^2 w}{\partial y^2} - kw = \frac{\partial w}{\partial t},\ 0 \le y \le h_0 \\ D_{wax}\frac{\partial^2 w}{\partial y^2} = \frac{\partial w}{\partial t},\ h_0 \le y \le h_0 + h_{wax} \end{cases} \tag{7.2}$$

where w is the water concentration as a function of time t and position y, D and k are the diffusivity of water and reaction constant in Mg, respectively, D_{wax} is diffusivity of water in wax. Water concentration is constant w_0 at the interface between water and top surface of the wax, and the water flux at the bottom surface of Mg is zero, i.e.,

$$w|_{y=h_0+h_{wax}} = w_0 \tag{7.3}$$

$$\left.\frac{\partial w}{\partial y}\right|_{y=0} = 0 \tag{7.4}$$

The initial condition is zero water concentration, i.e.,

$$w|_{t=0} = 0 \tag{7.5}$$

The continuity of concentration and flux of water molecules across the Wax/Mg interface gives

$$w|_{y=h_0-0} = w|_{y=h_0+0} \tag{7.6}$$

$$D\left.\frac{\partial w}{\partial y}\right|_{y=h_0-0} = D_{wax}\left.\frac{\partial w}{\partial y}\right|_{y=h_0+0} \tag{7.7}$$

The above solution is obtained by reducing the solution by Li et al. where reaction exists in both Mg film and its encapsulation layer [13].

$$w(t,y) = w_0\left[\textstyle\sum_1^\infty C_n e^{-\lambda_n t} f_n(y) + g(y)\right] \tag{7.8}$$

where λ_n are eigenvalues determined from

$$\cos\left(\sqrt{\frac{\lambda-k}{D}}h_0\right)\cos\left(\sqrt{\frac{\lambda}{D_{wax}}}h_{wax}\right) = \sqrt{\frac{D(\lambda-k)}{D_{wax}\lambda}}\sin\left(\sqrt{\frac{\lambda-k}{D}}h_0\right)\sin\left(\sqrt{\frac{\lambda}{D_{wax}}}h_{wax}\right) \tag{7.9}$$

$g(y)$ and $f_n(y)$ are given as

$$g(y)=\begin{cases}\dfrac{1}{\sqrt{\frac{Dkh_{wax}^2}{D_{wax}^2}}\sinh\sqrt{\frac{kh_0^2}{D}}+\cosh\sqrt{\frac{kh_0^2}{D}}}\cosh\left(\sqrt{\frac{k}{D}}y\right), 0\le y<h_0\\ 1-\dfrac{1}{1+\sqrt{\frac{D_{wax}^2}{Dkh_{wax}^2}}\coth\left(\sqrt{\frac{kh_0^2}{D}}\right)}\dfrac{h_0+h_{wax}-y}{h_{wax}}, h_0\le y<h_0+h_{wax}\end{cases} \tag{7.10}$$

$$f_n(y)=\begin{cases}\sin\left(\sqrt{\frac{\lambda_n}{D_{wax}}}h_{wax}\right)\cos\left(\sqrt{\frac{\lambda_n-k}{D}}y\right), 0\le y<h_0\\ \cos\left(\sqrt{\frac{\lambda_n-k}{D}}h_0\right)\sin\left[\sqrt{\frac{\lambda_n}{D_{\mathrm{wax}}}}(h_0+h_{wax}-y)\right], h_0\le y<h_0+h_{wax}\end{cases} \tag{7.11}$$

and C_n are coefficients determined by initial condition as

$$C_n=\frac{-\frac{2}{\lambda_n}\sqrt{\lambda_n D_{wax}}\cos\left(\sqrt{\frac{\lambda_n-k}{D}}h_0\right)}{h_0\sin^2\left(\sqrt{\frac{\lambda_n}{D_{wax}}}h_{wax}\right)\left[1+\frac{\sin\left(2\sqrt{\frac{\lambda_n-k}{D}}h_0\right)}{2\sqrt{\frac{\lambda_n-k}{D}}h_0}\right]+h_{wax}\cos^2\left(\sqrt{\frac{\lambda_n-k}{D}}h_0\right)\left[1-\frac{\sin\left(2\sqrt{\frac{\lambda_n}{D_{wax}}}h_{wax}\right)}{2\sqrt{\frac{\lambda_n}{D_{wax}}}h_{wax}}\right]} \tag{7.12}$$

The mass of water that reacts at a given location (per unit volume) is given by kw. Thus, the mass of dissolved Mg (per unit volume) is $kwM_{Mg}/(qM_{H_2O})$, where M_{Mg} and M_{H_2O} are molar mass of Mg and water, respectively, and $q=2$, which represents that 2 water molecules react with each Mg atom. The decrease of the volume of Mg film is then obtained by integrating $kwM_{Mg}/(q\rho_{Mg}M_{H_2O})$ over both the thickness direction y and time t, where ρ_{Mg} is the density of Mg. The Mg thickness h normalized by its initial thickness h_0 is then given as

$$\frac{h(t)}{h_0}=1-\frac{w_0M_{Mg}}{q\rho_{Mg}M_{H_2O}}k\left[\begin{array}{c}\dfrac{1}{\sqrt{\frac{Dkh_{wax}^2}{D_{wax}^2}}\sinh\sqrt{\frac{kh_0^2}{D}}+\cosh\sqrt{\frac{kh_0^2}{D}}}t\dfrac{\sinh\sqrt{\frac{kh_0^2}{D}}}{\sqrt{\frac{kh_0^2}{D}}}\\ +\sum_{n=1}\dfrac{C_n}{\lambda_n}\left(1-e^{-\lambda_n t}\right)\dfrac{\sin\sqrt{\frac{\lambda_n-k}{D}h_0^2}}{\sqrt{\frac{\lambda_n-k}{D}h_0^2}}\sin\sqrt{\frac{\lambda_n}{D_{wax}}h_{wax}^2}\end{array}\right] \tag{7.13}$$

The resistance of Mg film is related to its thickness by $R/R_0 = h_0/h$, where R_0 is the initial resistance. The critical time t_c it takes for the resistance to double ($R = 2R_0$) is then determined by $h(t_c)/h_0 = 0.5$. Here all material parameters are presented in previous studies, including $M_{H_2O} = 18g/mol$, $M_{mg} = 24g/mol$, $\rho_{Mg} = 1.738g/cm^3$, $w_0 = 1g/cm^3$, $k = 1.2 \times 10^{-3}s^{-1}$ and $D = 6.0 \times 10^{-16}\ m^2s^{-1}$, except for the water diffusivity in wax D_{wax}, which is obtained by fitting the experimental data as $D_{wax} = 6.05 \times 10^{-15}\ m^2s^{-1}$, as shown in Figure 7.3d.

Preparation of conductive wax composites. Mechanical mixing of tungsten powder (C10, Buffalo Tungsten) with candelilla wax at 100 ºC on a hotplate yielded well-dispersed mixtures. Melting and drop casting conductive wax formed in this manner on a glass slide through a stencil mask produced well-defined patterns, including circles with diameters of 3 cm and line shapes with 0.5 cm widths and 2.5 cm lengths, for measurements of sheet resistance and tests of reliability (temperature dependence and water degradation), respectively.

In-vitro electrical tests of conductive wax. Sheet resistances of C-wax with different loading fractions of W and candelilla wax were measured using a four-point probing tool (Jandel RM43 AR). With thicknesses determined by the caliper, these data yielded the conductivities of the samples. Placing a test structure of C-wax (line shape with 0.5 cm width, 2.5 cm length, and 0.1mm thickness) on a hot plate allowed measurement of the resistance (FLUKE 87 multi-meter) as a function of temperature. Each data point corresponds to a measurement at a given set temperature, stabilized for 10 minutes. Evaluations of the degradation of C-wax in water involved submerging samples in PBS solution. A thermometer placed next to the samples enabled temperature readings. The resistance values were averaged from five different samples for each test.

Fabrication of Mg-based wireless circuit on wax substrate. A glass slide coated with a thin film of PDMS served as a temporary substrate for a magnesium foil (~50 µm, Solution Materials, LLC, USA). Glass slides were precleaned in a mixture of acetic acid and deionized (DI) water (1:10). Photolithography and wet etching in diluted hydrochloric acid (HCl:DI water= 1:9) define RF coil structures from the foil. A physical transfer process delivers the Mg RF coil onto the surface of a PLGA substrate. The Mg RF coil/PLGA structure was then laminated on a substrate of candelilla wax. Dip-coating in molten candelilla wax forms the encapsulation layer.

7.5 Conclusion

The materials strategies described in this chapter provide examples of how wax-based materials can be tailored for use as encapsulation layers, substrates, and conductive composites for stable, extended operating periods of biodegradable electronics in aqueous environments. Fundamental chemical and electrical studies were carried out for both encapsulation and the conductive composite key properties such as water permeability, biodegradability, conductivity, and stability. Demonstrations with a partially biodegradable wireless LED and NFC circuits illustrate simple applications. The straightforward process enabled by low-temperature melting of the wax and composite materials provides a route for easy integration into already established biodegradable electronics.

7.6 Figures

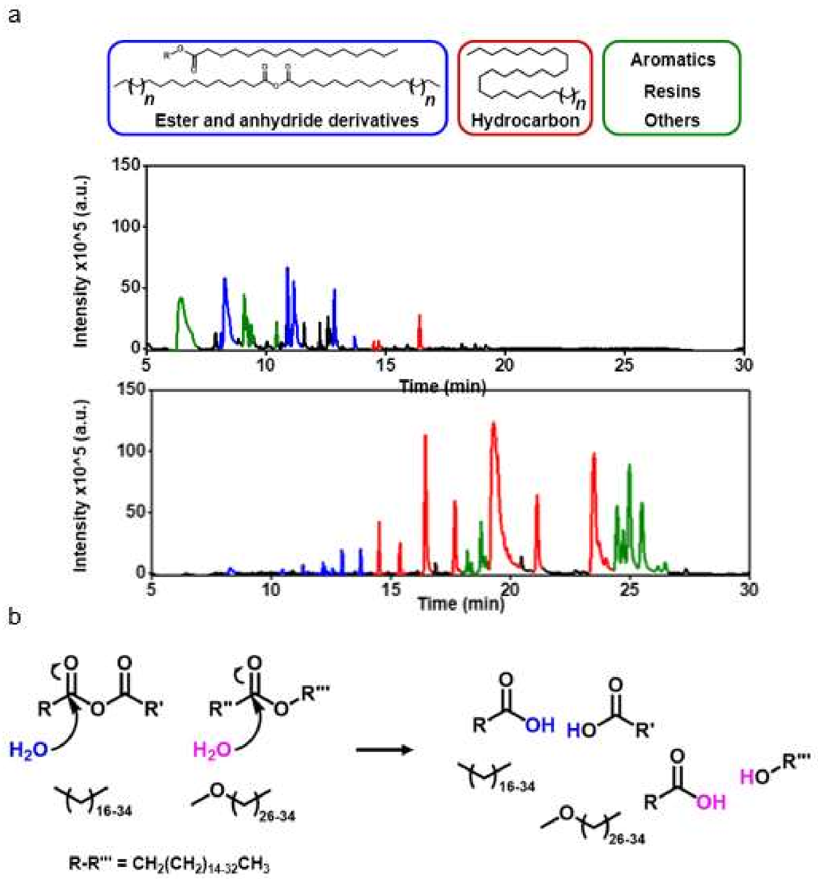

Figure 7.1. Chemistry of nature wax. a) Gas chromatography/mass spectrometry analysis of myrtle wax (top) and candelilla wax (bottom). b) Chemistry associated with the dissolution of wax by cleavage of the ester, anhydride and like moiety.

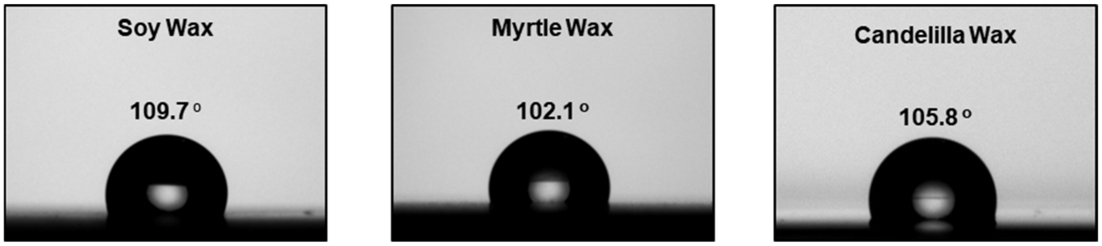

Figure 7.2. Contact angle of natural plant-based wax, soy wax (left), myrtle wax (center), and candelilla wax (right).

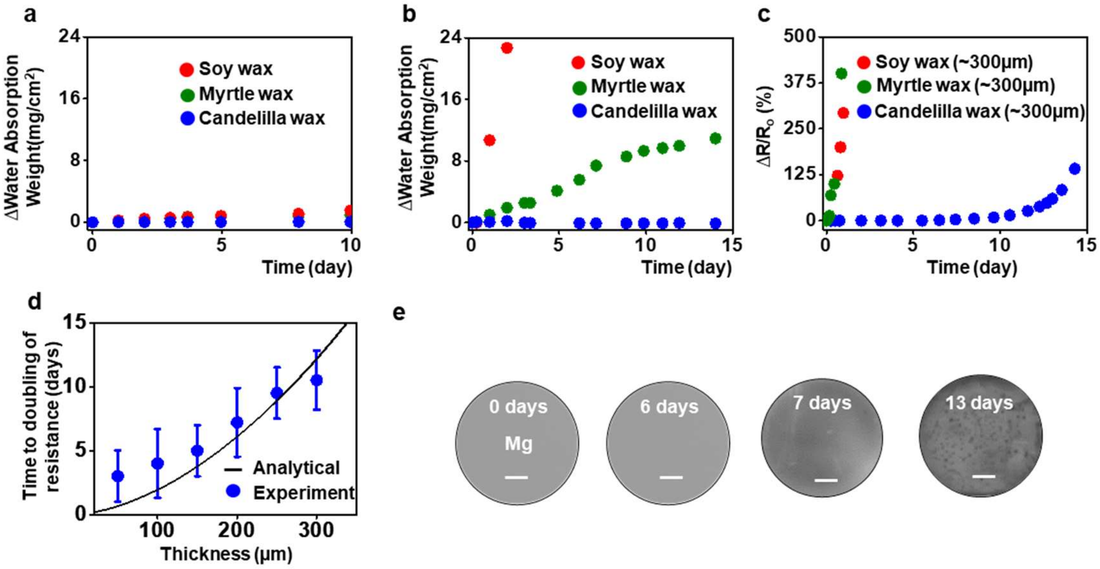

Figure 7.3. Water permeability of natural plant based wax encapsulation. a) The water absorption behavior of wax as measured in phosphate buffer solution pH 7.4 at room temperature. b) The water absorption behavior of soy, myrtle, and candelilla wax as measured in phosphate buffer solution with pH 7.4 at 37 °C temperature. c) Relative water permeation properties of soy, myrtle, and candelilla wax encapsulation layers as measured by the time evolution of the resistance of a thin film trace of Mg. Water that penetrates through the encapsulation layers results in Mg dissolution, thereby increasing their resistance. d) Fractional change in resistance ($\Delta R/R_o$) of a patterned feature of C-wax (2 mm width, 20 mm length, and 100 μm thickness) as a function of time of immersion in PBS solution at RT (black dots) and 37 ºC (blue dots). e) Series of images showing processes of dissolution of C-wax during immersion in DI water at 50 ºC. (Scale bar: 8 μm)

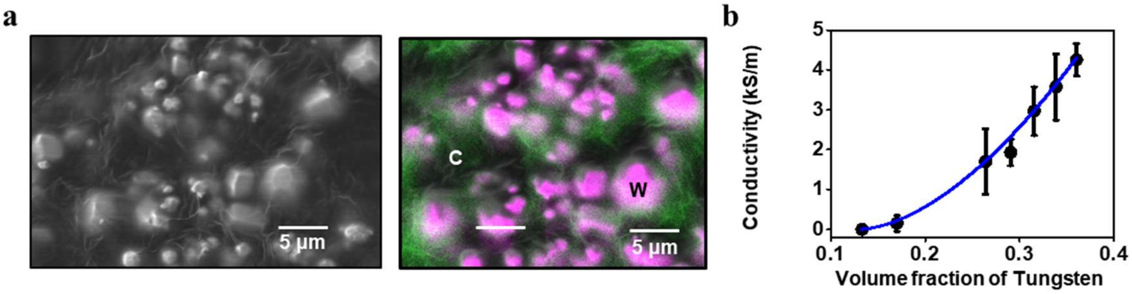

Figure 7.4. Electrically conductive biodegradable trace. a) Sanning electron microscopy (SEM) images of conductive wax (C-wax), compsed of a biodegradable candelilla wax doped with electrically conductive tungsten powder (left). The corresponding energy dispersive spectroscopy image, indicating major elements composing C-wax are carbon (green) and tungsten (pink) (right). b) Conductivity of C-wax paste with various volume fractions of W microparticles (~5 µm) in candelilla wax, evaluated using direct current (DC) measurement.

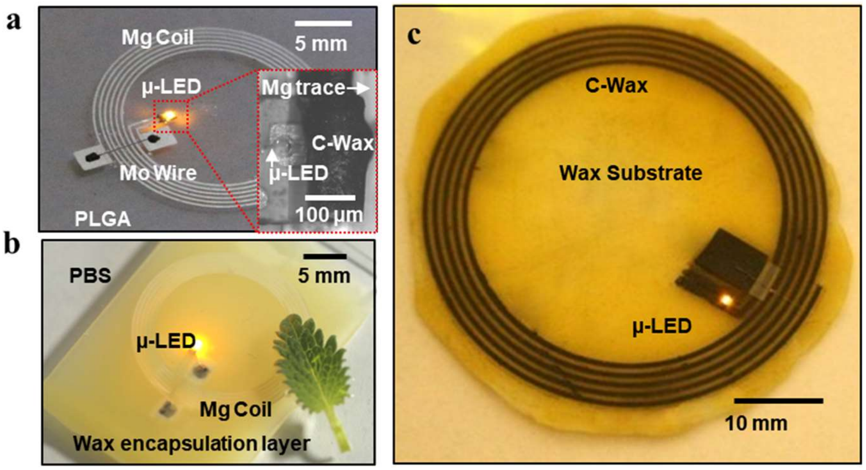

Figure 7.5. Integration of conductive wax and wax encapsulation into biodegradable electronic devices. a) Wireless light-emitting diode (LED) device where C-wax interconnects LED and Mo wire on RF Mg coil. Near field radio-frequency power from primary coil activates an LED in a secondary Mg coil via resonant magnetic coupling. b) Operation of such wireless LED device, covered by candelilla wax encapsulation layer (300 μm) on top and bottom, in PBS solution. Encapsulation layers are dip coated in a melted candelilla wax in 75 ºC oven. c) Fully biodegradable wax-based wireless circuit.

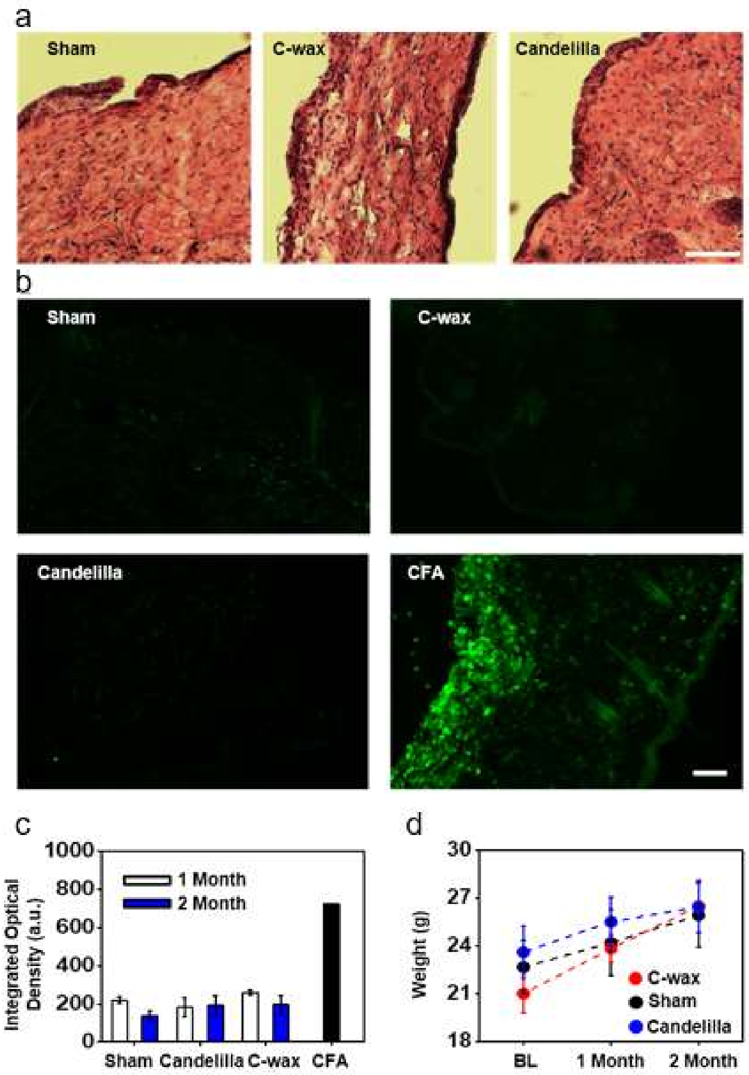

Figure 7.6. Biocompatibility of wax formulations. a) Representative images of H&E stained skin from mice implanted with candelilla, C-wax or sham surgery (scale bar 200 µM). b) Representative images of CD45 staining in skin from mice two months following implantation of candelilla, C-wax, sham surgery, or 24 hrs following injection of complete Freund's adjuvant (CFA) as a positive control for inflammation (scale bar 200 µM). c) Quantification of CD45 staining intensity, demonstrating no significant differences between the sham, Candelilla and C-wax groups (n=2-3 animals per group). d) Mouse weights before, one and two months after implantation of candelilla, C-wax or sham surgery (BL=baseline; n=6 for BL and one month timepoint groups, n=3 for two month timepoint groups). No significant differences were observed between the candelilla, C-wax and sham surgery animals.

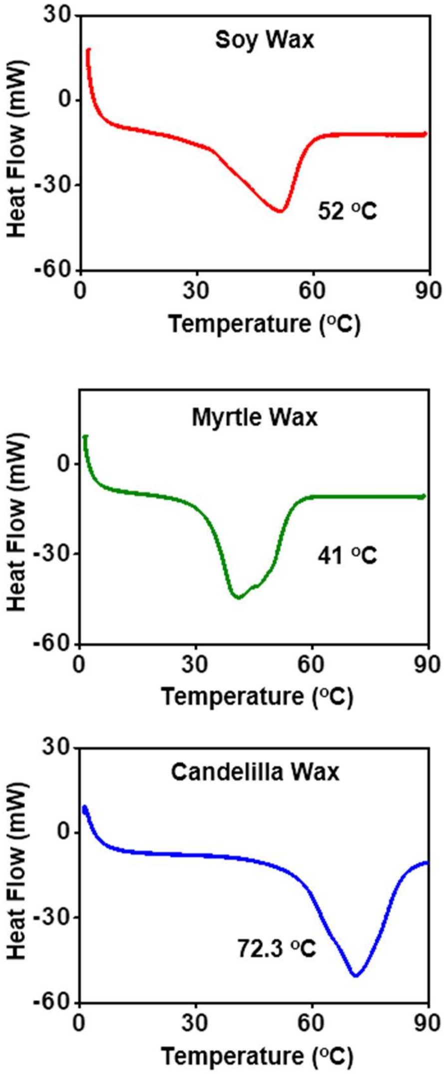

Figure 7.7. Differential scanning calorimetry thermogram of soy (top), myrtle (middle), and candelilla wax (bottom).

7.7 References

[1] K. N. Burns et al., *Int. J. Environ. Res. Public Health*, 13, 140 (2016).

[2] M. Heacock et al., *Environ. Health Perspect.* 124, 550 (2016).

[3] S. K. Kang et al., *Nature,* 530, 71 (2015).

[4] L. Yin et al., *Adv. Mater.* 27, 1857 (2015).

[5] A. E. V. Petersson et al., *Green Chem.* 7, 837 (2005).

[6] N. Gontard et al., Bio-packaging: technology and properties of edible and/or biodegradable material of agricultural origin. In: Mathlouthi M. editor. *Food Packaging and Preservation.* London: Blackie Academic & Professional. p. 159-181 (1994).

[7] R. Rojas-Molina, *J. Med. Plants Res*. 7, 702 (2013).

[8] H. C. Chen, *J. Am. Oil Chem.* 88, 1917 (2011).

[9] S. Lee et al., *Mater. Today,* 21, 207 (2018).

[10] M. Peuster et al., *Biomaterials*, 24, 393 (2003)

[11] M. Peuster et al., *Biometerials*, 24, 4057 (2003).

[12] S. Kanokpanont et al., *Int. J. Biol. Macromol.* 55, 88 (2013).

[13] R. Li et al., *Adv. Funct. Mater*. 23, 3106 (2013).

Chapter 8. Outlook

The results presented here represent recent material strategies for biointegrated electronics that are now available. Resulting systems are collections of advances in electrical/mechanical engineering, material sciences, and micro/nanoscale fabrication techniques that enable flexible, stretchable, and lightweight electronic platforms. Consequently, large-scale, high-density, wireless and multimodal interaction with tissues with minimal irritation after implants can now be achieved. The improvement rate in this area is accelerating as previous findings merge with new engineering strategies. The opportunities will continue to exist not only for bioelectronics research but also for unusual treatment approaches to common disorders and diseases. In addition, future integration will occur not only on the surface but throughout the volume of the entire human biological system.

In all cases, however, chronic operation along with minimally invasive strategies to implant and seamlessly integrate electronics across the large area of the human body remain challenges for the field. Difficulties include monitoring and timely modulation of any immune response, building ultrasoft and deformable electronics for conformal integration, and long-lived biofluid barrier for chronic operation. This dissertation presents some recent work in this direction, but overcoming these challenges still requires additional new concepts in materials science, and mechanical and electrical engineering. Stimuli-responsive polymers and liquid crystal polymers are new materials that could play important roles in the future. In addition, advances in signal processing and modulation based on precollected data stream could be bases for conditional or closed-loop technologies. Such advances could play critical roles in clinical devices for surgical or therapeutic purposes. The diversity of the scientific and engineering content suggests an interesting future for this field.